Tumor-Targeting Nanoparticles for Improved Cancer Therapy

by

Zhangyi Luo

B.S. in Pharmaceutical Sciences, Sun Yat-sen University, 2017

M.S. in Pharmaceutical Sciences, University of Pittsburgh, 2019

Submitted to the Graduate Faculty of the

School of Pharmacy in partial fulfillment

of the requirements for the degree of

Doctor of Philosophy

University of Pittsburgh

2024

UNIVERSITY OF PITTSBURGH

SCHOOL OF PHARMACY

This thesis was presented

by

Zhangyi Luo

It was defended on

January 25, 2024

and approved by

Jan Beumer, Pharm.D., Ph.D., Professor,
Department of Pharmaceutical Science, School of Pharmacy, University of Pittsburgh

Da Yang, M.D., Ph.D., Associate Professor,
Department of Pharmaceutical Science, School of Pharmacy, University of Pittsburgh

Lin Zhang, Ph.D., Professor,
Keck School of Medicine, University of Southern California

Thesis Advisor/Dissertation Director: **Song Li**, M.D, Ph.D. Professor,
Department of Pharmaceutical Science, School of Pharmacy, University of Pittsburgh

Tumor-Targeting Nanoparticles for Improved Cancer Therapy

Zhangyi Luo, Ph.D.

University of Pittsburgh, 2024

In the past decade, advancements in nanotechnology and our growing understanding of cancer biology and nano-bio interactions have led to the development of various nanoparticles (NPs). However, the targeting efficiency of existing NPs is still too limited to be translated into clinic. Developing new tumor targeting NPs and unveiling the targeting mechanism emerges as an ideal strategy to overcome the limitations in the current paradigm of tumor-targeted delivery and improve the therapeutic effect of anticancer agents.

An ultra-small NP was first developed based on 5-azacytidine (AZA)-conjugated polymer (PAZA) for the co-delivery of AZA and BMN673. AZA conjugation significantly reduced the nanoparticle size to 12 nm, allowing efficient tumor targeting through more effective enhanced permeation and retention (EPR) effect and penetration via the in-situ formation of fibronectin-enriched protein corona in the blood, which mediated transcytosis through ITGA5 receptor on tumor cells. An RNAseq-guided mechanistic study demonstrated that PAZA carrier reduced the DNA repair induced by BMN673, sensitizing HR-proficient non-small cell lung cancer (NSCLC) to BMN673. Furthermore, BMN/PAZA enhanced both innate and adaptive antitumor immune response, which was more effective at a lower dosage.

Despite the improved tumor targeting with the ultra-small PAZA NPs, it is still somewhat subjected to the limitation of EPR effect. To target tumors through a mechanism independent of the EPR effect, we developed a biodegradable nanocarrier coated with chondroitin sulfate (PCL-CP). PCL-CP NPs were highly effective in tumor targeting and penetration through both EPR and

CD44-mediated transcytosis in tumor endothelial cells and tumor cells, resulting in superior efficiency in active tumor targeting and tumor penetration. More importantly, we discovered a novel pharmacological target, iRhom1, and elucidated its role in chemo-immuno-resistance. However, there are no small molecule drugs available for inhibiting iRhom1. Better synergy could be achieved by combining chemotherapy drugs with gene therapeutics for "undruggable" targets. PCL-CP was further modified to be effective in co-delivering iRhom1 pre-siRNA (pre-siiRhom) and chemotherapeutic drugs. Co-delivery of pre-siiRhom1 and a chemotherapy agent (DOX or CPT-SAHA) led to significantly enhanced antitumor efficacy and activated tumor immune microenvironment in multiple cancer models.

Table of Contents

List of Tables

List of Figures

Preface

This Ph.D. dissertation presents a summary of the research work accomplished in the Center for Pharmacogenetics, Department of Pharmaceutical Sciences, University of Pittsburgh under the dedicated supervision and guidance of my advisor, Dr. Song Li. I extend my heartfelt gratitude to those individuals who have made valuable contributions to this thesis and provided support throughout this remarkable journey. Without their assistance, this research endeavor would not have been achievable.

First and foremost, I would like to express my sincere gratitude to my advisor, Dr. Song Li, for affording me the invaluable opportunity to start and complete my PhD training under his guidance. He sets an example of excellence as a researcher, mentor, instructor, and role model. It was a real privilege and honor for me to have the opportunity to share in his exceptional scientific knowledge as well as his extraordinary personality. I appreciate his unconditional support for my research and his generosity in allowing me to explore different research directions. His invaluable suggestions, comments, and guidance have inspired me to explore deeper into knowledge and maintain curiosity about new discoveries, ultimately teaching me how to be a true scientist. I am also grateful to him for his generous, selfless support, and patience that he has extended to me over the past six years.

I express my sincere gratitude to my thesis committee members, Dr. Jan Beumer, Dr. Lin Zhang, and Dr. Da Yang, for their invaluable time, suggestions, and encouragement throughout this process. The feedback I received enabled me to move beyond my comfort zone and consider problems from various perspectives.

I would also like to thank my ‘greater Li family’: Thank Dr. Yixian Huang for teaching me the various drug delivery techniques and continuous sharing his broad knowledge, rich experience, and insightful suggestions. Thank Dr. Jingjing Sun for her help in polymer synthesis and for the collaborative opportunities she provided. Thank Dr. Jieni Xu for teaching me all the protocols and techniques during my initial period in the Li lab. Also, thanks for her guidance and assistance during my early years as a junior graduate student. Thank Dr. Yuang Chen and Dr. Haozhe Huang for their invaluable assistance in my research, as well as for their efforts in organizing the Pitt pharmacy basketball events, which have brought me lot of joy alongside my research. Many thanks to my other dear lab members (Dr. Dingwei Diao, Dr. Chaogang Wei, Dr. Zhuoya Wan, Pearl Moharil, Ziqian Zhang, Apurva Pardeshi, Dr. Yan He, Dr. Yangwuyue Liu, Shengzhen Liu, Dr. Shangyu Chen, Sheida Dabiri, Chien-yu Chen, Bei Zhang, Yiqing Mu, Shichen Li, Huatian Li) for their inspiration and assistance at every stage of my progress.

I would also like to express my gratitude to all the faculty and staff members at the Center for Pharmacogenetics. Special thanks to Dr. Wen Xie, Dr. Xiaochao Ma, Dr. Da Yang, Dr. Christian Fernandez and Dr. Simone, Brixius-Anderko for fostering an exceptional environment for research and personal growth. Special thanks are extended to Dr. Yang and his group members, Zehua and Yifei, for their guidance in training me in molecular biology techniques. Many thanks go to the faculty members of the School of Pharmacy at the University of Pittsburgh. Special thanks to Dean. Amy Seybert, Dr. Kerry Empey, Dr. Robert B Gibbs, Dr. Maggie Folan, Bailey Tobias, and Lori M. Altenbaugh for their continuous support and help all these years.

I would like to express my sincere gratitude to my remarkable family for the love, support, and continuous encouragement throughout the years. I would like to thank my parents, Zongyu Luo and Xiaomei Zhang, for their support and encouragement. They provided me the freedom and

fortitude to pursue my dream. Finally, I would like to express my deep gratitude to my best friends, soul mates, and girlfriend, Ka Kei Lo, for her tolerance, support and love. She restored my confidence and brought brightness into my life. We mature alongside one another, serving as life partners and overcoming future challenges together.

1.0 Overview of Current Tumor Targeting Strategies

1.1 Introduction of EPR effect

The enhanced permeation and retention effect, also known as EPR effect, is a well-established physiological phenomenon that occurs in anatomical and pathophysiological abnormalities. In this phenomenon, the endothelial lining in the blood vessel wall becomes more permeable and leakier than in normal vasculature. This is commonly observed in tumors, infarcts, and other pathological sites in the body [1]. These gaps were found to have a size range up to 2000nm. Consequently, in these regions, macromolecules and nanoparticles (NPs) within a specific size range of 10-500 nm are able to extravasate into the interstitial space, which qualified the criteria for "permeation" in the EPR effect [2]. The selective permeation of this tissue was demonstrated in numerous tumors, inflammations, and infarcted areas. Furthermore, once nanoparticles (NPs) have penetrated the tumor interstitial space, the compromised lymphatic vessels are unable to facilitate the transportation of macromolecules from the tumor, representing an additional pathophysiological abnormality of tumor tissue. This anomaly resulted in the notion that lymphatic vessels in tumors are 'dysfunctional' and that the lumen is too narrow for nanoparticle transportation [1]. These concepts qualified the "retention" aspect of the EPR effect, leading researchers to hypothesize that nanoparticles would accumulate or be retained within the tumor due to their limited ability to exit.

Over the past three decades, EPR-mediated drug delivery has been recognized as an effective method for targeted delivering drugs to tumors, particularly macromolecular drugs and drug-loaded pharmaceutical nanocarriers. Nevertheless, only 15 nanomedicines based on

nanoparticles have received approval for clinical use in cancer therapy, with an additional 190 nanoparticle-based nanomedicines currently undergoing clinical trials [3]. Doxil/Caelyx, the first approved nanomedicine for breast cancer in 1995, has paved the way for the development of NP-based chemotherapy formulations. Subsequently, Abraxane and Vyxeos have emerged as advanced treatment options for various cancer types, such as breast cancer, pancreatic adenocarcinoma, non-small cell lung cancer, and leukemia. Further development of NP-based formulations with chemotherapy drugs is underway in multi-stage clinical trials. In addition to small-molecule drugs, recent advancements in RNA technology have led to the clinical evaluation of nucleic acid-based therapies with nanoparticle-based formulations.

There is certainly enough evidence to support the notion that NP-based delivery can enhance the effectiveness of cancer therapy. Nevertheless, the current benefits of nanomedicine are constrained to the reduction of systemic toxicity [4]. The improvement in efficacy in clinical settings remains elusive. The limited enhancement in efficacy has been linked to the failure of distinct nanoparticle accumulation in the tumor and an unfavorable pharmacokinetic profile. This suggests that EPR strategy as a mechanism for tumor targeting, may not fully optimize the delivery efficiency of nanoparticles. Warren Chan and colleagues found that only 0.7% of systemically administered nanoparticles reach solid tumors based on EPR effect [5]. The unexpected low accumulation of EPR effect is a complex and comprehensive issue that has sparked significant controversy within the field of nanomedicine.

The significance and presence of the importance and the existence of EPR effect in solid tumors in human patients have recently been heavily debated. It is eminent that the EPR effect is notably more pronounced in small animal xenograft tumor models, commonly employed for assessing cancer nanomedicines in preclinical settings, in comparison to tumors in human subjects

[6]. The accumulation of nanocarriers in human tumors is indeed observed, but the extent of this phenomenon varies significantly among patients. It is challenging to identify the specific factors contributing to the disparity between preclinical models and the multifaceted process that encompasses various physiological and morphological parameters, which can impact the overall efficacy of EPR effect in human patients.

1.2 Heterogeneity of EPR effect in different tumor type

1.2.1 Vascular permeability

The size of vascular fenestration serves as the physiological basis of EPR effect. Nevertheless, the foundation has been called into question as a result of the heterogeneity observed in various types of tumors. A recent study has demonstrated that the aggressiveness of the tumor is one of the factors contributing to heterogeneity. In other words, rapidly proliferating tumors, such as carcinomas, are characterized by underdeveloped vasculature, resulting in more permeable and leaky blood vessels. While slow-growing tumors like sarcomas exhibit less permeability compared to carcinomas, this implies that the efficacy of nanoparticle targeting dependent on the EPR effect may be compromised. Indeed, in tumors with low permeability, the size of large-scale nanodrugs within the vascular endothelial space may not effectively facilitate transvascular transport [7]. Nanodrugs smaller than 10 nm in size have the ability to efficiently penetrate tumors through both transvascular and extravascular transport mechanisms. Nevertheless, the rapid clearance by the kidneys eliminates those NPs before they reach the tumor, leading to an insufficient EPR effect [8]. Nanodrugs, which typically range in size from 100 to 200 nm, have

the capability to achieve prolonged circulation in the body. Nevertheless, as a result of the aforementioned low permeability, they frequently encounter challenges in achieving passive targeting to the tumor site through intravascular transport, also resulting in the compromised EPR effect [9].

Insufficient permeation resulted in increased hindrance to the nanoparticles' ability to target tumors through EPR effect, while excessive vascular leakage can also impede the extravasation of nanoparticles. The chemotherapy treatment of tumors often leads to excessive vascular leakage in the tumor area, which in turn causes an increased release of multiple inflammatory cytokines. The condition can also be caused by the systemic toxicity of a drug, resulting in the apoptosis of endothelial cells. An overabundance of leakage can lead to the escape of plasma and hemoconcentration, leading to flow stasis and elevated interstitial fluid pressure (IFP) [10]. Furthermore, in the context of enhanced vascular damage, fibrin clots deposited during the process will obstruct blood flow and endothelial gap. All of these mechanisms act to prevent the nanoparticles from reaching the tumor. Therefore, the heterogeneity in vascular requires customization of nanoparticle designs to suit various tumor types and their respective vascular conditions.

1.2.2 Blood flow

The irregular vasculature within the tumor typically results in irregular blood flow. In contrast to the vessels in normal tissue, tumor vessels exhibit insensitivity to angiotensin receptor type 2 (AGTR2) [11]. Furthermore, intermittent blood flow (occurring only once every 15–20 minutes) and reverse blood flow are observed at the site of the tumor. Tumor vessels exhibiting irregular structure are further distinguished by a curved vascular shape, filling of the endothelial

cell septum, and impairment of the basement membrane. These effects result in the distortion of vascular morphology, leading to an increase in the geometric resistance of blood flow. Furthermore, tumor blood contributes to an increase in blood viscosity through elevated hematocrit levels. The elevation of vascular resistance and blood viscosity markedly augments the impediment to blood perfusion in the tumor region, ultimately impairing the trans-vascular transport efficiency of NPs.

1.2.3 Blood vessel pericyte and basement membrane

The vascular wall consists of endothelial cells, pericytes, smooth muscle cells, and the basal membrane, collectively responsible for facilitating proper function and selective exchange of macromolecules between blood and tissue [12]. While the majority of studies concentrate on the impact of tumor endothelial cell on EPR effect, it is important to note that pericytes and the basal membrane also play a significant role in the extravasation process. The tumor vasculature is characterized by several features: 1) a defect in endothelial-pericyte interactions, 2) a loose association of the basement membrane with endothelial cells and pericytes, and 3) broad extensions away from the vessel wall, as well as a thickened layer of basal membrane [13]. Consequently, these structural abnormalities indicate that the deficiency in anticipated permeability may not exclusively stem from the endothelium, but also from the vascular basement membrane.

1.2.4 Abnormal interstitial barrier

In addition to the abnormalities in blood vessels, tumor interstitial fluid pressure (IFP) and tumor extracellular matrix (ECM) are recognized as barriers to effective drug delivery or the EPR effect. In normal tissue, lymphatic vessels function to remove excess fluid, thereby maintaining the interstitial fluid pressure (IFP) at or near zero. However, in tumor tissue, the lymphatic system is compromised, which is an important factor contributing to the retention effect. The uniformly elevated IFP in tumor tissue can be attributed to the absence of functional lymphatic vessels within tumors, as well as the compression caused by rapidly proliferating tumor cells. In fact, the IFP inside the tumor tissue closely approximates the microvascular pressure, leading to hindered diffusion of macromolecules, such as nanoparticles, across the blood vessel wall [14]. Moreover, the majority of the NPs that reach the tumor tend to remain in the periphery of the tumor rather than achieving uniform distribution throughout the entire tumor. The nanoparticles located at the interface of blood vessels and the peripheral region of the tumor may also return to the blood supply as a result of intravasation driven by IFP. The presence of these factors impedes the transport across vessel walls and undermines the advantages of the EPR effect [15].

The tumor extracellular matrix (ECM) is characterized by its distinctive stiffness and fibrotic stroma within the tumor microenvironment, typically composed of collagen and hyaluronic acid (HA) [16]. They are primarily secreted by stromal cells that exhibit significant dysregulation and are interconnected to create a complex network. The dense ECM in tumors can create a physical obstacle that impedes the accumulation and diffusion of nanotherapeutics at the tumor sites, thereby significantly compromising their therapeutic efficacies [17]. The inhibitory effect on the ECM is particularly notable in solid tumors, including breast cancer, pancreatic

cancer, and bladder cancer, which are frequently characterized by the abundant formation of ECM in the tumor microenvironment.

1.3 Strategies to improve EPR-based effect

Multiple factors can contribute to the heterogeneity of EPR effect in different tumor types and affect the overall tumor-targeting efficiency. Various strategies have been developed for improving the EPR-based tumor targeting through each aspect of the heterogeneity (**Table. 1-1**).

1.3.1 Enhancing the interendothelial gap dependent extravasation

The presence of gaps in tumor vascular ECs is a significant factor contributing to the EPR effect. In certain tumors characterized by poor permeability, the size and permeability of interendothelial gaps may be too restricted to allow large-scale NPs to effectively achieve trans-vascular targeting. Efforts to enhance permeability have involved studying various aspects, ranging from the modification of nanoparticles to the modulation of tumor vessel permeability.

A direct approach involves disrupting the integration of vascular endothelial to widen the gap between TECs. Numerous molecules have been assessed for their potential to disrupt vascular endothelial function. For instance, nitric oxide (NO) serves as a crucial signaling molecule that can impact endothelial barrier function in various ways by affecting blood vessels. NO diffuses from endothelial cells to surrounding vascular smooth muscle cells, resulting in vasodilation, increased blood flow, and augmented extravasation of fluid and small molecules. Treatment of the flavonoid acetic acid-based agent 5,6-dimethylxanthenone-4-acetic acid (DMXAA) leads to

elevated levels of NO and serotonin, resulting in disassembly of endothelial conjunction. The incorporation of DMXAA into nanoparticles can lead to the disruption of tumor vascular endothelial, resulting in enhanced tumor targeting through the disruption of vasculature [18]. Another example involves the use of combretastatin A4 phosphate (CA4P), a tubulin-binding agent, to induce vessel disruption by inhibiting tubulin polymerization. Co-delivery CA4P with chemotherapy drugs, such as Doxorubicin, can initially induce vessel disruption, thereby improving the delivery of Doxorubicin to tumor tissue [19].

Furthermore, in addition to chemotherapy agents, radiotherapy also substantially increases the permeability of tumor vasculature by triggering the apoptosis of tumor endothelial cells (TECs). Study indicated that ^{131}I-labeled BSA encapsulated in liposomes exhibited greater retention at the tumor site compared to blank liposomes, indicating enhanced tumor vascular permeability. Patients who receive Doxil in combination with radiotherapy demonstrate a higher overall remission rate, potentially attributable to enhanced drug delivery following radiotherapy [20].

In addition to enhancing the EPR effect by modulating the physiological vascular condition, optimizing the size of the NPs can also improve trans-vascular penetration to the tumor. Research has demonstrated that NPs below 30 nm show greater accumulation in tumors compared to NPs with a size of 100 nm, particularly in poorly permeable tumors like pancreatic cancer. Nevertheless, this distinction was eliminated in hyperpermeable tumors, indicating the benefit of reducing the size of NPs for targeting poor permeable tumors [21].

1.3.2 Augmentation of blood perfusion

As previously mentioned, the primary impediments to blood perfusion are the irregular structure of the vasculature and the compression of blood vessels caused by increased solid stress. Consequently, increasing perfusion in tumor blood vessels can be accomplished through augmentation of blood flow, vascular normalization, and decompression accordingly.

Suzuki et al artificially induce hypertension by administering angiotensin II to enhance blood flow [22]. Interestingly, tumor blood vessels typically do not have a smooth muscle layer or pericytes necessary for vasoconstriction in response to angiotensin II, unlike the blood vessels in normal tissues, which exhibit constriction (hence hypertension). The differential response to angiotensin II in tumor blood vessels compared to normal blood vessels results in an increase in blood flow volume to tumor tissues due to vasoconstriction of the normal blood vessels. Certainly, nanoparticles (NPs) can exploit enhanced blood perfusion, leading to their accumulation in tumor regions by leveraging the augmentation of EPR effect and further improved chemotherapy [23].

Vascular normalization represents an alternative approach aimed at mitigating the challenge of inadequate blood perfusion in tumor tissues. The occurrence of vascular abnormality in tumors is typically attributed to the persistent activation of proangiogenic factors. Hence, antiangiogenic drugs or antibodies were considered for the normalization of tumor blood vessels. The administration of angiogenesis inhibitors, such as bevacizumab, has been shown to induce tumor vessel normalization by increasing pericyte coverage. This process enhances oxygenation levels and has been demonstrated to improve the antitumor effect of radiotherapy [24]. The normalization of tumor blood vessels through treatment with antiangiogenic antibodies resulted in improved tumor targeting of nanoparticles smaller than 12 nm, while it hindered the uptake of nanoparticles larger than 125 nm [25]. This paradox arises from the observation that the

administration of antiangiogenic antibodies leads to a significant reduction in the size of vessel fenestrations, which form the basis of the EPR effect. This suggests that both the time window and dose window need to be optimized in order to strike a balance between tumor vessel normalization and vascular permeability.

Decompressing vessels by ablating cells or extracellular matrix in tumors has the potential to alleviate solid stress and enhance blood perfusion. For instance, Saridegib, a semi-synthetic derivative of cyclopamine, has been shown to decrease solid stress and enhance blood flow perfusion by suppressing the proliferation of cancer-associated fibroblasts (CAFs). A study has demonstrated that the administration of Saridegib in pancreatic cancer resulted in a 10% increase in the diameter of the blood vessels and lymphatic vessels within the tumors, as well as a 47% increase in the perfusion vessel fraction [26].

1.3.3 Overcoming pericyte and basement membrane barrier

The conventional EPR effect is commonly associated with a reduction in pericyte coverage and basement membrane extent on tumor vessels, as compared to normal tissues [27]. Nevertheless, a recent study has demonstrated that basement membrane still covers over 92% of the blood vessels in various tumor models. Following traversal of the endothelial barrier, NPs are impeded by the basement membrane barrier within the subendothelial space, leading to the formation of perivascular NP pools [28]. Through the utilization of local hyperthermia therapy, it is possible to disrupt the NP pools formed with the basement membrane, thereby releasing the entrapped NPs into tumors by recruiting neutrophils [28].

1.3.4 Alleviating IFP and ECM stiffness

Elevated IFP can result from both a compromised lymphatic system and leaky vasculature. Most strategies focus on the restoration of blood vessels, as mentioned previously. Repairing the lymphatic system may also significantly reduce the retention time of NPs in tumors. The VEGF receptor 2 antibody, DC101, was employed for the restoration of blood vessels. However, the findings indicated that it cannot only normalize the blood vessels surrounding the tumor site, but also decrease the IFP in the tumor. This led to increased tumor accumulation and penetration, particularly in small-sized NPs (~12nm) [25]. Similarly, celecoxib, a commonly utilized pharmaceutical agent that functions as a cyclooxygenase-2 (COX-2) inhibitor, has the capacity to not only reduce tumor IFP by normalizing tumor vasculature, but also to diminish tumor-associated fibroblasts within the tumor microenvironment and disrupt the fibronectin network. The human-derived A549 tumor xenograft model was treated with oral celecoxib at a dosage of 200 mg/kg. After two weeks, the interstitial fluid pressure in the tumor returned to normal, resulting in a significant increase in the penetration depth of small-sized NPs (~20 nm) [29].

Furthermore, in order to overcome the IFP, NPs must pass through dense ECM to effectively penetrate deep tumor tissues. Cancer and stromal cells have the capacity to generate significant actomyosin forces on the ECM, which contribute to an increase in ECM stiffness [30]. Hence, mitigating the ECM and its mechanical constraints by either inhibiting its formation or accelerating its degradation could decrease transport resistance and thus improve the NPs-based delivery. TGF-β inhibitor has been studied as a promising approach for ECM modulation. These inhibitors have the potential to not only decrease the presence of pericytes, but also to impede the development of the interstitial matrix, particularly collagen I [31]. For instance, LY364947, a highly potent ATP-competitive inhibitor targeting the TGF-β type I receptor, was employed to

augment the tumor penetration of 30-70 nm micelles [21]. Another study demonstrated that losartan has the potential to decrease the levels of TGF-β, leading to a notable reduction in collagen. The depletion of collagen further led to increase in the accumulation and penetration of NPs [32]. A comparable approach, which aimed to target collagen degradation, was accomplished using NPs containing collagenase [33]. Furthermore, a recent study has demonstrated that the inhibition of focal adhesion kinase (FAK) can specifically modulate the ECM stiffness instead of simply degrading it. Co-delivery of FAK siRNA has the potential to enhance CRISPR/Cas gene editing by promoting the uptake of the NPs and their penetration into tumors [34].

Table 1-1. Summary of current strategy to improve the EPR effect.

Strategy	Therapeutic method	Mechanism
Endothelial gap	DMXAA	Induce the release of NO and serotonin
	CA4P	Induce vessel disruption
	Radiotherapy	Triggering the apoptosis of tumor endothelial cells
Blood perfusion	Angiotensin II	Specifically increase in blood flow volume to tumor tissues
	bevacizumab	Facilitate tumor vessel normalization
	Saridegib	Enhance blood flow perfusion by suppressing the proliferation of cancer-associated fibroblasts
Pericyte and basement membrane	Local hyperthermia therapy	Disrupt the basement membrane of tumor vascular
IFP and ECM	DC101	Decrease the IFP in the tumor
	celecoxib	Diminish tumor-associated fibroblasts within the tumor microenvironment and disrupt the fibronectin network
	LY364947	Deplete collagen I
	FAK siRNA	Modulate the ECM stiffness

1.4 Transcytosis-based active targeting

The controversy surrounding EPR-dependent tumor-targeting has led to a growing interest in active targeting as an alternative strategy to enhance tumor targeting, independent of the EPR mechanism. A recent study by Chan et al. has demonstrated that the primary mechanism of nanoparticle transport is an active process, rather than the commonly acknowledged EPR-mediated passive process. This suggests the pivotal role of the transcytosis-based mechanism in tumor targeting [35]. The primary inquiry will be how nanoparticles can traverse vasculature in order to specifically target tumor tissue that is not reliant on the EPR effect. Transcytosis serves as an additional trans-endothelial transport pathway utilized physiologically to complement the active transportation of macromolecules, such as nutrients like albumin. Previous studies have demonstrated the binding of albumin to the gp60 protein in caveolae of endothelial cells, facilitating its transport across the vasculature [36]. This interaction has been leveraged to develop albumin as a carrier for transporting chemotherapy drugs in vivo, as exemplified by Abraxane [36]. Similar endogenous transcytosis has also been identified for the transportation of ultrasmall ferritin. The statement is based on physiological research indicating that a subset of tumor and normal blood vessels form a chain of grape-like interconnected vesicles and vacuoles, termed vesiculo-vacuolar organelles [37]. The presence of physiologically pre-existing transcytosis enlightened the development of active-targeting NPs utilizing transcytosis, leading to the identification of numerous targeting ligands to improve the tumor targeting of NPs.

1.4.1 Peptide-based transcytosis

One of the most extensively studied tumor-targeting peptides is the RGD motif and its derivatives. The RGD motif identifies integrin heterodimers formed by the V unit (CD51) and the β3 unit (CD61) on the surface of TECs. This complex acts as a receptor for vitronectin and plays a role in angiogenesis [38, 39]. Researchers have advanced the development of a cyclized RGD peptide (cRGD) to enhance targeting efficiency. This is because linear peptides are more flexible and can engage in more nonspecific interactions with the cell membrane, whereas cyclic peptides are more rigid and can facilitate more specific interactions [40, 41]. Additionally, in the majority of cases, cyclic RGD peptides exhibited lower cytotoxicity compared to linear peptides [41]. Several nanoparticle formulations containing cRGD have been designed to target TECs, such as lipid NPs, polymeric micelles, and PAMAM dendrimers [40, 42-44].

An enhanced iteration known as iRGD (CRGDKRGPDEC), derived from the RGD peptide, was subsequently refined through in vivo T7 phage display, featuring a sequence akin to the conventional cyclic RGD [45]. iRGD not only exhibits binding affinity to the tumor vasculature, but also demonstrates significant penetration into the tumor core. This feature holds significant importance as it addresses the challenge of NPs encountering difficulty in penetrating tumor tissues due to the dense stroma, as previously discussed. The process of iRGD penetration involves three sequential steps. First, the RGD motif binds to αv integrins on TECs. Subsequently, it undergoes proteolytic cleavage, revealing a binding motif for neuropilin-1. Finally, neuropilin-1 facilitates the penetration into the tumor core [45]. This process could elucidate the mechanism by which iRGD-modified NPs effectively target both cancer cells and TECs. iRGD-conjugated NPs have been shown to target and penetrate tumors through transcytosis in various tumor models, including low-permeability tumors such as pancreatic adenocarcinoma [46, 47].

1.4.2 Antibody-based transcytosis

Antibodies serve as a versatile ligand for a variety of transcytosis receptors. In the context of TECs, VEGFR2 is a highly potent and widely acknowledged receptor for nanoparticle targeting, given its predominant expression on TECs. Research has indicated that the conjugation of NPs with anti-VEGFR2 antibodies resulted in a fourfold increase in targeting efficiency toward breast tumors, which are characterized by the presence of VEGFR2-expressing vascular endothelial cells [48]. The level of VEGFR2 antibody conjugation has been found to be associated with improved tumor targeting and antitumor efficacy [49]. In addition to VEGFR2, the overexpression of ICAM-1, a surface glycoprotein typically found on endothelial cells, has been noted in various cancer types linked to advanced disease, low survival rates, and resistance to chemotherapy. The study demonstrated that the targeting of ICAM-1 through the use of ICAM-1 antibody-conjugated iron oxide nanoparticles is an effective strategy for imaging triple-negative breast cancer [50]. Another study demonstrated that the conjugation of anti-ICAM-1 antibody to a lipid nanoparticle (LNP) loaded with siRNA targeting lipocalin2 effectively suppressed tumor growth by negatively regulating angiogenesis [51].

1.4.3 Polysaccharide-based transcytosis

Cancer cells frequently exhibit distinct glycans compared to normal cells, resulting in the alteration of saccharide receptors on tumor endothelial cells. CD44 is the primary exploited saccharide receptor, which is overexpressed on both tumor cells and tumor endothelial cells. While it enhances tumor malignancy as a stem cell marker on tumor cells [52], it also exerts regulatory effects on angiogenesis and the function of endothelial cells [53].

Hyaluronic acid (HA) has garnered significant attention for its targeted delivery capabilities among all the ligands of the CD44 receptor. Several studies have demonstrated that the surface modification of nanoparticles with HA can greatly improve the uptake and accumulation in tumors, both *in vitro* and *in vivo* [54-57]. In addition to HA, chondroitin sulfate (CS) serves as another ligand for CD44. Similar to HA, chondroitin sulfate is also recognized as a natural polymer known for its biocompatibility and biodegradability. CS-modified nanoparticles also demonstrated improved in vivo tumor targeting and anti-tumor efficacy when delivering a range of therapeutic agents [58-60]. A recent and more intriguing study systematically illustrates that CS can additionally facilitate efficient transcytosis across tumor endothelial cells and tumor cells [62].

P-selectin is a cell adhesion molecule possessing inflammatory properties that are involved in the recruitment of leukocytes and the binding to platelets. It is expressed in ECs constitutively. P-selectin is stored within intracellular granules known as Weibel-Palade bodies in quiescent ECs. Upon endothelial activation induced by endogenous cytokines or exogenous stimuli, such as ionizing radiation, P-selectin translocate to the cell membrane and subsequently into the lumen of blood vessels [61, 62]. Elevated P-selectin expression has been noted in the vasculature of human lung [63], breast [64], and kidney cancers [65]. To specifically target P-selectin on TECs, fucoidan, an algae-derived polysaccharide that serves as the natural ligand for P-selectin, was utilized to modify NPs to enable their P-selectin targeting ability. The fucoidan-based nanoparticles were designed to target activated endothelium, showing the ability to penetrate endothelial barriers in vitro. In vivo studies demonstrated their therapeutic advantage over untargeted chemotherapeutic drugs or passively targeted nanoparticles in P-selectin–expressing tumors and metastases [66]. A subsequent study also demonstrated the involvement of P-selectin-mediated transcytosis in the

transport of nanoparticles across the blood-brain barrier, leading to the targeting of the brain and the inhibition of medulloblastoma, which is the most common malignant pediatric brain tumor [67].

1.4.4 Cationic-based transcytosis

The cationic surface of NPs is recognized for its affinity to both tumor cells and tumor endothelial cells, as these cells typically exhibit high levels of anionic proteins on their surfaces. Therefore, cationic nanoparticles can readily bind to the cell surface via charge-charge interactions, leading to cellular uptake and transcytosis. It has been reported that Cationic LNP is preferentially transported to inflamed, angiogenic vessels in both tumor tissue and chronically inflamed lungs [68]. These cationic LNPs have been developed for in vivo RNA silencing therapy in a lung-metastasis tumor model [69, 70]. However, cationic LNP will also susceptible to rapid recognition by RES system and quickly removed from circulation. An enzyme-activatable polymeric nanoparticle has been designed to achieve a balance between "stealthy" and "sticky" properties. This neutral long-circulating micelle can be transformed into a cationic micelle by the γ-glutamyl transpeptidase on the luminal endothelial cell surface. This transformation facilitates cationic-based transcytosis through TECs and enables tumor penetration [71].

1.4.5 Limitation and improving strategy for active targeting

Transcytosis-based active targeting is a fast-growing field as EPR effect is becoming controversial. However, as previously mentioned, a particular receptor is essential for the majority of transcytosis-based targeting strategies, which may impose certain limitations. The crucial point

to consider is that the efficiency of tumor targeting is determined by both the distribution and quantity of the receptor. The non-tumor distribution of the receptor can drastically decrease the distribution of NPs in the tumor. For example, an ex vivo near-infrared (NIR) imaging studies employing Cy5.5-labeled HA-CA nanoparticles, which exploit CD44-mediated transcytosis, demonstrated intense fluorescence in the liver. This can be attributed to the uptake of HA-CA nanoparticles by phagocytic cells of the RES system and by liver sinusoidal endothelial cells expressing the comparable level of CD44 [57]. Partially shielding the CD44 ligand is a promising strategy to prevent non-tumor endothelial cells from being undesirably targeted. Study showed that optimizing the surface amount of PEG shielding can reduce uptake by liver sinusoidal endothelial cells without compromising transcytosis in tumor endothelial cells [72].

Furthermore, the pathological condition had a significant impact on receptor status. It is shown that NRP-1, a primary receptor for iRGD-mediated tumor targeting, is downregulated in acute myeloid leukemia patients undergoing thalidomide treatment [73]. In addition to the regulation at the gene level, the post-translational regulation of receptors also influences their function in mediating transcytosis. An illustration of this phenomenon is the cleavage of the CD44 extracellular region, which results in a reduction in the uptake of NPs in tumor cells. However, the use of ADAM17 inhibitors can prevent the cleavage of CD44 and also restore the CD44-mediated tumor uptake. This topic will be further explored in chapter 3 in this PhD defense.

In addition to receptor-related limitations, after the NPs have reached the tumor tissue through transcytosis, the IFP and ECM hindrance could also act as barriers for NPs to distribute within the tumor, rather than remaining at the interface of the tumor-blood vessel. A potentially effective approach involves the use of a ligand capable of mediating transcytosis in both tumor

cells and tumor endothelial cells, thereby enhancing tumor penetration following arrival at the tumor [71].

1.5 Bioinspired tumor-targeting strategies

In addition to the passive tumor targeting mediated by EPR effect and the active targeting mediated by ligands, bioinspired targeting strategies have also been developed. The representative strategy for coating cell membranes involved researchers directly utilizing entire cell membranes as a material for nanoparticle coating. The complexity of a cell's membrane, including its lipids, proteins, and carbohydrates, can be preserved by directly transferring the outermost layer onto the surface of a nanoparticle. This process enables the resulting membrane-coated nanoparticle to exhibit many properties of the source cell. This rationale has been used to exploit multiple cell membranes for enhanced drug delivery to tumors. For example, studies have shown that platelet-functionalized NPs can target to tumor and circulating tumor cells, possibly because of the presence of P-selectin on the platelet surface, which can bind to the CD44 receptor on the cell surface [74, 75].

White blood cell (WBC) membrane-coated NPs have similarly been proposed for potential application in the delivery of cancer drugs. This is because leukocytes have the ability to target sites of inflammation, which has long been associated with certain types of cancers and tumor vasculature remodeling. the WBC membrane coating strategy enabled the particles to traverse across the endothelial layer, resulting in the selective destruction of cancer cells. In contrast, both free drug and drug-loaded uncoated particles exhibited a preference for killing endothelial cells rather than crossing the barrier. In vivo, the coatings were found to be effective in preventing liver

uptake and phagocytosis by Kupffer cells. This evasion of the immune system, in conjunction with the particle's affinity for tumors through inflamed endothelium, resulted in increased accumulation within B16 mouse melanoma tumors. Intravital microscopy further showed that the particles residing within the tumor microvasculature [76]. It is also believed that the WBC membrane may facilitate the targeting of tumors through specific receptor-ligand binding. The presence of CD49d, a surface marker and primary ligand for vascular cell adhesion molecule 1 (VCAM-1), was initially verified on the WBC coated NPs to improve tumor uptake [77]. In a different instance, neutrophil membrane-coated nanoparticles can effectively target endothelial cells through ICAM-1. This enables the neutrophil membrane-coated nanoparticles to target both established metastases or premetastatic niches, ultimately leading to an anti-tumor and anti-metastasis effect [78]. Nanoparticles coated with the membrane of cytotoxic T cells have also been reported to target tumors through ICAM-1 [79].

The progress in synthetic biology has enabled the development of a versatile platform for bacterial-based tumor targeting, which can be engineered to exhibit complex behaviors not achievable with current nanotechnology and molecular approaches. For instance, *Magnetospirillum magneticum* strain AMB-1, a magnetotactic bacteria can be externally manipulated using magnetic fields in vivo. This manipulation resulted in a fourfold increase in translocation across an in vitro model of vascular endothelium and a 21-fold higher colonization of tumor spheroids when guided by magnetic torque. A threefold increase in bacterial accumulation was noted in tumors subjected to magnetic torque after the intravenous administration of magnetotactic bacteria in a mouse model of breast cancer with subcutaneous MCF-7 tumors [80]. In a separate investigation, researchers developed a genetically encoded microbial encapsulation system that allows for adjustable and dynamic expression of surface

capsular polysaccharides. This system was designed to improve the systemic delivery of *Escherichia coli* Nissle 1917. The bacteria have the ability to temporarily evade immune attack, whereas subsequent loss of encapsulation leads to effective clearance in vivo. This dynamic delivery strategy enabled a tenfold increase in the maximum tolerated dose of bacteria and enhanced the anti-tumor efficacy in murine cancer models [81].

1.6 Conclusion

While there is a widespread belief in the revolutionary impact of nanotechnology on cancer therapy, the translation of nanomedicine from fundamental research to clinical application has encountered challenges. Based on a recent survey, the phase II trials had a failure rate of 52%, while the failure rate in Phase III trials was as high as 86%. The primary reason for the majority of failures in both Phase II (71.4%) and Phase III (100%) trials was attributed to inadequate therapeutic efficacy, which was a result of the limited ability of nanomedicines to overcome sequential physiological barriers [3].

The preview provided an overview of the current tumor targeting strategy, beginning with the EPR effect and progressing to the development of bioinspired tumor-targeting carriers (**Fig. 1-1**). Several strategies have been developed to demonstrate improved tumor-targeting delivery of nanomedicine; however, limitations persist for these innovative approaches. As our understanding of tumor heterogeneity advances, it has become clear that a single strategy cannot be used to target different tumor categories. Indeed, cancer genomics, including RNA-seq and single-cell RNA-seq, has revealed additional heterogeneity, indicating the significance of "tailored therapy" in the nanomedicine field. This approach involves the application of tumor-targeting strategies based on

individual identified targets and tumor status, which is equally important as the development of new targeting strategies.

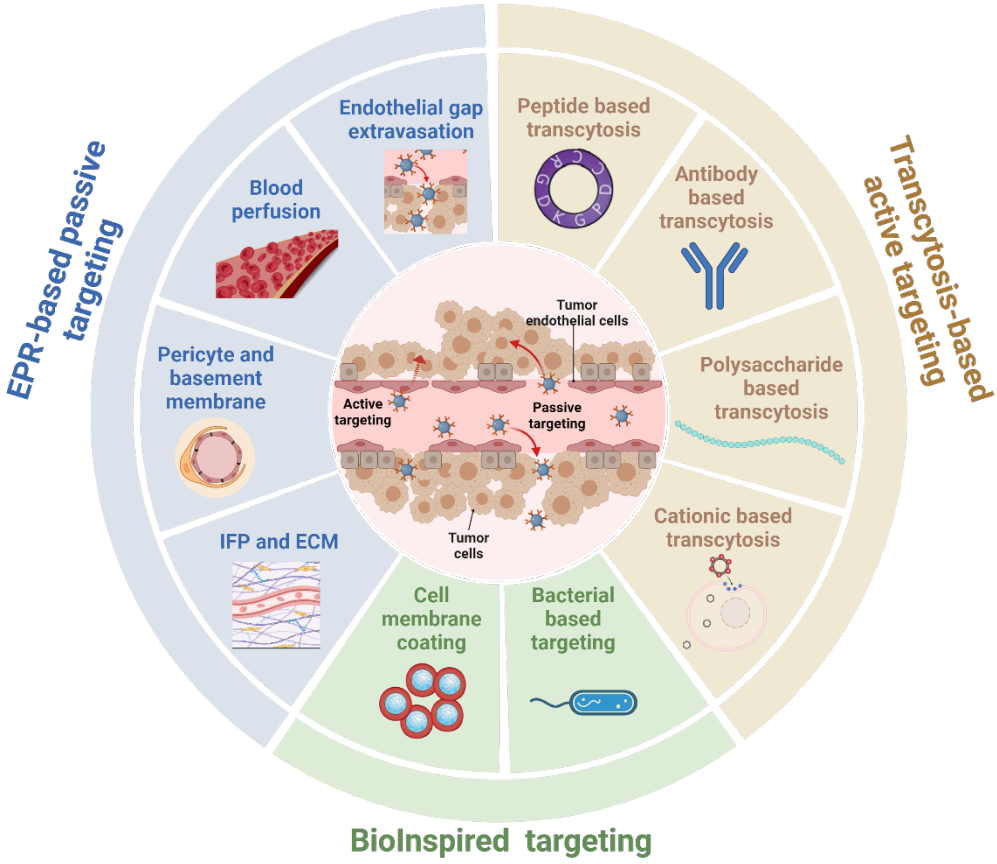

Figure 1-1. Current strategies to improve tumor targeting.

2.0 In situ Formation of Fibronectin-Enriched Protein Corona on Ultra-small Nanocarrier for Enhanced Synthetic Lethal Therapy

2.1 Strategies to improve EPR-based effect

Inhibition of PARP1 is an clinically effective synthetic lethal therapy in homologous recombination (HR)-deficient cancers by generating double strand breaks (DSBs)[82]. However, it offers insubstantial benefit for the majority of cancer types that are HR-proficient, such as non-small cell lung cancer (NSCLC). Moreover, cancer patients succumb to PARPi resistance through various feedback mechanisms such as induction of the anomalous hypermethylation of tumor suppressor gene promoters[83, 84]. A key player in the resistance is DNA methyltransferase 1 (DNMT1), which is overexpressed in tumors, mediating abnormal DNA methylation patterns that epigenetically silence the expression of tumor suppressor genes[85]. Intriguingly, epigenetic modifiers like DNMT1 inhibitors (DNMTi) potentially affect DNA repair, rendering HR-proficient tumor cells of HR-deficient phenotype and sensitizing them to PARPi and other DNA-damaging agents[86-89]. From the immunological perspective, DNA-damaging agents have the potential to convert immunologically "cold" tumors to "hot", augmenting immunotherapy via mechanisms like cyclic GMP-AMP synthase (cGAS)-stimulator of interferon genes (STING) pathway[90], elevation of tumor mutation burden[91], and the upregulated generation of HLA-neoantigen complex[92]. Meanwhile, DNMTi could upregulate the expression of MHC I gene[93], enhancing the immune system's recognition of tumor cells through increased presentation of neoantigens. Taken together, combination of DNMTi with PARPi represents an attractive approach to improve the treatment through several synergistic mechanisms.

However, oral administration of PARPi shows low bioavailability and poor drug accumulation in the tumor tissue, necessitating the use of high doses in patients, which may cause off-target toxicity and limit its long-term use[84]. Similarly, DNMTi such as 5-azacytidine (AZA) and decitabine are unstable and show limited duration of action due to enzymatic inactivation by cytidine deaminase (CDA)[94]. Nanocarriers have emerged as a powerful tool in enhancing the bioavailability of free drugs[95-97]. However, it is still challenging to co-load water-insoluble PARPi and water-soluble AZA into a single nanocarrier with high drug co-loading. In addition, tumor targeting and penetration represents another major barrier for nanoparticles (NPs)-mediated cancer therapy. Smaller nanoparticles (NPs) often exhibit superior tumor accumulation and penetration[21, 98]. It is generally assumed that smaller NPs shall be more effective in passing through paracellular space in both tumor endothelium lining as well as the tumor cells and stromal cells following extravasation[99, 100]. However, a recent study utilizing Au NPs of varying sizes have revealed that most NPs enter tumors through active transcytosis processes within endothelial cells[101]. Contrary to previous assumptions, passive diffusion through leaky vasculature seems to be a secondary route of entry even for 15 nm Au NPs. Nonetheless, the exact mechanisms governing this trans-endothelial process have remained elusive, particularly for the more effective smaller NPs. In addition, it remains uncertain whether this phenomenon extends to other nanocarrier systems, such as polymeric NPs. Moreover, although increasing evidence demonstrates that smaller NPs achieve deeper tumor penetration, the underlying mechanism is still underexplored. Unraveling these puzzles holds the key to engineering the next generation of nanocarriers, ensuring deeper tumor penetration and potentially revolutionizing therapeutic outcomes.

In this work, we developed an ultrasmall nanocarrier PAZA for co-delivery of DNMTi AZA and PARPi Talazoparib (BMN) to enhance synthetic lethal therapy in HR-proficient tumor. By conjugating AZA to a specific PVD polymeric backbone, the particle size was significantly reduced to 12 nm. This reduction facilitated tumor penetration through clathrin-mediated transcytosis, a departure from the generally assumed paracellular transport mechanism. Through proteomics and genetic knocking out (KO) approaches, we found that fibronectin was enriched in the protein corona (PC) surrounding PAZA nanocarrier, which interacted with the ITGA5 receptor on tumor cells, contributing to effective tumor uptake and penetration. The in-situ formed PC-PAZA NPs loaded with BMN exhibited remarkable antitumor activity in HR-proficient NSCLC at low dosages. Furthermore, BMN/PAZA increased the immunogenicity, synergizing effectively with PD-1 antibodies to combat orthotopic LLC lung cancer.

2.2 Material and Method

2.2.1 Reagent

4-Vinylbenzyl chloride, 4,4'-dithiodibutyric acid, triethylamine, 4-Cyano-4-(phenyl-carbonothioylthio)pentanoic acid, poly(ethylene glycol)methyl ether methacrylate (average Mn = 950), 2,2-Azobis (isobutyronitrile) (AIBN), Dulbecco's Modified Eagle's Medium (DMEM), RPMI 1640 Medium, trypsin-EDTA solution, 3-(4,5dimethylthiazol-2-yl)-2,5-diphenyl tetrazolium bromide (MTT), D-Luciferin were purchased from Sigma-Aldrich (MO, U.S.A), BMN673 and 5-Azacytidine were purchased from MedChemExpress LLC (NJ, USA).

2.2.2 Cell lines and Animals

LLC murine NSCLC cancer cell line and A549 human NSCLC cell line were obtained from ATCC (Manassas, VA). They were cultured in DMEM medium supplemented with 10% FBS and 1% penicillin/streptomycin at 37 °C in a humidified atmosphere with 5% CO2.

ITGA5 KO cell line was generated by using CRISPR technology. LLC cells were infected with the lentivirus packaged by ITGA5-All-in-one lentiviral sgRNA-CRISPR-Cas9 plasmid encoding EGFP and puromycin resistance (Horizon Discovery Ltd., Cambridge, UK). The successfully knocked out cells were selected by cell sorting of EGFP+ and ITGA5 KO population. Cells were further confirmed by western blot analysis for the lack of ITGA5 expression.

Female C57BL/6 mice (4–6 weeks) were purchased from Charles River (CA, U.S.A). All animals were housed under pathogen-free conditions according to AAALAC (Association for Assessment and Accreditation of Laboratory Animal Care) guidelines. All animal-related experiments were performed in full compliance with institutional guidelines and approved by the Animal Use and Care Administrative Advisory Committee at the University of Pittsburgh.

2.2.3 Polymer synthesis and chemical characterization

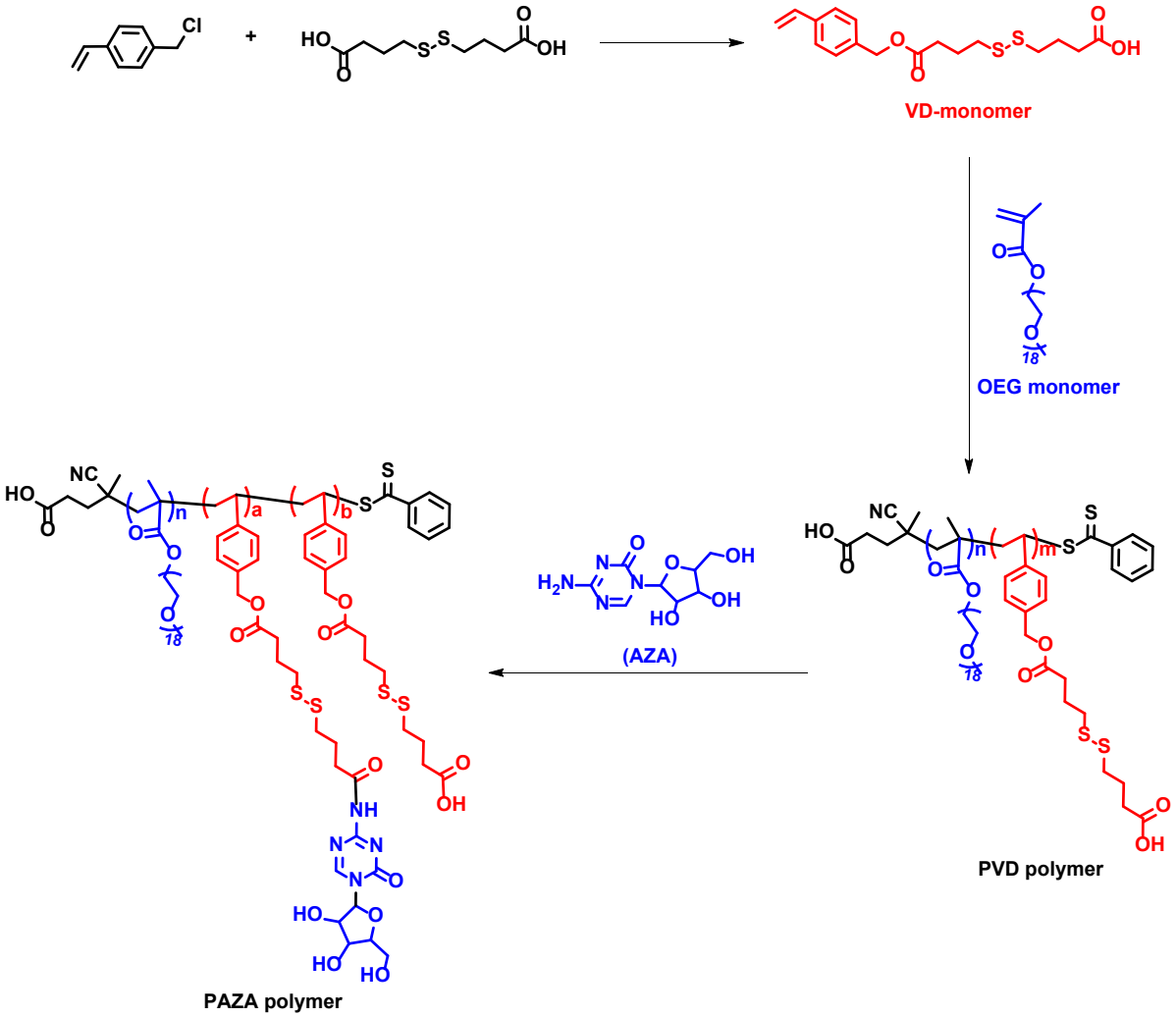

Figure 2-1. Synthesis route of PVD and PAZA polymers by RAFT polymerization and subsequent AZA conjugation.

The synthesis route of PAZA and PVD polymer are shown in **Fig. 2-1**. The PVD polymer backbone was synthesized by controlled reversible addition-fragmentation chain transfer (RAFT) polymerization of poly(ethylene glycol) methyl ether methacrylate (Mn=950) and VD monomer. Briefly, AIBN (3.6 mg, 0.0223 mmol), 4-Cyano-4-(thiobenzoylthio)pentanoic acid (8 mg, 0.0287 mmol), poly(ethylene glycol) methyl ether methacrylate (Mn=950) monomer (800 mg, 0.84 mmol), and VD monomer (680 mg, 2.15 mmol) were added into a Schlenk tube containing 2 mL of tetrahydrofuran. After three freeze-pump-thawing cycles, the tube was placed into an oil bath

(80 °C) and the reaction mixture was stirred under the protection of N_2. After 20 h, the reaction was quenched and the PVD polymer was obtained by precipitation in ether for 2 times.

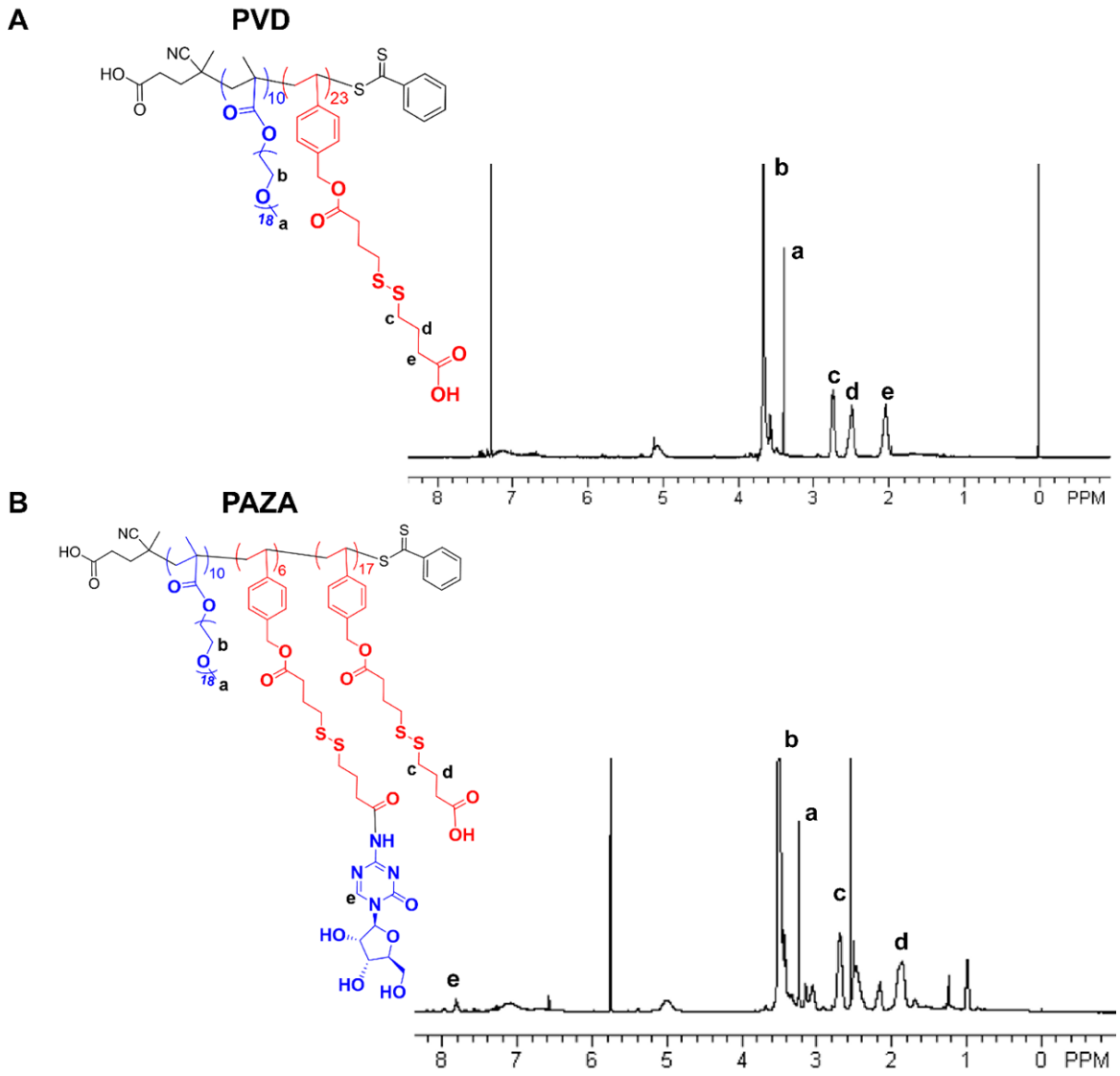

Figure 2-2. NMR characterization of PVD polymer and PAZA polymer.

(A) PVD polymer. The ratio of PEG unit and VD unit is determined by the integration ratio of peak a to peak c. (B) PAZA polymer. The number of poly (ethylene glycol) methyl ether methacrylate and PVD units in the PVD polymer were determined to be 10 and 23, respectively, by comparing the intensities of Ia and Ic in (A). The number of conjugated AZA unit was determined to 6 by comparing the intensities of Ia and Ie in (B).

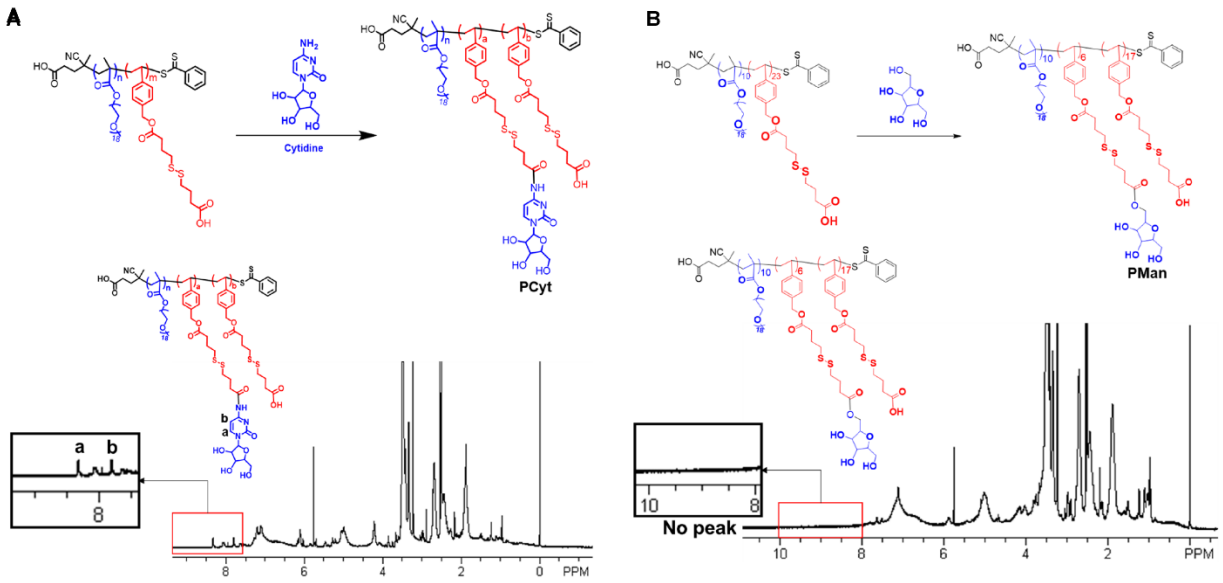

Figure 2-3. NMR characterization of PCyt polymer (A) and PMan polymer (B).

The PAZA polymer was obtained by conjugation of AZA to PVD backbone. PVD polymer (60 mg, 0.085 mmol -COOH), EDC (200 mg, 1.04 mmol) and HOBT (80 mg, 0.6 mmol) were dissolved in 15 mL of DMSO with the addition of 200 µL of DIPEA. Then, AZA (80 mg, 0.33 mmol) was added to the solution and stirred at room temperature for 72 h. The PAZA polymer was obtained after dialysis against DMSO/water and lyophilization.

The PCyt and PMan polymers were synthesized similarly as PAZA polymer. AZA (80.59 mg, 0.33 mmol) was replaced by Cytidine (80.26mg, 0.33 mmol) and Mannitol (60.12 mg, 0.33 mmol), respectively.

The structures of these polymers were characterized by NMR (**Fig. 2-2&2-3**).

2.2.4 Preparation and characterization of drug-loaded micelles

Blank micelles and BMN-loaded micelles were prepared via a film hydration method. Briefly, BMN solution (10 mg/mL in methylene chloride) was mixed with PVD or PAZA polymer (20 mg/mL in methanol) at different carrier/drug weight ratios. The solvent was removed by

nitrogen flow to produce a thin film of carrier/drug mixture, which was further dried in vacuum for 2 h to remove any remaining solvent. Then the thin film was hydrated and gently vortexed in PBS to form final formulation. Particle sizes, polydispersity and morphology was measured by DLS (Nano-ZS 90, Malvern Instruments, Malvern) and transmission electron microscopy (TEM). CMC was measured using Nile red as a fluorescence probe [102]. Drug loading capacity and efficiency of BMN was measured by Waters e2695 HPLC system equipped with a Waters 2489 UV detector according to a published chromatography condition [103].

2.2.5 Stability and drug release kinetics

The stability of the BMN/PAZA drug-loaded micelles was measured both in PBS solution and after lyophilization. For lyophilization stability study, 1 mL of BMN/PAZA micelle solution was lyophilized after size measurement. The lyophilized powder was re-dissolved by 1 mL nanowater to regenerate the BMN/PAZA drug-loaded micelle solution for size measurement. For long term stability study, the micelle solution was re-measured for size after standing 4 weeks under room temperature.

BMN *in vitro* drug release study was conducted by dialysis method. Briefly, 1 mL of BMN/PAZA micelles containing 6 mg of BMN in PBS buffer were placed in a clamped dialysis bag and immersed in 25 mL of 0.1 M PBS buffer solution containing 0.5% (w/v) Tween 80 with 10 mM GSH, 10 μM GSH or without GSH. Each group was triplicated. The experiment was performed in an incubation shaker at 37 ℃ at 100 rpm. At selected time intervals, both 10 μL BMN/PAZA micelles solution in the dialysis bag and 1 mL medium outside the dialysis bag were withdrawn while same amount of fresh medium was added for replenishment. The BMN concentration was determined by HPLC as described above.

AZA release study was also conducted similarly. PAZA micelle (20 mg) in PBS buffer were placed in a clamped dialysis bag and immersed in 50 mL of 0.1 M PBS buffer solution with 10 mM GSH, or without GSH. For stability assay, 20 mg of blank PAZA micelle in 100 uL plasma or tumor lysate (100 mg/mL) were placed in a clamped dialysis bag and immersed in 50 mL of 0.1 M PBS buffer solution. Each group was triplicated. The experiment was performed in an incubation shaker at 37 ℃ at 100 rpm. At selected time intervals, 10 mL of medium outside the dialysis bag was withdrawn while same amount of fresh medium was added for replenishment. The withdrawn medium was lyophilized and the AZA was extracted by 90% methanol. The elution condition is 0.1% TFA: Methanol: Acetonitrile = 95:2.5:2.5.

Intracellular release of AZA was detected by LC-MS. The LLC cells were incubated with 10 mg of PAZA for 6 h, 12 h, 24 h, 48 h, and 72 h respectively. Cells were lysed and extracted by 50% methanol. 100 µL of the sample was transferred to a tube, to which 100 µL methanol containing the internal standard (gemcitabine) was added. The samples were then vortexed and centrifuged for 10 minutes at 10,000 x g. The AZA concentration was detected by LC-MS/MS. Chromatographic separation was performed using a Thermo Hypersil GOLD C18 column (2.1 x 100 mm, 1.9 µm). An isocratic (50:50) gradient was used for AZA with a total runtime of 3 minutes using the mobile phases water with 0.1 % formic acid (A) and acetonitrile (B).

2.2.6 In vitro cytotoxicity assay

Cytotoxicity assay was performed on BRCA-proficient NSCLC cell lines LLC and A549. The cytotoxicities of AZA, BMN673, AZA plus BMN, PAZA carriers alone, and PAZA/BMN with different doses were examined by MTT assay. Cells were seeded in 96-well plates at a density of 5000 cells/well for 24 h. Then, the medium was replaced with fresh medium containing different

formulations every 24 h for 96 h. After incubation, the medium in each well was replaced with 0.2 ml of fresh medium containing 0.5 mg/ml MTT, and incubated for another 3 h. The medium in each well was further replaced with 0.1 mL DMSO to dissolve the formazan crystals. The absorbance in each well was measured at 562 nm and 620 nm using a microplate spectrophotometer. Cell viabilities were calculated from following equation, where OD is the optical density of sample or control at the indicated wavelength:

$$\text{Cell viability}(\%) = \frac{\text{OD}_{sample,\,562nm} - \text{OD}_{sample,620nm}}{\text{OD}_{control,562nm} - \text{OD}_{control,620nm}}$$

2.2.7 Cellular uptake and endocytosis pathway analysis

For cellular uptake study, the LLC cells were incubated with rhodamine labeled PAZA and PVD NPs, respectively, for 6 h. Then, the culture medium was discarded, and cells were washed with cold saline for 3 times. The cell nucleus was stained with Hoechst 33342 Cellular, followed by washing with saline for 3 times. Cellular uptake was measured by fluorescence microscope (BZ-X800, Keyence). For endocytosis pathway analysis, the cells was pre-incubated with different endocytosis inhibitors including filipin, chlorpromazine, amiloride, dynasore, cytochalasin D and mβCD, separately for 2 h at the working concentrations that were not toxic to the cells[104] . Then, the medium was replaced with fresh medium, and treated with rhodamine labeled PAZA and PVD NPs (500 ng/mL rhodamine), respectively. At 6 h after addition of NPs, the cells were washed with cold saline 3 times and analyzed by flow cytometry.

2.2.8 *In vitro* transwell assay

For all transwell based studies, an *in vitro* multilayer LLC cell or LLC-ITGA5 KO cell model was established by seeding the cells in a 0.4 μm diameter microporous membrane (Corning, product no. 3470). Membranes were inserted in 12 well plates followed by incubation for 4 days [105]. The lower chamber was added with blank DMEM medium, and the upper chamber was added with DMEM medium containing rhodamine-labeled PVD or PAZA NPs (500 ng/mL rhodamine), with or without pre-treatment with transcytosis inhibitor chlorpromazine (6 μg/ml) for 2 h. At 10 h after addition of NPs, the fluorescence intensity of the medium in the basolateral side was determined. In fibronectin-mediated transcytosis study, similarly, the lower chamber was added with blank DMEM medium, and the upper chamber was first treated with Anti-ITGA5 antibody or IgG isotype control for 2 hours, then added with blank DMEM medium containing rhodamine-labeled PVD or PAZA NPs (500 ng/mL rhodamine), with supplement of fibronectin (10 μg/mL) or mouse serum. In a separate study, cells were first seeded in 0.4 μm diameter microporous membrane, followed by incubation for 4 days to develop the multilayer cells. One day before treatment, the lower chamber was replaced with a new plate and seeded with LLC cells. Then, the upper chamber was added with DMEM medium containing rhodamine-labeled PVD or PAZA NPs (500 ng/mL rhodamine), respectively. At 6 h after addition of NPs, the cells were washed with cold saline for 3 times and analyzed by flow cytometry.

2.2.9 Cell spheroid penetration

WT or ITGA5 KO LLC cells were seeded in a Nunclon Sphera 96 well U-bottom plate (Thermofisher) at a density of 10000 cells per well with 6 μg/ml of collagen I to form a single

spheroid per well [106]. After 96 h incubation, dense spheroids were formed, which were confirmed by microscope. The cell spheroids were incubated with rhodamine labeled PVD or PAZA NPs (500 ng/mL rhodamine) respectively, with or without pre-treatment with transcytosis inhibitor 6 μg/ml chlorpromazine (6 μg/ml) for 2 h. In a separate study, the cell spheroids were incubated with rhodamine labeled PVD or PAZA NPs (500 ng/mL rhodamine) in 10% FBS medium, blank medium or medium with fibronectin (10 μg/mL) respectively. After 18 h incubation with NPs, the cells were gently rinsed by saline 3 times. The penetration ability was observed by a confocal laser scanning microscope with Z stack scanning (CLSM, FluoView 3000, Olympus) at 20 μm intervals from the bottom to the middle of the spheroids.

2.2.10 Tumor models

Subcutaneous (s.c.) LLC tumor model was established by injecting LLC cells into the flank of C57BL/6 mice. Orthotopic LLC tumor model was established by resuspending 1×10^6 luciferase-expressing LLC cell line (LLC-Luc) in a 1: 1 mixture of PBS and Growth Factor-Reduced (GFR)-Matrigel, followed by orthotopically injecting into the left lateral thorax of C57B6 mice[107]. The tumor size and location were monitored and quantified with a noninvasive bioluminescence system (Perkin Elmer IVIS 200 system).

2.2.11 Tumor targeting and tumor penetration

The tumor targeting effect of PAZA was evaluated in both WT/ITGA5 KO LLC model (s.c). and orthotopic model using a larger PVD carrier as a control. Hydrophobic fluorescence dye DiR was loaded into the PAZA carrier or PVD control polymer at a wt/wt ratio of 40:1 and intravenously injected into the mice for real-time imaging at the DiR dosage of 1 mg/kg. After 24 h, the mice were imaged by an IVIS 200 system with excitation at 730 nm and emission at 835 nm. The tumor and various organs was then excised for *ex vivo* imaging following our previous protocol [102]. The tumor was then frozen sectioned and stained with DAPI to label the cell nucleus and the antibody for CD31 to label the vascular endothelial cell. The fluorescence signals in the core of the tumor were examined under Keyence BZ-X800 fluorescence microscope.

2.2.12 Therapeutic study

The LLC tumor-bearing mice (5 mice each group) with tumors of volume ~50 mm^3 was randomly categorized into study groups and intravenously (IV) injected with saline, BMN, AZA, PAZA carrier, BMN/PAZA, and free BMN+AZA combination once every 3 days for 5 times. The tumor volume and body weight were measured every 3 days. After the completion of the experiment, the tumor tissue and major organs were harvested, fixed with 4% (v/v) paraformaldehyde in PBS (PH 7.4), embedded in paraffin, and sectioned into 4 μm slices. Each section was processed for H&E staining and observed under a microscope. Immunohistochemical analysis (IHC) of Ki67 protein, an important biomarker of cell proliferation, was carried out using the labeled streptavidin-biotin method. Ki67 expression was quantified by calculating the number

of Ki-67 positive cells/total number of cells in five randomly selected areas using ImmuneRatio software.

LLC-Luc orthotopic model was used to evaluate the combination effect of PAZA/BMN with PD-1 antibody, and mice were randomly categorized into study groups 10 days after surgery inoculation. PAZA carrier, BMN/PAZA combination (0.25mg/kg) was intravenously injected once every 3 days. Anti-mouse PD-1 antibody (InvivoGen) (100μg each mouse) was intraperitoneally injected once every 3 days. The tumor volume of the mice was monitored by IVIS-200 imaging. 150mg/kg D-luciferin was injected intraperitoneally for the bioluminescence imaging of each mouse.

2.2.13 Toxicity study

Biochemical parameters: Blood samples were collected after 5 injections of saline and BMN/PAZA formulations into tumor-bearing mice. The serum alanine aminotransferase (ALT), aspartate aminotransferase (AST) and creatinine levels were evaluated as indicators of hepatic and renal function.

Complete blood count (CBC): Blood samples were collected after 5 injections of saline and BMN/PAZA formulations into tumor-bearing mice. Blood sample was measured by CBC analyzer in UPMC Hillman Cancer Center.

Histology changes: Tissue section of major organ (heart, liver, spleen, lung and kidney) that collected after the therapeutic study was processed for H&E staining to test if there is morphology change to major organs after treatments[108].

2.2.14 Western blot

The expression levels of γ-H2AX, RAD51, STING, phosphorated STING, IRF3, and phosphorated IRF3 in cells and tumor tissues after various treatments were evaluated by western blot. The cells and homogenized tumor tissues after various treatments was lysed in RIPA buffer with protease inhibitor and, PhosSTOP™ phosphatase, followed by quantitated for protein using the BCA Protein Assay Kit. Equal amounts of protein were resolved by SDS-PAGE. Membranes were blocked in 5% BSA/PBST and incubated with antibodies. Immunodetection was performed using SuperSignal West Pico and Femto Chemiluminescent Substrate. Blot stripping was performed using Restore Western Blot Stripping Buffer according to the manufacturer's guidelines. Protein levels were quantified by densitometric analysis using ImageJ/Fiji. Phosphorylated protein levels were normalized to total protein band, then to loading control, and expressed as fold change versus control DMSO.

2.2.15 Immuno-fluorescence staining

DNA repair capability after various treatments was evaluated by determining the RAD51 foci via immunofluorescence staining. Cells after various treatments were washed, fixed and permeabilized in 0.25% Triton/PBS. Blocking was performed in 5% BSA/0.1% Triton/PBS, followed by incubation with primary antibodies in dilution buffer (1%BSA/0.1%Triton/PBS) (overnight, 4°C). Cells were then washed in PBS and incubated with secondary antibodies, followed by washing and mounting on coverslips using ProLong Gold antifade reagent with DAPI. Cells were imaged using Keyence BZ-X800 fluorescence microscope and analyzed using

ImageJ/Fiji software. FindFoci ImageJ plugin was used for RAD51 foci quantification, at least 5 fields were counted for foci number respectively [109].

2.2.16 Analysis of tumor-infiltrating immune cells

The immune cell populations in the tumors after various treatments were measured by flow cytometry following previous protocol [110]. Briefly, one day after the last treatment, cell suspensions from the spleens or tumors were filtered, and red blood cells lysed. Single cell suspensions were incubated with respective flow antibodies. Zombie dye was used to discriminate viable and dead cells. Infiltration of various immune cells ($CD4^+$, $CD8^+$, Treg, natural killer (NK) cells, myeloid derived suppressor cells (MDSC), dendritic cells and macrophages) in tumor tissues, the production of lymphocyte effector molecules (such as IFN-γ, perforin and granzyme B) on immune cells, and MHC-I on tumor cells was determined by multi-color flow cytometric analysis. The expression of phosphorated IRF3 and TBK1 in tumor cells and DC cells was also evaluated by flow cytometry.

2.2.17 RNAseq analysis

One day after the last treatment, the tumors were collected for RNAseq, which was performed at the Health Sciences Sequencing Core at Children's Hospital of Pittsburgh. Raw sequence data was analyzed as described in previous published protocol [111, 112] to generate transcript level gene expression. Then gene set enrichment analysis (GSEA) [113] was performed to identify the treatment-associated alteration in functional pathways.

2.2.18 Proteomic analysis

Cy3-labelled PAZA and PVD were incubated with mouse serum for 6h. The Sephadex G-100 column was used to remove unbounded protein. The PAZA or PVD with protein corona were collected and quantified based on the fluorescence intensity. Polymer-protein corona complex were then loaded in SDS-PAGE gel. Gel slice samples were sent to BGI America Mass Spec Service Center for proteomic analysis. Briefly, Gel slices were digested with Trypsin/LysC according to the standard in-gel digestion protocol [114]. Samples were then extracted, dried and reconstituted for LC-MS/MS. MS Data was searched against the most updated UniProt Mouse database. Sequest analysis workflow was used to reveal basic protein identification information.

2.3 Result

2.3.1 Preparation and characterization of ultra-small micelles

The PVD polymer backbone was synthesized by reversible addition-fragmentation chain transfer (RAFT) polymerization, and the AZA-conjugated polymer (PAZA) was obtained by conjugation of AZA to PVD backbone (**Fig. 2-1**). The structures were characterized by NMR and IR spectra (**Fig. 2-2**). PVD could form NPs with an average diameter of 100 nm in aqueous solution. Interestingly, conjugation of 6 units of AZA to PVD drastically decreased the NP size to 12.3 nm (**Fig. 2-4A**). Besides, PAZA micelles showed a low critical micelle concentration (CMC) value of 0.0076 mg/mL (**Fig. 2-4B**), indicating a likely excellent micelle stability upon dilution.

The PAZA carrier was able to load BMN into spherical NPs with drug loading capacity as high as 14.8%, which was much higher than that of PVD carrier (~5.8%) (**Fig. 2-4C, Table 2-1**).

It has been reported that reducing the particle size of polymeric micelles often compromises the encapsulation capacity and stability of drug-loaded micelles[115-118]. Intriguingly, we found that conjugation of AZA markedly reduced the nanocarrier size to 12 nm, while simultaneously enhancing drug loading efficiency. To deliver into the mechanism of interaction between the BMN molecule and PVD or PAZA polymer, we conducted molecular dynamics (MD) simulations. The model system comprised one polymer copy and eight BMN copies, with solvent effects simulated

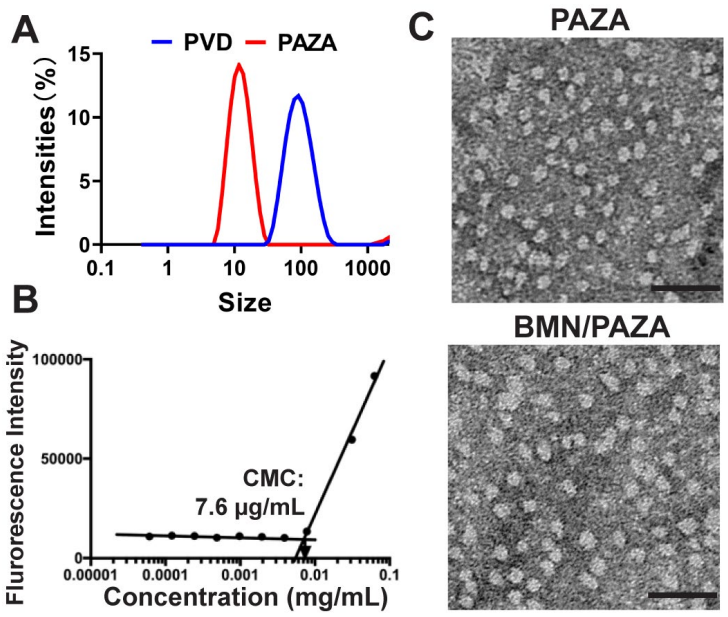

Figure 2-4. Characterization of PAZA NP

(A) Size of PVD and PAZA micelles. (B) Critical micelle concentration of PAZA polymer. (C) Morphology of PAZA and BMN loaded PAZA by TEM.

through explicit water MD and a subsequent Generalized Born surface area (GBSA) model. After a series of MD simulations, micelle structures were formed for both PAZA (**Fig. 2-5A**) and PVD polymers (**Fig. 2-5B**). It was shown that the conjugation of AZA induced a reconfiguration of the

polymer segments, facilitating the formation of more stable micelles with a tighter packing of the hydrophobic core (brownish sticks) compared to PVD. In swarm MD simulations, BMN formed

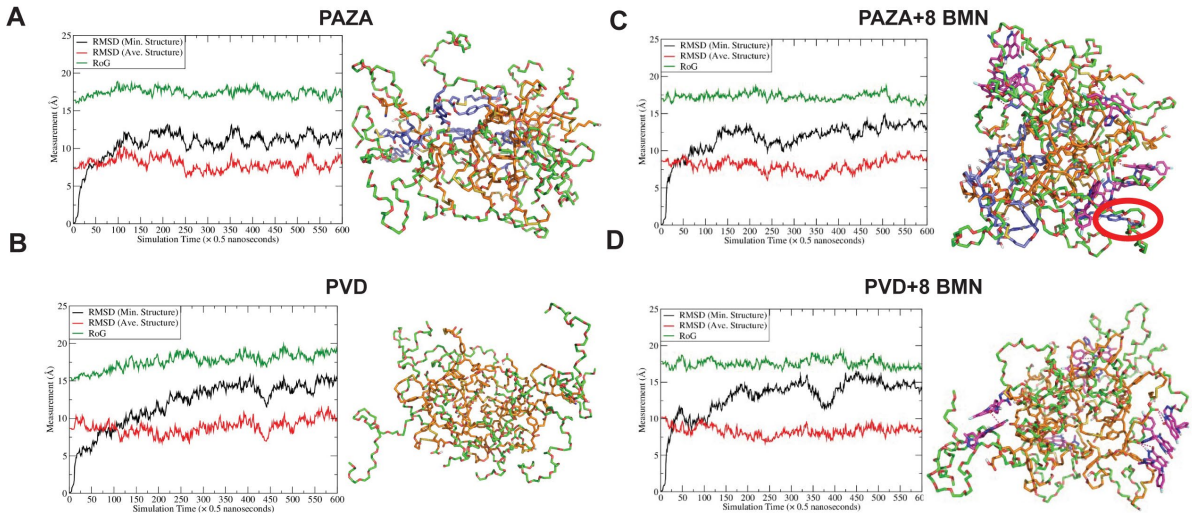

Figure 2-5. Modeling of PAZA NP.

Time courses of root-mean-square deviations (RMSD) of heavy atoms and radius of gyration (RoG) and representative conformations of **(A)** PAZA**; (B)** PVD; **(C)** PAZA+8 BMN molecules; **(D)** PVD + 8 BMN molecules. The following color schemes were applied: greenish sticks for hydrophobic parts of the residues, brownish sticks for hydrophilic parts of the residues, and magenta sticks for the AZA substructure. Red cycle: π-π interactions moiety between PAZA and BMN.

similar hydrogen bonding with both PVD and PAZA with 2.32 and 2.36 hydrogen-bonds on average, respectively. However, BMN showed stronger π-π interactions with PAZA than with PVD, which comes from pyrimidine ring of AZA (**Fig. 2-5C&D**).

Molecular Mechanics/Poisson-Boltzmann Surface Area - Water Solvent Accessible Surface (MM-PBSA-WSAS) method was used to estimate the free energy of binding between BMN and the nanocarriers, providing insights into the thermodynamics of drug encapsulation within the nanocarriers. We first calculated MM-PBSA-WSAS free energies for BMN itself, PAZA or PVD polymer itself, and PAZA + 8 BMN and PVD + 8 BMN. Then we calculated the free energy change upon BMN binding, $\Delta G_{binding} = G_{complex} - (G_{polyer} + 8 \times G_{BMN})$. The calculated $\Delta G_{binding}$ values were -44.43 and -38.16 kcal/mol for PAZA and PVD, respectively.

This result explained why PAZA has better loading capacity than PVD. Moreover, we calculated the root-mean-square deviation (RMSD) of the heavy atoms to describe the dynamics of the polymer and polymer-drug complex. PAZA/BMN complex exhibited higher stability than PVD/BMN complex, as evidenced by the smaller fluctuation in the RMSD values for the former (black curves of **Fig. 2-5C&D**).

Fig. 2-6A shows the model we proposed to elucidate the improved performance of PAZA. The formation of large micelles by the PVD polymer can be attributed to the mechanism of multi-micelle aggregates, wherein the initially formed small micelles exhibit limited stability, resulting in rapid flocculation and the subsequent formation of larger multi-micelle aggregates[119]. In contrast, for PAZA, the hydroxyl groups of AZA molecules at the interface can engage in hydrogen

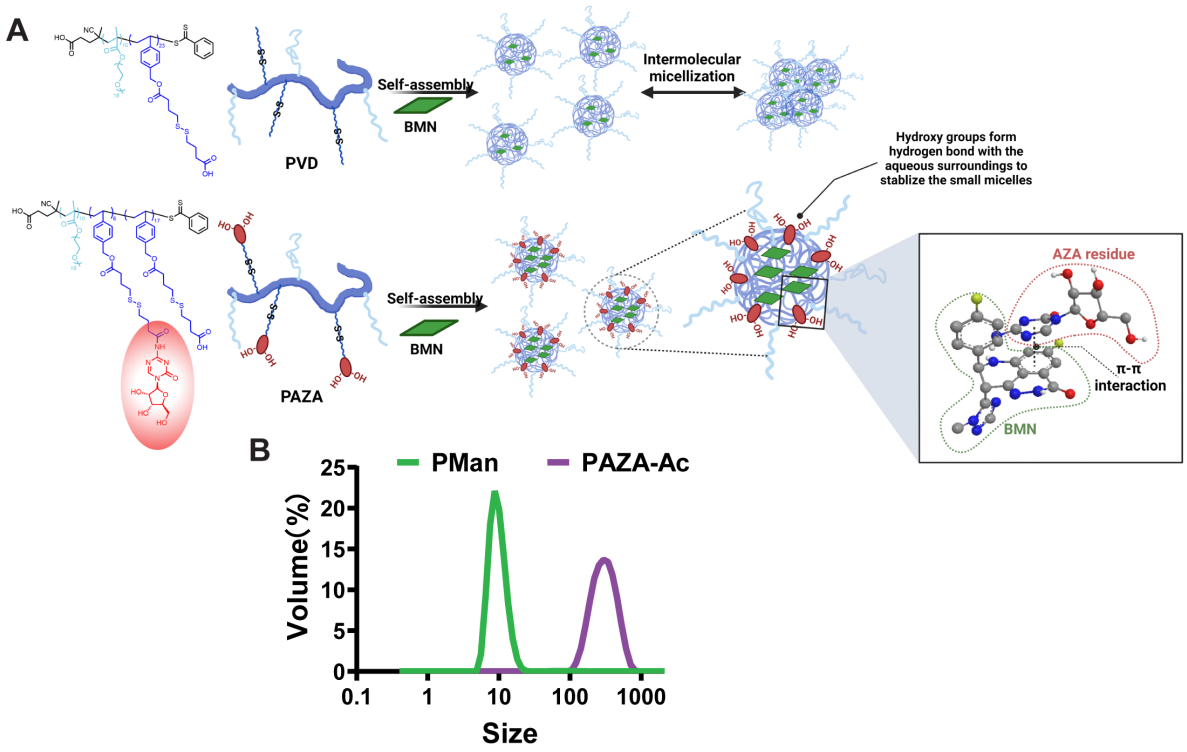

Figure 2-6. Self-assemble and drug loading mechanism of PVD and PAZA.

(A) Illustration of the proposed self-assemble and drug loading mechanism of PVD and PAZA. (B) Validation of proposed mechanism with the size of acetylated-PAZA (PAZA-Ac) and PMan micelle.

bonding with the aqueous surroundings, thereby stabilizing the initially formed small micelles. In addition, the π-π interaction between the pyrimidine ring of AZA and BMN (**Fig. 2-5C**&**D**) helps to improve both BMN loading capacity and the formulation stability. To further test our model, we synthesized the acetalized PAZA (PAZA-ac) to eliminate the effect of hydrogen bond of PAZA. We also synthesized mannitol conjugated PVD (PMan) to attenuate the π-π interaction between the pyrimidine ring of AZA and BMN (**Fig. 2-3B)**. As shown in **Fig. 2-6B**, PAZA-ac showed drastically increased size, but PMan was able to maintain the ultra-small size, suggesting that the hydroxyl group of AZA played an important role in forming the ultrasmall micelle. In addition, PMan suffered a significant drop in drug loading capacity compared to PAZA (**Table. 2-1**), suggesting that the pyrimidine ring of AZA contributed significantly to BMN loading through π-π interaction (**Fig. 2-6A**). This information might be of value in the future design of other ultrasmall-sized drug formulations.

Table 2-1. Drug loading parameters and size of BMN loaded PVD, PAZA and PMan.

Micelles	Weight Ratio (polymer /BMN)	Size(nm)	BMN loading efficiency	BMN loading capacity
BMN/PVD	10:1	100.60	57.7%	5.77%
BMN/PAZA	5:1	12.95	74.2%	14.84%
	10:1	12.74	80.3%	8.03%
	20:1	11.90	81.2%	4.37%
BMN/PMAN	5:1	108.37	24.7%	4.93%
	10:1	151.40	33.9%	3.40%
	20:1	27.50	59.6%	2.98%

In addition to improved performance in loading a drug, PAZA can protect AZA from enzymatic degradation. PAZA is a redox-responsive self-immolative carrier which can release the parent AZA due to the formation of thiolan-2-one (**Fig. 2-7A**). The release study showed that no AZA was released from PAZA in the PBS (pH 7.4) without GSH, but fast release of AZA was observed in the presence of 10mM GSH (**Fig. 2-7B**). The accumulative amount of released AZA was decreased after 12 h likely due to that the released AZA was not stable in aqueous solution and gradually hydrolyzed to ribosylguanylurea[120] (**Fig. 2-7A**). Moreover, in contrast to the rapid intracellular degradation observed with free AZA treatment, PAZA demonstrated a sustained

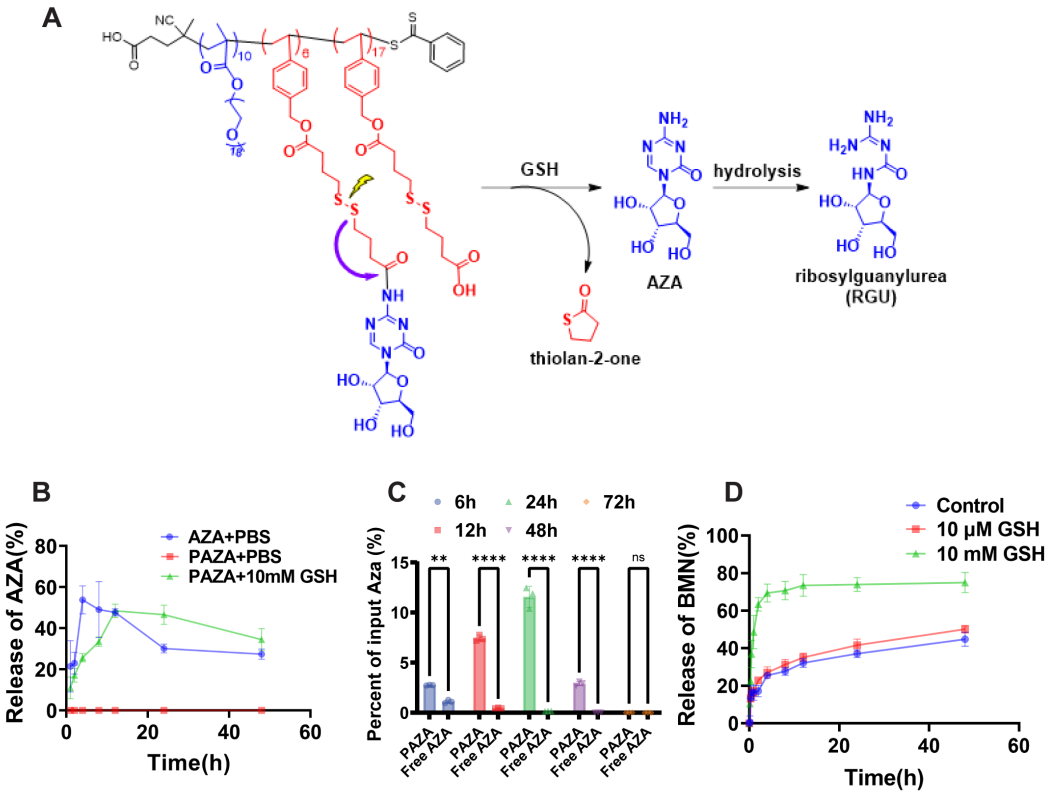

Figure 2-7. Release profile of AZA and BMN673 in PAZA NP.

(A) Scheme of the self-immolative release of AZA from PAZA under redox condition. (B) Release of AZA from PAZA under redox condition. (C) Intracellular release of AZA from PAZA (n=3, *p < 0.05, **p < 0.01, ***p < 0.001, ****p<0.0001). (D) In vitro release of BMN from PAZA under different GSH concentrations.

release of AZA, maintaining significantly higher intracellular drug concentrations for 48 h. This further underscores the excellent protective effect of PAZA nanocarrier in AZA delivery (**Fig. 2-7C**). We also assessed the release kinetics of BMN from the BMN/PAZA formulation. In its absence or low GSH environment, only less than 25% of BMN loaded in PAZA was released in 2 h, and the slow kinetics of release was extended for 48 h. However, upon exposure to 10 mM GSH, the release of BMN from the PAZA micelles was greatly accelerated and more than 60% BMN was released. The accelerated drug release is likely due to the disassembly of the micelles, which was induced by the cleavage of disulfide link (**Fig. 2-7D**).

2.3.2 Efficient tumor penetration via clathrin-mediated transcytosis

Utilizing an LLC mouse tumor model, we analyzed the tumor-targeting efficiency of PAZA carrier through NIR imaging and compared it to the larger PVD NPs (**Fig. 2-8A**). Notably, tumors treated with DiR/PAZA displayed more fluorescence signals compared to DiR/PVD-treated tumors, which was further supported by the quantification (**Fig.2-8B**). The LLC tumors treated with DiR/PAZA and DiR/PVD NPs were further frozen sectioned for penetration study. More DiR signals were observed in the core of tumors treated with DiR/PAZA NPs compared to tumors treated with DiR/PVD NPs, indicating the superior penetration capacity of PAZA carrier in the LLC tumor core (**Fig. 2-8C**).

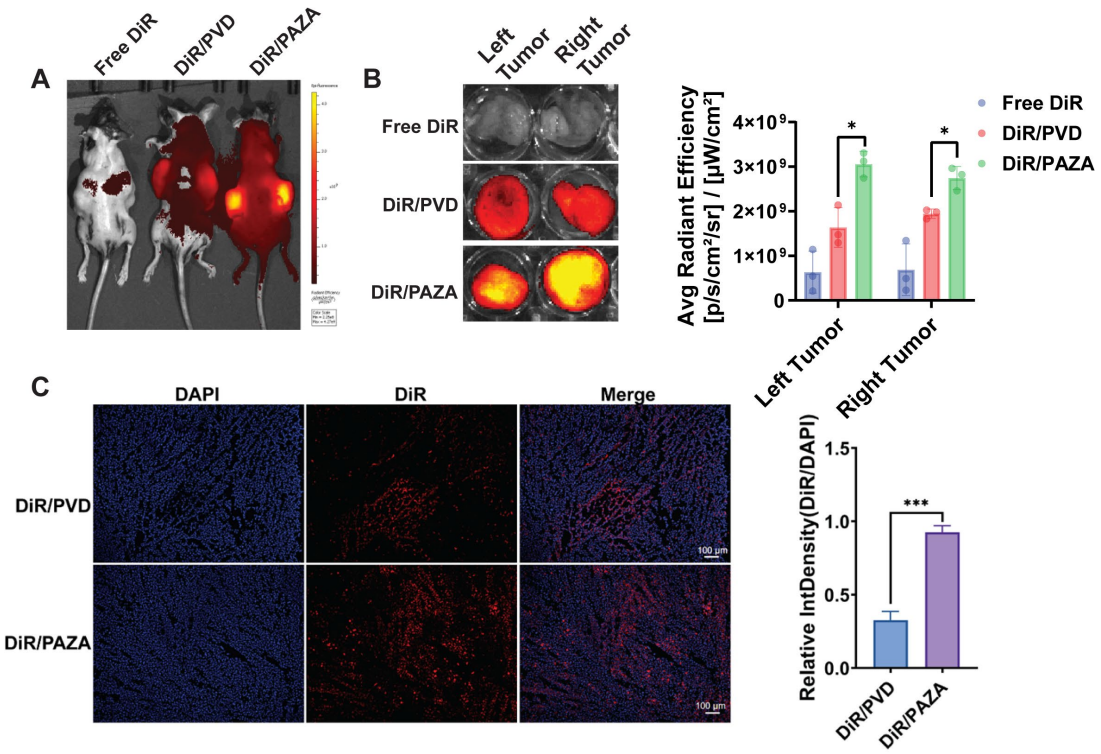

Figure 2-8. Tumor accumulation of PAZA NP.

(A) In vivo NIR images and (B) Ex vivo NIR images and quantification of tumors of each mouse treated with DiR-labeled PVD and PAZA, respectively, at 24 h. (n=3, data are presented as mean ± s.d. *p < 0.05, **p < 0.01, ***p < 0.001, ****p<0.0001). (C) Fluorescence images and quantification of frozen tumor core sections at 24 h after treatment with DiR-loaded PVD and PAZA micelles, respectively (n=3, Data are presented as mean ± s.d. *p < 0.05, **p < 0.01, ***p < 0.001, ****p<0.0001).

To investigate the underpinning mechanism behind the enhanced tumor penetration of PAZA, we used different inhibitors of endocytic pathways [104] and found that the cellular uptake of both PAZA and PVD carriers was significantly decreased after pre-incubation with chlorpromazine, suggesting that both of them were taken up by LLC cells mainly through clathrin-mediated endocytosis (**Fig. 2-9A, Table. 2-2**). The 3D cell spheroids model showed that smaller PAZA were capable of penetrating deeper within tumor spheroids than the larger PVD particles (**Fig. 2-9B**). Such deep penetration was significantly suppressed by chlorpromazine, indicating that endocytosis may also play a role in tumor penetration. Then, we investigated if the deep tumor penetration of PAZA is mediated by transcytosis pathway via an *in vitro* transwell assay in multi-

layer LLC tumor cells model (**Fig. 2-9C**). By determining the fluorescence intensity in the medium of lower chamber, we found that PAZA carrier was more effective in penetrating through multilayer tumor cells than PVD carrier (**Fig. 2-9D**). In addition, the penetration of PAZA was

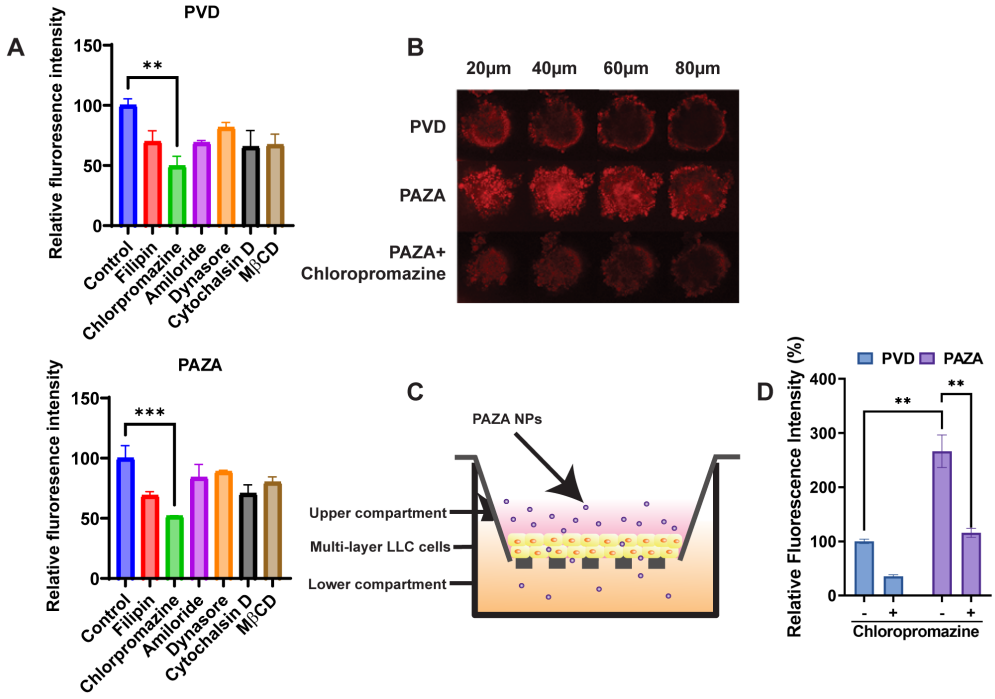

Figure 2-9. PAZA penetrate tumor through transcytosis-mediated process.

(A) Cellular uptake of PVD and PAZA after treated with various inhibitors of endocytic proteins, represented by the quantitative median fluorescence intensity. n=3, data are presented as mean ± s.d. **p < 0.01, ***p<0.001. (B) Confocal z-stack images of LLC tumor cell spheroids after 18 h incubation with Rhodamine-labeled PVD and PAZA NPs, or Rhodamine-labeled PAZA NPs that had been pretreated with endocytosis inhibitor chlorpromazine. (C) Illustration of in vitro transwell assay in multilayer LLC cells and (D) Relative fluorescence intensity of lower chamber medium after 6 h incubation with rhodamine-labeled PVD and PAZA (with or without pretreatment of endocytosis inhibitor chlorpromazine for 1 h) at upper chamber. The fluorescence intensity of each group was compared with the fluorescence intensity of PVD without chlorpromazine treatment group. (n=3, Data are presented as mean ± s.d. *p < 0.05, **p < 0.01, ***p < 0.001, ****p<0.0001).

greatly inhibited by preincubation with chlorpromazine, indicating the PAZA carrier penetrated deeply into the core of the tumor primarily through the clathrin-mediated transcytosis rather than paracellular transport due to its smaller size.

Table 2-2. Logic matrix illustrating the effects of chemical inhibitors we used on different endocytic pathways.

	Targeted endocytosis pathway			
	Clathrin-Mediated	**Caveolin-Mediated**	**Macropinocytosis**	**Phagocytosis**
Filipin		×		
Chlorpromazine	×			
Amiloride			×	
Dynasore	×			
Cytochalasin D				×
MβCD		×		

2.3.3 The role of fibronectin-ITGA5 in mediating tumor cell transcytosis

To elucidate the mechanism underlying the effective transcytosis mediated by the ligand-free, ultrasmall NPs compared to the large-sized counterpart, we evaluated how PAZA and PVD engage with the initial biological milieu they encounter upon intravenous administration. Accumulating evidence demonstrated the tendency for most NPs to acquire a coating of serum protein corona post intravenous injection even when using an anti-fouling polymer such as PEG[121, 122]. The PC imparts the NPs with a new biological identity, intricately molding NP interactions within complex biological systems. To study whether PAZA and PVD interact with serum differently and whether such difference contributes to their tumor targeting and penetration efficiency, we conducted proteomics analysis of the protein corona of PVD and PAZA NPs following the exposure to mouse serum. Remarkably, fibronectin (FN) emerged as a key player, being significantly more enriched in the protein corona of PAZA as opposed to that of PVD (**Fig.**

2-10A, Table 2-3). Fibronectin, a crucial glycoprotein, facilitates cell adhesion, migration, and signaling[123]. It possesses specific binding sequences such as the RGD motif (arginine-glycine-aspartic acid) that can selectively interact with the integrin receptors such as ITGA5 that are significantly upregulated on tumor cells and tumor endothelial cells[124, 125].

Table 2-3. Significantly enriched proteins in protein corona in PAZA compared to PVD.

Protein	Relative abundance (Log)[PAZA/PVD)
C4b-binding protein	3.17
Fibronectin	2.74
Lysosomal alpha-mannosidase	2.58
Vinculin	2.32
Fibrinogen alpha chain	2.00
Odorant-binding protein 1b	2.00
Coagulation factor XIII A chain	1.81
Complement C1r-A subcomponent	1.74
Complement C5	1.58
Coagulation factor IX	1.58
Vitamin K-dependent protein C	1.58
Lipopolysaccharide-binding protein	1.58
Major urinary protein 3	1.58
Complement factor H	1.55
Coagulation factor VII	1.41

To investigate if FN in the serum indeed plays a role in the tumor targeting of PAZA, we initially assessed how the serum proteins, especially FN affects the interactions of PAZA or PVD with cultured tumor cells by quantitative flow analysis (**Fig. 2-10B**). There was significantly more cell binding/uptake of PAZA NPs compared to PVD NPs in a study with complete medium.

However, the cellular interaction of both NPs was significantly inhibited when serum-depleted medium was used. The decreases in cellular uptake were rescued for both NPs, especially PAZA NPs, when FN was added to the serum-free medium. Importantly, the cellular uptake of PAZA

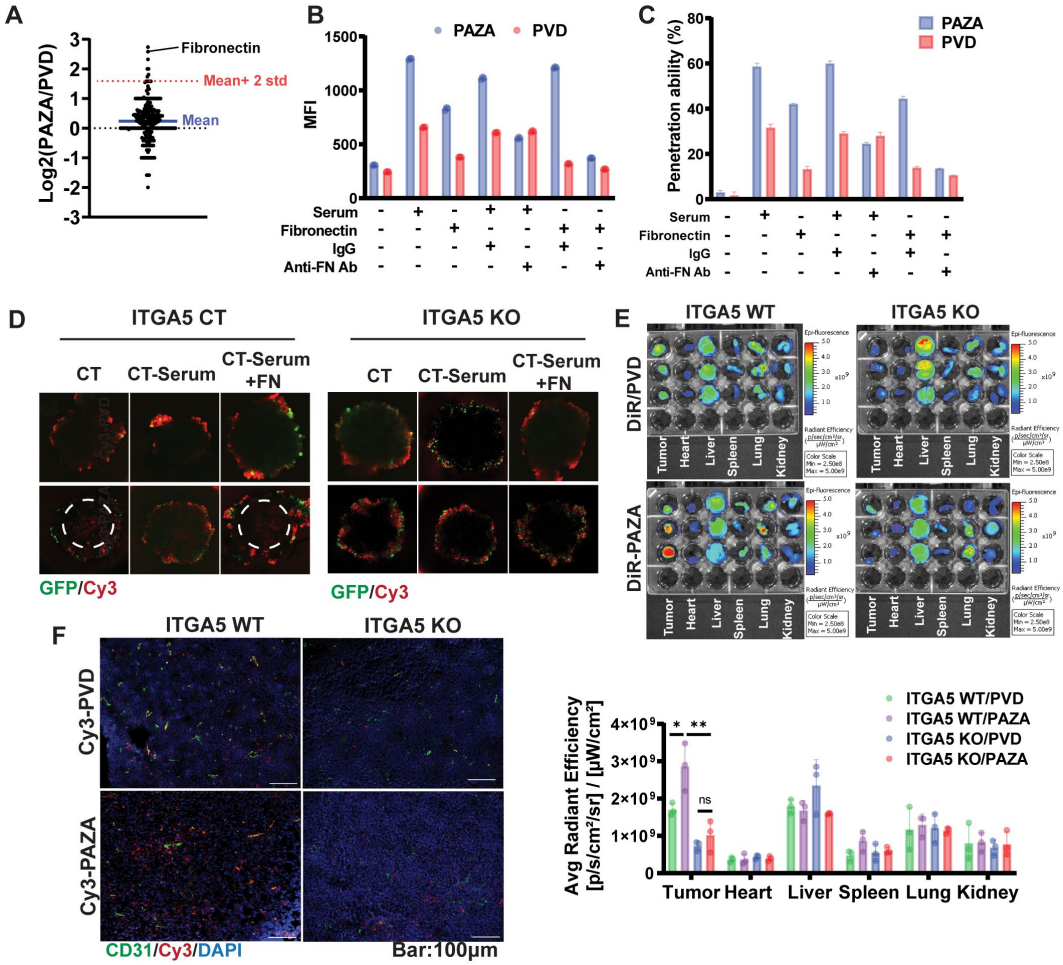

Figure 2-10. Fibronectin mediates the transcytosis of PAZA NPs.

(A) Difference of various protein amount in the protein corona on PVD & PAZA. (B) Quantification of cellular uptake by flow cytometry of Cy3-labeled PVD and PAZA by LLC cells with blank medium or medium with various supplements. (C) Transwell assay of transmigration of Cy3 labeled PAZA or PVD across multilayer LLC cells with blank medium or medium with various supplements, respectively. (D) Confocal z-stack images of middle sections of ITGA5 Control or KO LLC-GFP spheroids after 18 h incubation with Cy3-labeled PAZA or PVD with serum (CT), without serum (CT-Serum) or FN supplement in the medium without serum (CT-Serum+FN). (E) Ex vivo imaging of ITGA5 WT or KO mice and quantification at 24 h following i.v. administration of DiR-loaded, Cy3-labled PAZA or PVD. N=3. Data are presented as mean ± s.d. *$p < 0.05$, **$p < 0.01$. (F) Fluorescence images of frozen tumor core sections from ITGA5 WT or KO tumor at 24 h after treatment with Cy3-labled PVD and PAZA NPs. CD31 was stained with FITC-labeled antibody to show the blood vessels. Bar=100 μm.

NPs in complete medium or FN-supplemented medium was significantly attenuated by ITGA5-specific antibody but not by a control IgG. These data suggest a role of FN/ITGA5 specific interaction in mediating the endocytosis of PAZA NPs by tumor cells.

serum or ITGA5-specific antibody (**Fig. 2-10C**), suggesting that FN/ITGA5 interaction also contributed significantly to the effective tumor transcytosis. Notably, the NPs exhibited slightly lower penetration ability in the presence of FN compared to that in the serum, indicating that other proteins are also involved in the tumor targeting and penetration of PAZA but to a much lesser extent. Moreover, in tumor sphere studies with wild-type LLC cells, PAZA's penetration was hindered by serum deprivation but was partially restored with fibronectin addition, emphasizing its key role in tumor penetration. However, the ITGA5 KO tumor sphere nearly abolished this effect, even when fibronectin was reintroduced (**Fig. 2-10D**), further confirming a critical interplay between fibronectin and ITGA5 in mediating efficient tumor penetration of PAZA. To establish the *in vivo* significance of the above studies, the *in vivo* distribution of PVD and PAZA was also evaluated in mice bearing ITGA5 KO tumors. As shown in **Fig. 2-10E&F**, the superior tumor accumulation and penetration of PAZA over PVD was abolished when ITGA5 was knocked out in tumors. Taken together, our data suggest that the superior tumor targeting and penetration of PAZA NPs was attributed to the *in-situ* formation of FN-enriched protein corona after intravenous administration, which promoted transcytosis in the tumor tissue through FN-ITGA interaction.

2.3.4 PAZA carrier sensitized HR-proficient cancer to BMN

Following the mechanistic study of tumor targeting and penetration, we evaluated the therapeutic efficacy of PAZA nanocarrier loaded with BMN673. Free AZA and BMN673 showed a synergistic cell-killing effect with a combination index (CI<1) in two NSCLC cell lines, LLC and A549, at various dose combinations (**Fig. 2-11A).** PAZA prodrug carrier showed comparable cytotoxicity compared to free AZA in LLC and A549 cells. Compared to PAZA and BMN alone,

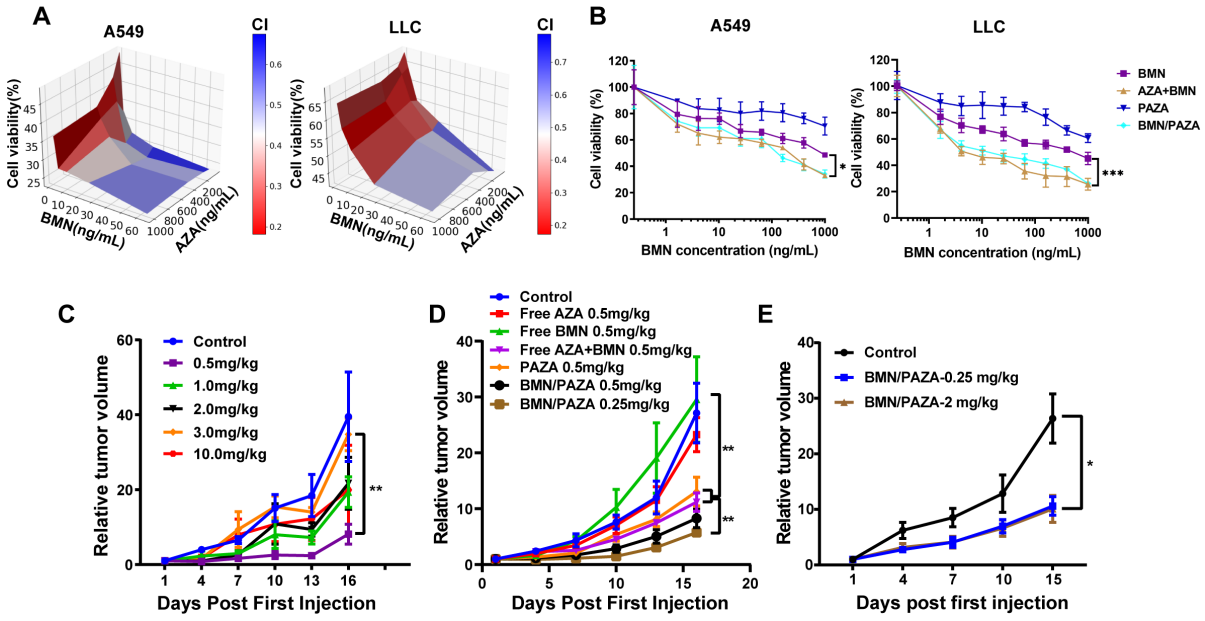

Figure 2-11. BMN/PAZA shows enhanced anti-tumor effect on BRCA-proficient NSCLC.

(A) Combination index (CI) of various AZA and BMN dosage on A549 and LLC cell lines. CI was calculated based on MTT cytotoxicity assay. (B) MTT cytotoxicity assay of various formulations in A549 and LLC cell lines. (n=6 biologically independent samples, and the data are presented as the mean±s.d. *p < 0.05, **p < 0.01, ***p < 0.001.) (C) Relative tumor volume changes of the C57BL/6 mice treated with BMN/PAZA at the different BMN and AZA dosages (the dosage of BMN and AZA is same, n=3 biologically independent samples, and the data are presented as the mean ± s.d. *p < 0.05, **p < 0.01, ***p < 0.001). (D) Relative tumor volume changes of the C57BL/6 mice treated with various formulations with free BMN and AZA as controls (n=5 biologically independent samples, and the data are presented as the mean ± s.d., *p < 0.05, **p < 0.01, ***p < 0.001). (E) Relative tumor volume changes of the LLC tumor-bearing nude mice treated with two different BMN/PAZA NPs: BMN/PAZA-0.25 (0.25 mg/kg of BMN and AZA), and BMN/PAZA-2 (2 mg/kg of BMN and AZA). (n=4 biologically independent samples, and the data are presented as the mean±s.e.m, *p < 0.05, **p < 0.01, ***p < 0.001).

incorporation of BMN into PAZA further increased the cytotoxicity (**Fig. 2-11B**). Compared to the combination of free AZA and BMN, BMN/PAZA showed similar cytotoxicity.

Fig. 2-11C shows the *in vivo* therapeutic efficacies of BMN/PAZA formulations with various dosages in LLC tumor-bearing C57BL/6 mice. Surprisingly, simultaneously decreasing the dose of AZA and BMN led to increased therapeutic efficacy. The formulation showed higher therapeutic effect at a lower dosage (0.5 mg/kg of both AZA and BMN). Then, we evaluated the therapeutic effect of BMN/PAZA formulations with free AZA and BMN as controls (**Fig. 2-11D**). At a dosage of 0.5 mg/kg for both BMN and AZA, BMN alone showed no effect in inhibiting the tumor growth in BRCA-proficient LLC tumor model, while free AZA only slightly inhibited the tumor growth. PAZA was more effective in inhibiting the tumor growth than free AZA. Combination of AZA and BMN showed higher therapeutic effect than the single drugs, and BMN-loaded PAZA NPs showed the best therapeutic antitumor efficacy. **Fig. 2-11D** also shows that reducing the dose of both AZA/BMN to 0.25 mg/kg in BMN/PAZA formulation led to further improvement in antitumor activity. To further gain the insight of the dose effect, we evaluated the antitumor activity of BMN/PAZA in LLC tumors grown in nude mice (**Fig. 2-11E**). In this immunodeficient mouse model, there was no difference between the two groups (2 mg/kg vs 0.25 mg/kg) in tumor growth inhibition, indicating that the higher therapeutic efficacy for BMN/PAZA formulation at lower dosage (0.25 mg/kg) in immunocompetent mice might be attributed to a more favorable immune response.

In addition, the BMN/PAZA formulation was well tolerated with no significant changes in body weight (**Fig. 2-12A&B**), serum levels of ALT, AST, and creatinine (**Fig. 2-12C-E**), and histology of major organs (**Fig. 2-12F**). However, there was a slight increase in the ALT and AST

levels after treatment with free BMN and AZA combination, indicating that loading BMN into PAZA carrier decreased the potential liver toxicity for the combination therapy.

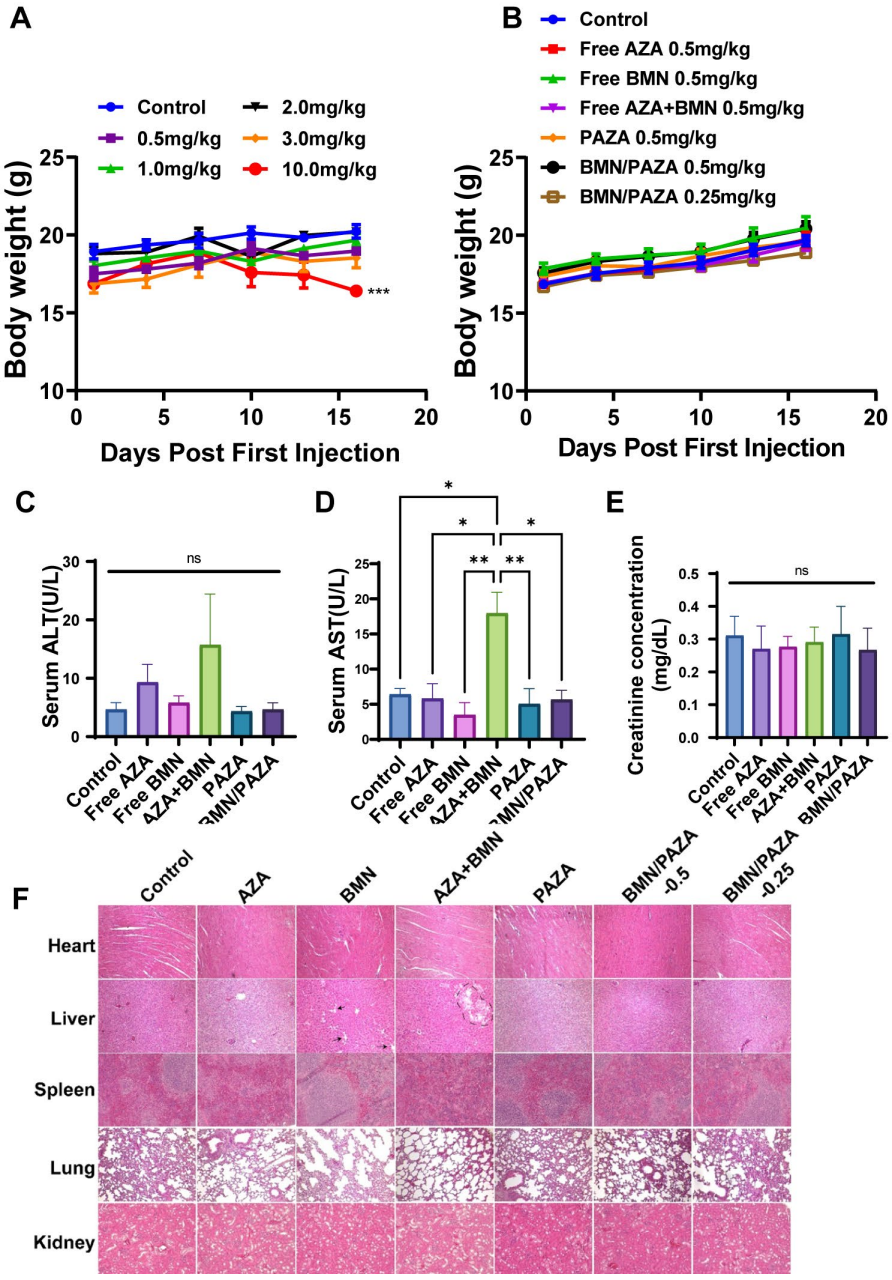

Figure 2-12. Safety profile of BMN/PAZA.

(A) The change of body weight in 2-10C, *p < 0.05, **p < 0.01, ***p < 0.001. (B) The change of mice body weight in 2-10D. (C-E) Serum level of ALT, AST, and creatinine after various treatments. The dose of both BMN and AZA is 0.5mg/kg. n=3, data are presented as mean±s.d. *p < 0.05, **p < 0.01, ***p < 0.001. (F) H&E staining of major organs after various treatments for 5 times.

2.3.5 PAZA carrier produced DNA repair dysfunction and enhanced the DNA damage induced by BMN

To gain the mechanistic insight into the enhanced therapeutic efficacy of BMN/PAZA and the dose effect, RNA sequencing (RNA-Seq) of tumor tissues after various treatments was analyzed. GSEA also showed that DNA repair pathway was significantly inhibited in BMN/PAZA-treated tumors versus tumors treated with BMN alone **(Fig. 2-13A&B)**, indicating that delivery of BMN using epigenetic-regulating carrier PAZA may produce DNA repair dysfunction and enhance the DNA damage levels. To test this hypothesis, the DSB levels in cultured LLC cells after various treatments were first evaluated by Western blot using γ-H2AX as a DNA damage marker. Free AZA treatment didn't increase the protein expression levels of γ-H2AX and free BMN treatment led to a small increase in γ-H2AX levels in LLC cells (**Fig. 2-13C**). Combination of free AZA and BMN or incorporation of BMN into PAZA further increased the levels of γ-H2AX. We also found that compared to lower dose of AZA, higher dose of AZA (A3) was less effective in synergizing with BMN to induce DNA damage (**Fig. 2-13D**). It is well known that AZA only works as epigenetic modifiers to inhibit DNA methylation when given at low doses. At high doses, it leads to cell death through inhibition of DNA synthesis, which short-circuits its DNA hypomethylating effect [126]. Our studies indicated that compared to the inhibition effect of DNA synthesis, the epigenetic modulation effect of AZA may play a more important role in the synergy between AZA and BMN in increasing the DSBs. At high doses, AZA

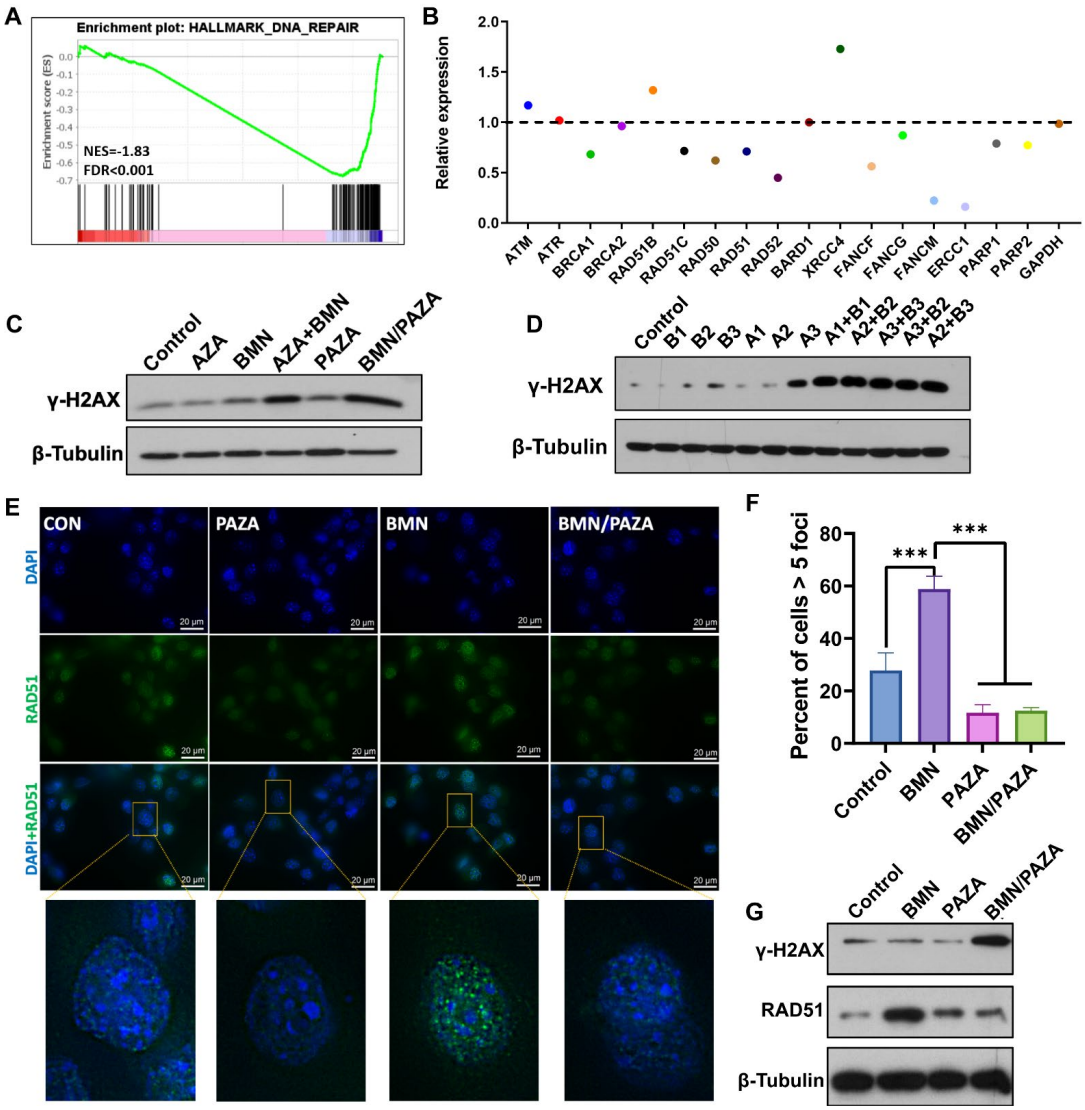

Figure 2-13. BMN/PAZA combination synergistically induced DNA repair dysfunction and DNA damage.

(A) Gene Set Enrichment Analysis of transcriptional profiles in DNA repair pathway (BMN/PAZA vs BMN). (B) The relative expression level of canonical DNA repair genes in BMN/PAZA treated group (compared to BMN treated group). (C) The γ-H2AX expression levels in LLC cells after various treatments at the BMN dose of 500 nM (BMN: PAZA=1: 20). (D) The γ-H2AX expression levels in LLC cells treated with different doses of free AZA (A) and free BMN (B). B1: 40 ng/mL BMN, B2: 200 ng/mL BMN, B3: 1000 ng/mL; A1, A2, A3 are the AZA concentrations corresponding to B1, B2, B3. (E) Fluorescence images of RAD51 foci (green) in LLC cell at 48 h after treatment with PAZA, BMN and BMN/PAZA (Scale bar: 20 μm). (F) The percent of Rad51 foci positive cells after various treatments. (n=3 biologically independent samples. Data are presented as mean±s.d, *$p < 0.05$, **$p < 0.01$, ***$p < 0.001$) (G) Protein levels of RAD51 and γ-H2AX in tumor tissues after various treatments.

largely causes non-specific toxicity, which may also be attributed to immunosuppression as

detailed later (**Fig. 2-14**).

BMN treatment alone increased RAD51 foci, a surrogate HR repair marker, in LLC cells. However, incorporation of BMN into PAZA led to a significantly decreased level of RAD51 foci (**Fig. 2-13E**). This were further confirmed by the quantification of the number of RAD51 foci-positive cells (**Fig. 2-13F**) and *in vivo* RAD51 expression in tumor tissues (**Fig. 2-13G**), indicating that BMN treatment induced HR response and DNA repair, which could be reduced by PAZA treatment. All data above indicated that the enhanced synthetic lethality of BMN/PAZA was attributed to the DNA repair dysfunction that was brought by PAZA combination treatment.

2.3.6 BMN/PAZA increased innate and adaptive anti-tumor immune responses

As indicated by **Fig. 2-11**, the antitumor immune response may contribute to the better therapeutic efficacy of BMN/PAZA at a lower dose in immunocompetent murine model. As an initial step to test this hypothesis, we used CIBERSORT[127] to analyze our RNA-seq data to evaluate the predicted infiltration of immune cells in the tumors treated with formulations at

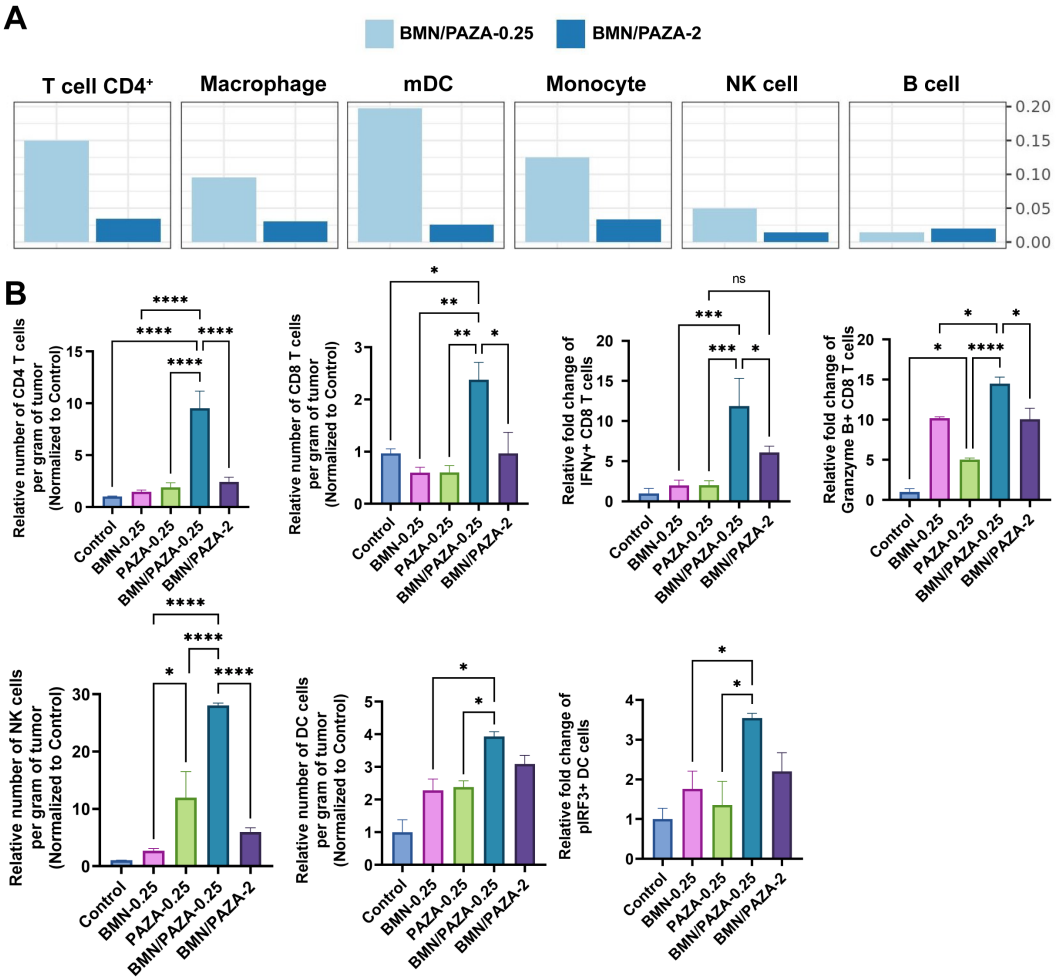

Figure 2-14. The anti-tumor immune response elicited by BMN/PAZA combination is dose dependent.

(A) Immune cell infiltration profiles predicted by CIBERSORT based on RNA-seq data. (B) Representative flow cytometric analysis and the quantification for the relative abundance of $CD8^+$ T-cell, $CD4^+$ T-cell, NK cell, dendritic cell (DC), $IFN\gamma^+CD8^+$ T-cell, Granzyme B^+CD8^+ T-cell, $pIRF3^+$ DC in tumor tissue after various treatments (n=3, data are presented as mean±s.d, *$p < 0.05$, **$p < 0.01$, ***$p < 0.001$).

different doses (**Fig. 2-14A**). It is also apparent from **Fig. 2-14A** that increasing the dose to 2 mg/kg led to significant decreases in the numbers of these immune cells despite that this dose was well tolerated as shown in other toxicity profiles.

Flow cytometry showed that BMN or PAZA treatment led to an increase in the numbers of NK and DC cells, but no significant changes in CD4 and CD8 T cells in the tumors (**Fig. 2-**

14B). In comparison, BMN/PAZA formulation at the same dose (0.25 mg/kg for BMN and AZA) led to significant increases in the numbers of these immune cells in the tumor tissues. Furthermore, compared to BMN or PAZA, BMN/PAZA combination treatment led to significant increases in the population of IFNγ^+ CD8 T cell and Granzyme B^+ CD8 T cells, suggesting significant activation of functional T-cells (**Fig. 2-14B**). It should be noted that the improvement in immune profile of BMN/PAZA was significantly diminished at a higher dose (**Fig. 2-14B**). This data, together with the data of decreased therapeutic efficacy of BMN/PAZA at the higher dose, strongly supports an important role of immune response in the overall therapeutic efficacy of BMN/PAZA.

RNA-seq analysis of BMN/PAZA-treated tumors revealed significant gene enrichment in cytosolic DNA sensing pathway and Type I IFN pathway compared to BMN group (**Fig. 2-15A**). The western blot assay further confirmed that loading BMN into PAZA carrier activated the STING pathway by increasing the protein expression of the phosphorylated STING (pSTING) and the downstream phosphorylated IRF-3 (pIRF-3) in the tumors (**Fig. 2-15B**). BMN/PAZA formulation was also more effective in eliciting the STING activation at a lower dosage. We also assessed the IFNβ and MHCI expression levels after various treatments (**Fig. 2-15C**). While BMN or PAZA alone was not effective in inducing the expression of IFNβ and MHCI, BMN/PAZA showed strong induction of both IFNβ and MHCI, which was also more drastic at a lower dosage. These data indicated that BMN/PAZA combination showed significant synergy in eliciting innate immune response that subsequently further boosts the adaptive immune responses. In addition to providing an effective strategy for improving the efficacy of synthetic lethality therapy for HR-proficient NSCLC, BMN/PAZA shall represent a safe therapy due to its unique dose-response profile. Safety shall also benefit from the improvement in tumor-selective delivery.

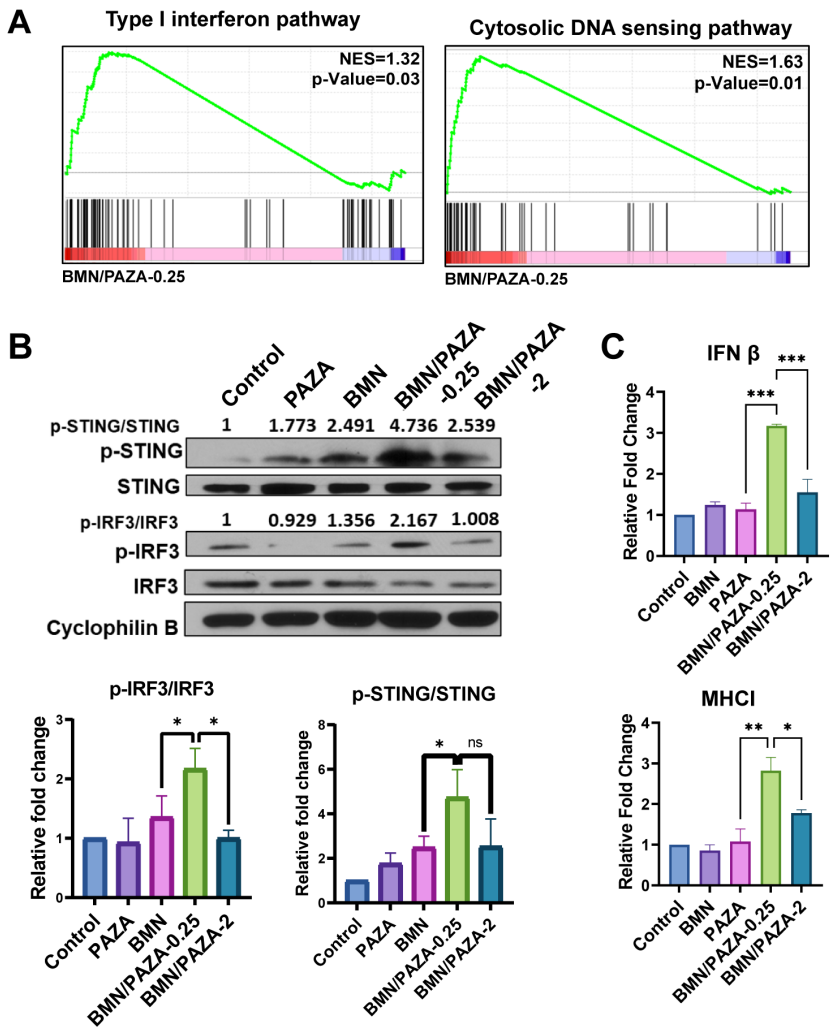

Figure 2-15. The anti-tumor immune response elicited by BMN/PAZA combination is through activation of STING-Type 1 IFN pathway.

(A) Gene Set Enrichment Analysis (GSEA) of transcriptional profiles of BMN/PAZA-0.25 versus BMN in Type I interferon pathway and Cytosolic DNA sensing pathway. (B) The protein levels of p-STING, STING, p-IRF3 and IRF3 in mouse LLC tumor tissues after treatments with PAZA. (C) The mRNA levels of IFN β and MHCI (n=3, data are presented as mean±s.d, *p < 0.05, **p < 0.01, ***p < 0.001).

2.3.7 BMN/PAZA synergized with aPD-1 in an orthotopic model of lung cancer

In addition to an overall improvement in the immune landscape, BMN/PAZA treatment led to upregulation of PDL1 expression (**Fig. 2-16A**) in tumor cells, indicating the potential benefit from combination therapy with PD-1 antibody (aPD-1) [128-130]. To examine the therapeutic

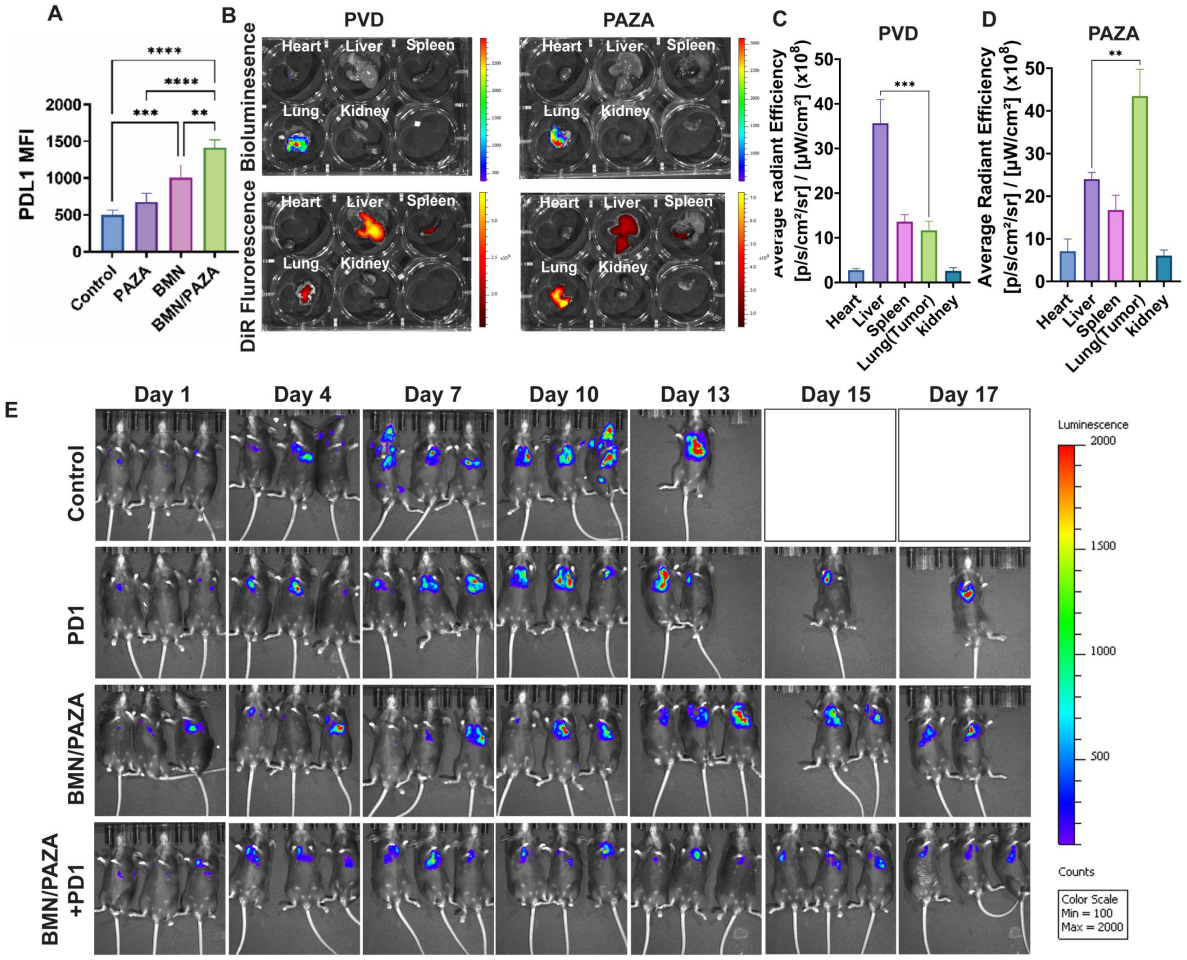

Figure 2-16. BMN/PAZA in combination with PD-L1 blockade inhibit tumor growth in orthotopic model.

(A) Flow cytometry analysis of PD-L1 expression on LLC cell after treatment with BMN, PAZA, or BMN/PAZA complex. n=3. Data are presented as mean±s.d. *$p < 0.05$, **$p < 0.01$, ***$p < 0.001$, ****$p < 0.0001$. (B) Bioluminescence and ex vivo NIR images of major organs and lung orthotopic tumors of each mouse treated with DiR-labeled PVD and PAZA respectively at 24 h. (C-D) Quantification ex-vivo image of (C) PVD and (D) PAZA (n=3. Data are presented as mean±s.d. *$p < 0.05$, **$p < 0.01$, ***$p < 0.001$). (E) Lung orthotopic tumor growth represented by luminescence intensity after PD-1, BMN/PAZA or BMN/PAZA+PD-1 combination treatment.

efficacy of BMN/PAZA+aPD-1 combination, we established an orthotopic lung cancer model by transplanting LLC-Luc into the lung of C57BL/6 mice. Compared to larger PVD nano-carrier, PAZA showed robust tumor targeting in lung orthotopic tumor (**Fig. 2-16B-D**). The control mice and PD1 treated group showed rapid cancer progression**,** which was reflected by *in vivo* imaging of LLC-Luc signal **(Fig. 2-16E)**. In comparison, the BMN/PAZA treated group showed stronger tumor growth inhibition effect. The BMN/PAZA + aPD-1 combination treated group showed repressed tumor growth and recession of tumor area after 2 weeks treatment, demonstrating the enhanced synergy in the overall antitumor activity in orthotopic lung tumor model.

2.4 Discussion

Suboptimal tumor targeting and penetration remain significant challenges in the clinical translation of nanomedicine. To address these challenges, two primary strategies have emerged. The first strategy is to design small-sized nanocarriers that can achieve better tumor targeting and penetration presumably through benefiting more from the leaky blood vessels and cellular gaps [131-133]. In addition, nanoparticles with a particle size below 20 nm haven been reported to be more advantageous in overcoming interstitial fluid pressure (IFP) and extracellular matrix (ECM), which is beneficial to achieve deep tissue penetration [134]. Another strategy is to incorporate a targeting ligand to improve specific tumor cell binding and enhance transcytosis through endothelial cells and tumor cells [135, 136]. However, while these strategies have been explored, the design of NPs often overlooks the influence of the protein corona on *in vivo* behaviors. PC was reported to mask intended targeting ligands of the nanocarriers, resulting in non-specific cellular interactions [137]. However, recent studies have shown that certain proteins within the corona,

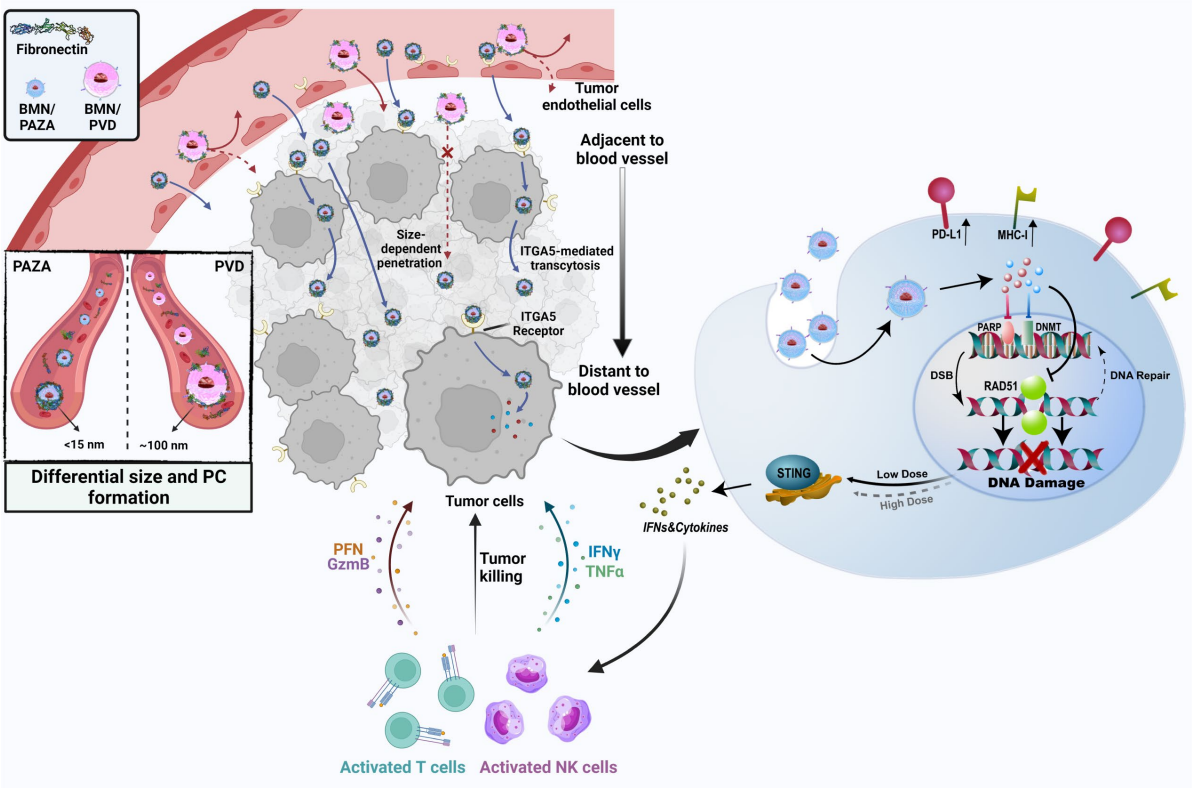

Figure 2-17. Schematic illustration of the formation of fibronectin-enriched PC on small-sized BMN/PAZA NPs, the tumor penetration through ITGA5-dependent transcytosis of small-sized BMN/PAZA NPs and the tumor inhibition via increased DNA damage and activation of immune response of BMN/PAZA combination.

Systemic administration of BMN/PAZA NP could recruit fibronectin on its surface as protein corona, followed by efficiently targeting and penetrating tumor deeply through ultra-small size effect and ITGA5- dependent transcytosis mechanism. Release of BMN-673 and 5-azacitidine inhibited the PARP and the DNMT respectively. The synergistic inhibition induced DNA repair dysfunction and DNA damage. Low dose combination treatment could further elicit the cGAS/STING based innate immune pathway. The epigenetic modulation of tumor cells and activated innate immune together contributed to the activation of T-cell and NK cell.

such as albumin, transferrin, and apolipoprotein, can potentiate the targeting and therapeutic capabilities of NPs [138-140]. This underscores the need to consider PC during the nanocarrier design and develop strategies that promote the adsorption of desirable proteins while minimizing the nonspecific adsorption of undesirable ones.

In our study, the conjugation of AZA to the PVD backbone drastically reduced particle size, which altered the PC composition on the NPs. Specifically, FN became more enriched in the corona of PAZA NPs. The FN interacts with the ITGA5 receptor on tumor cells, facilitating increased tumor cellular uptake and transcytosis of PAZA NPs, leading to enhanced tumor penetration (**Fig. 2-17**). This work represents the first to show that small, ligand-free NPs can gain tumor-targeting property following i.v. administration via recruiting tumor-homing protein FN. In addition to providing a simple and effective tumor-targeting system, this study may have a broad implication in understanding the interaction of NPs with biological system and the potential biological consequences.

In addition to excellent tumor targeting and penetration, PAZA nanocarrier shows excellent loading capacity for both hydrophilic AZA and hydrophobic PARPi BMN. Molecular dynamics and experimental validation reveal the mechanism behind the high drug loading capacity of the small nanocarrier, with the pyrimidine ring of AZA contributing significantly to BMN loading through π-π interactions. Moreover, the pharmacological combination of PAZA and BMN showed strong synergistic effect through the inhibition of DNA repair and the activation of both innate and adaptive immune responses. More importantly, BMN/PAZA formulation was more effective in tumor inhibition at lower dose due to the stronger immune activation, which denotes a wider therapeutic window with low toxicity (**Fig. 2-17**). Furthermore, BMN/PAZA increased the immunogenicity and potentiated the response to aPD-1 treatment, expanding the clinical application of aPD-1 in those tumors with poor immune checkpoint blockade response. All results together suggested an exciting possibility for expanding PARPi in HR-proficient NSCLC by our small PAZA nanocarrier.

This study demonstrated the enhanced EPR effect from our ultrasmall size nanoparticle PAZA. We further showed the FN enriched protein corona led to ITGA5-mediated transcytosis. However, PAZA is still limited to being studied as EPR based targeting. We acknowledge that ITGA5 on tumor endothelial cells shall likely contribute to the tumor targeting of PAZA NPs, which will be further studied in the near future. In fact, the transcytosis-based tumor targeting mechanism may represent a more effective strategy for designing the tumor-targeting NPs, which will be elaborated in section 3 with the example of CD44-mediated transcytosis.

3.0 Inhibition of iRhom by CD44-targeting Nanocarrier for Improved Cancer Immunochemotherapy

3.1 Introduction

Resistance to cancer therapy such as chemotherapy and immunotherapy remains a challenge in curing cancer patients. The improvement of treatment regimens, especially through rational design of combination therapy, has resulted in advancement in overcoming chemoresistance [141, 142]. The discovery of immune checkpoint molecules such as PD-1/PD-L1 and CTLA4 has also changed the landscape of cancer immunotherapy. However, only a small population of cancer patients benefit from immune checkpoint blockade (ICB)-based immunotherapy such as colorectal cancer (CRC) patients with deficient mismatch repair (dMMR) [143]. Strong interests remain in developing new mechanism-based therapies to benefit more cancer patients.

IRhom proteins (iRhom 1 and iRhom 2) are catalytically inactive relatives of rhomboid intramembrane proteases [144, 145]. They are widely distributed in many tissues and play an important role in regulating the stability and trafficking of other membrane proteins. IRhom proteins have seven transmembrane domains and are predominantly localized in endoplasmic reticulum (ER) [146] but also distributed on the route of protein trafficking, including Golgi and cell surface [147, 148]. They have been shown to regulate (enhance) the activity of ADAM17, a membrane-tethered metalloprotease and the primary shedding enzyme responsible for the release of the proinflammatory cytokine TNFα and several EGF receptor ligands [146, 149-152]. IRhom proteins are also found to be involved in regulating the homeostasis and functions of other proteins

such as HiF1α and JNK2/3 [147, 153, 154]. IRhom1 is overexpressed in breast cancer (BC) and head and neck cancer, and knockdown (KD) of iRhom1 causes apoptosis or autophagy in epithelial cancer cells, and attenuation of fibrotic stroma formation through inhibiting the endothelial–mesenchymal transition [154-156]. Moreover, a negative correlation between $CD8^+$ T cell infiltration and iRhom1 expression is shown in several types of cancers including BC and CRC [154]. Knockout (KO) of iRhom1 in 4T1 cells (murine BC cell line) is associated with delayed tumor growth and more infiltration of immune cells [154]. The potentially multifunctional role of iRhom in regulating both tumor survival and immune microenvironment suggests a novel and effective therapeutic target for improving cancer treatment. In this study, we investigated the mechanism of how iRhom1 regulates the antitumor immune response. The role of iRhom1 in chemosensitivity was also examined.

Finally, to enable a new immunochemotherapy based on nanoparticle (NP)-mediated co-delivery of iRhom1 pre-siRNA and a chemotherapeutic drug, a new polymeric nanocarrier PEG-Chitosan-Lipid (PCL) was developed. More importantly, we systematically characterized the CD44-mediated transcytosis and its role in tumor targeting and penetration of our nanocarrier. In this study, we demonstrated the vital role of transcytosis-based mechanism in our nanocarrier-based immunochemotherapy.

3.2 Material and Method

3.2.1 Clinical data analysis

GEPIA2 web tool was used for the analysis of iRhom1 expression in different cancer types and the correlation between iRhom1 expression and survival outcome [157].

For the analysis of specific chemotherapy cohort, we collected clinical information and the transcriptome data of 1174 patients of BC from TCGA-BRCA, and 515 CRC patients from the TCGA-COAD. Triple negative breast cancer patient cohort (BRCA-TNBC) was selected based on the IHC information of BC patients. The cohort of patients that received chemotherapy was identified based on the clinical information to generate BRCA-TNBC-chemotherapy cohort (n=85) and COAD-chemotherapy cohort (n=145) respectively. The analyses in this study were mostly restricted to primary tumor samples. The transcriptome data from GDC were annotated based on human reference genome GRCh38 and were quantified as the gene-level expression in FPKM. The cut-off of expression is 50 percent quantile.

For the analysis of the correlation of the expression levels of iRhom1 and APP-related molecules in human tumor tissues, a CPTAC dataset that contains mass spectrometry-based proteomics of 122 treatment-naive primary breast cancers was used and analyzed [158].

3.2.2 Clustering analysis of drug response

Drug response data of 545 agents tested across 722 cancer cell lines are downloaded from the CTRP [159, 160]. Two hundred and eighty-two (282) agents that showed sensitivity with low RHBDF1 expression were clustered based on their mechanism of action. Category of mechanism

of action was defined by the protein targets or activity of agents based on the Informer Set of CTRP [161]. One hundred and sixty-two (162) drug targets were clustered together with average correlation Z-score and total number of molecules in each cluster.

3.2.3 RNA-seq analysis

RNA seq of iRhom$^{-/-}$ CT26 cell sample and control sample was performed at the Health Sciences Sequencing Core at Children's Hospital of Pittsburgh. Raw sequence data was analyzed by HISAT-Stringtie workflow as described in previously published protocol [111, 112, 162] to generate transcript level gene expression. Then gene set enrichment analysis (GSEA) [163] was performed to identify the treatment-associated alteration in functional pathways.

3.2.4 Reagent

Dulbecco's Modified Eagle's Medium (DMEM), RPMI 1640 Medium, trypsin-EDTA solution, 3-(4,5dimethylthiazol-2-yl)-2,5-diphenyl tetrazolium bromide (MTT), triethylamine, D-Luciferin, doxorubicin, camptothecin, ivermectin and SAHA were purchased from Sigma-Aldrich (MO, U.S.A).

3.2.5 Cell lines and animals

CT26 and MC38 murine CRC cell lines, 4T1.2 murine BC cell line and MDA-MB-468 human BC cell line were obtained from ATCC (Manassas, VA). B16F10 and B16F10-OVA were

obtained from Dr. Da Yang's lab. They were cultured in DMEM medium supplemented with 10% FBS and 1% penicillin/streptomycin at 37 °C in a humidified atmosphere with 5% CO_2.

IRhom1$^{-/-}$ cell lines were generated by using CRISPR technology. Cells were infected with the lentivirus packaged by LentiCRISPR-sgRHBDF1 expression plasmid encoding puromycin resistance. The sgRNA sequences of RHBDF1 were previously described in GeCKO v2 Mouse CRISPR Knockout Pooled Library [164] for mRHBDF1. The successfully knocked out cells were selected by single clone culture followed by Western blot analysis for the lack of RHBDF1 proteins.

IRhom1 rescue cell lines and overexpression cell lines were generated by stable expression of pLenti-C-mGFP-P2A-rhbdf1-Puro plasmid. The successful knockout cells were selected by cell sorting of EGFP^{+} population. Cells were further confirmed by Western blot analysis for both GFP and iRhom1 expression.

CD44$^{-/-}$ cells were also generated by using CRISPR technology. Cells were infected with the lentivirus packaged by CD44-All-in-one lentiviral sgRNA-CRISPR-Cas9 plasmid encoding EGFP and puromycin resistance. The successfully knocked out cells were selected by cell sorting of EGFP^{+} and CD44$^{-/-}$ population. Cells were further confirmed by Western blot analysis for the lack of CD44 proteins.

Female Balb/c mice (4–6 weeks) were purchased from Charles River (CA, U.S.A). C57BL/6 mice, B6.129(Cg)-Cd44tm1Hbg/J (CD44$^{-/-}$) mice, C57BL/6-Tg(TcraTcrb)1100Mjb/J (OT-1) mice, Nu/J mice (4–6 weeks) were purchased from Jackson Lab (ME, U.S.A). All animals were housed under pathogen-free conditions according to AAALAC (Association for Assessment and Accreditation of Laboratory Animal Care) guidelines. All animal-related experiments were

performed in full compliance with institutional guidelines and approved by the Animal Use and Care Administrative Advisory Committee at the University of Pittsburgh.

3.2.6 Vector, RNA interference and lentiviral infection

RHBDF1 cDNA ORF Clone (Cat. MG5A2039-U) was obtained from Sino Biological (PA, U.S.A). Flag tagged MAPK14 Mouse ORF Clone (Cat.MR227429) was purchased from Origene (MD, USA). LentiCRISPR V2 Plasmid (#52961) was purchased from Addgene (MA, USA). CD44-All-in-one lentiviral sgRNA-CRISPR-Cas9 plasmid was purchased from Horizon Discovery Ltd. (Cambridge, UK). pLVX-HA-Hygro[165], psPAX2, pMD2.G were kindly provided by Dr. D. Yang (University of Pittsburgh). The LentiCRISPR-sgRHBDF1 was generated by following the published protocol [164]. The pLVX-HA-iRhom-Hygro was generated by the insertion of RHBDF1 cDNA ORF into pLVX-HA-Hygro vector. The ERAP1 siRNA (Cat. sc-44435) was purchased from Santa Cruz Biotechnology (TX. USA). pLenti-C-mGFP-P2A-rhbdf1-Puro (Cat. MR210964L4) and pLenti-C-mGFP-P2A-rhbdf1-Puro (Cat. MR210845L4V) plasmids for iRhom1/iRhom2 expression was purchased from Origene.

3.2.7 Preparation of rhomboid pre-siRNA

Production of Rhomboid pre-siRNA (pre-siiRhom) and control scaffold tRNA (LSA) was conducted as described before [166-168]. Briefly, HST08 bacterial cells were transformed with Bio-Rhomboid-siRNA plasmid or the tRNA-plasmid. Following the isolation of total RNA from bacteria, recombinant RNA was purified with an NGC Quest 10 Plus Chromatography system consisting of an ENrichTM Q 10×100 column (Bio-Rad, Hercules, CA). RNA concentration was

determined with a Nano-drop 2000 Spectrophotometer (Thermo Fisher Scientific), and RNA purity was examined by high-performance liquid chromatography as described before[169]. Endotoxin levels were determined by using Limulus Amebocyte Lysate Pyrogent-5000 kinetic assay (Lonza, Walkersville, MD), following the manufacturer's instructions.

3.2.8 Tumor models

Subcutaneous (s.c.) CRC tumor model was established by injecting CT26 (5×10^5 per mouse) cells into the abdomen of Balb/c mice. Orthotopic breast tumor model will be established by inoculating 4T1 cells ($1x10^5$ cells/mouse) into the mammary gland of a BALB/c or nude mouse. S.C. $CD44^{-/-}$ tumor model was established by injecting $CD44^{-/-}$ CT26 (5×10^5 per mouse) cells into the abdomen of Balb/c mice or $CD44^{-/-}$ MC38 (5×10^5 per mouse) cells into the abdomen of B6.129(Cg)-Cd44tm1Hbg/J (CD44-/-) mice. S.C. luciferase-expressing CRC model was established by injecting CT26-Luc (5×10^5 per mouse) cells into the right flank of Balb/c mice. The iRhom KO tumor model was established by inoculation more $iRhom1^{-/-}$ CT26 cells (5×10^6 per mouse) together with Matrigel into the abdomen of Balb/c mice.

3.2.9 Co-immunoprecipitation

Cellular lysates were prepared by incubating the cells in IP lysis buffer (Thermo Fisher Scientific) in the presence of protease inhibitor cocktail (Sigma-Aldrich) and phosphatase inhibitors (Thermo Fisher Scientific) for 20 min at 4°C with vortexing every 5 min, followed by centrifugation at 13,000 rpm for 10 min at 4°C. For immunoprecipitation, about 1 mg of protein was incubated with anti-HA magnetic beads (Thermo Fisher Scientific), Anti-DYKDDDDK

magnetic beads (Thermo Fisher Scientific) or Anti-GFP magnetic beads (ChromoTek). Protein was pulled down according to manufacturer's protocol. The precipitated proteins were eluted from the beads by resuspending the beads in 2.5× SDS-PAGE loading buffer and boiling for 10 min. The boiled immune complexes were subjected to SDS-PAGE, followed by immunoblotting with appropriate antibodies.

3.2.10 *In vitro* T cell killing assay

$CD8^+$ T cells were isolated from spleens of OT-1 TCR transgenic mice using a $CD8a^+$ T Cell Isolation Kit (Miltenyi Biotec) with a MidiMACS separator. Purified OT-1 T cells were then suspended in RPMI 1640 medium containing 10% FBS, anti-mouse CD3 (clone: 2C11, 4 μg/ml), and anti-mouse CD28 (clone: 37.51, 4 μg/ml). After 48 hours of stimulation, activated OT-1 T cells were seeded into a new plate with B16-OVA cells tumor cells at various E:T ratios in fresh medium for 24 h of further culture. Then cytotoxicity detection kit (Sigma-Aldrich) was used to measure the cytolysis rate elicited by $CD8^+$ T cells against different tumor cells based on producer's protocol. Under the same conditions, B16-OVA (WT or iRhom1-KO) cells were cocultured with $CD8^+$ T cells in sterile 12-well culture plates at 1:20 ratio for 18h, and images were taken under the phase contrast mode using a BZ-X710 Fluorescence Microscope (Keyence, Itasca, IL, USA).

3.2.11 Polymer synthesis and chemical characterization

Synthesis of CPT-SAHA: Camptothecin (1g, 2.87mmol) and 1,4,5-oxadithiepane-2,7-dione (2g, 12.33mmol) were dissolved in pyridine (30mL). The reaction was kept at 40°C for 48h. After the reaction, pyridine was removed by rotator evaporator. The residue was mixed with cold

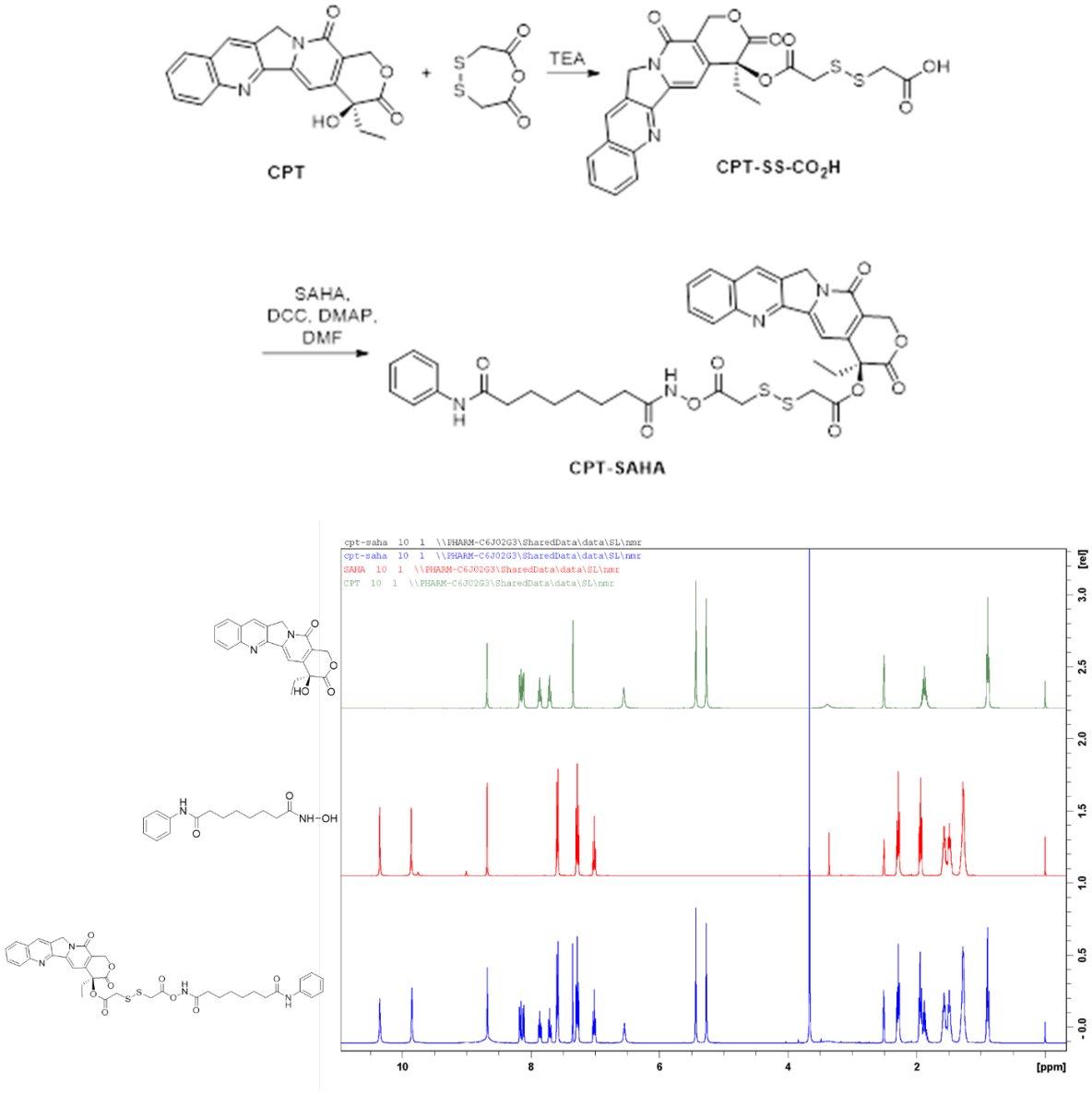

Figure 3-1. Synthesis route and 1H-NMR (in DMSO-d6) of CPT-SAHA. NMR of SAHA and campthothecin were used as reference.

ether to form precipitation. The precipitate was washed by HCl (1mol/L) to obtain CPT-SS-COOH (0.48g).

CPT-SS-COOH (0.51g, 1mmol), SAHA (0.26g 1mmol), DCC (0.41g, 2mmol), and DMAP (0.024g, 0.2mmol) were dissolved in DMF (20mL), and the reaction was kept at room temperature for 48h. After the reaction, the precipitates were removed by filtration. The filtrate was mixed with cold ether and the precipitate was collected and purified by silica gel column chromatography. The yield of CPT-SAHA was ~20% (0.146g). The structure was characterized by NMR (**Fig. 3-1**).

Synthesis of PEG-chitosan: Low molecule weight chitosan (340 mg, Sigma Aldrich, Cat. 448869) was dissolved in 5 mL DMF. PEG2K-NHS ester (420 mg, JenKem Technology, M-SCM-2000) and 1 mL triethylamine were added to the DMF mixture. The mixture was shaken at room temperature for 48 h. After the reaction, all the solution was transferred into a dialysis bag (MWCO: 12k-14k) and dialyzed against water. After 1 day dialysis, the solution was lyophilized to generate PEG-Chitosan.

Synthesis of 2-stearoylcyclohexane-1,3-dione (Ketone lipid): The synthesis was performed following a previously published route[170]. Dimedone (1.05 mol), stearic acid (1 mol), and DMAP (1.5 mol) were dissolved in dichloromethane ([dimedone] = 1.0 M). A separate solution of DCC (1.2 mol) in dichloromethane ([DCC] = 1.0 M) was added slowly at room temperature to the reaction mixture. The reaction mixture was shaken at room temperature for 4 h. Then, the white N, N'-dicyclohexylurea precipitate was filtered off and washed with dichloromethane until colorless. The dichloromethane filtrate was combined and washed with 3% HCl until the pH of the aqueous phase was < 3. The organic phase was separated, dried over Na_2SO_4, filtered and the solvent was removed under vacuum. The crude, pale yellow solid was

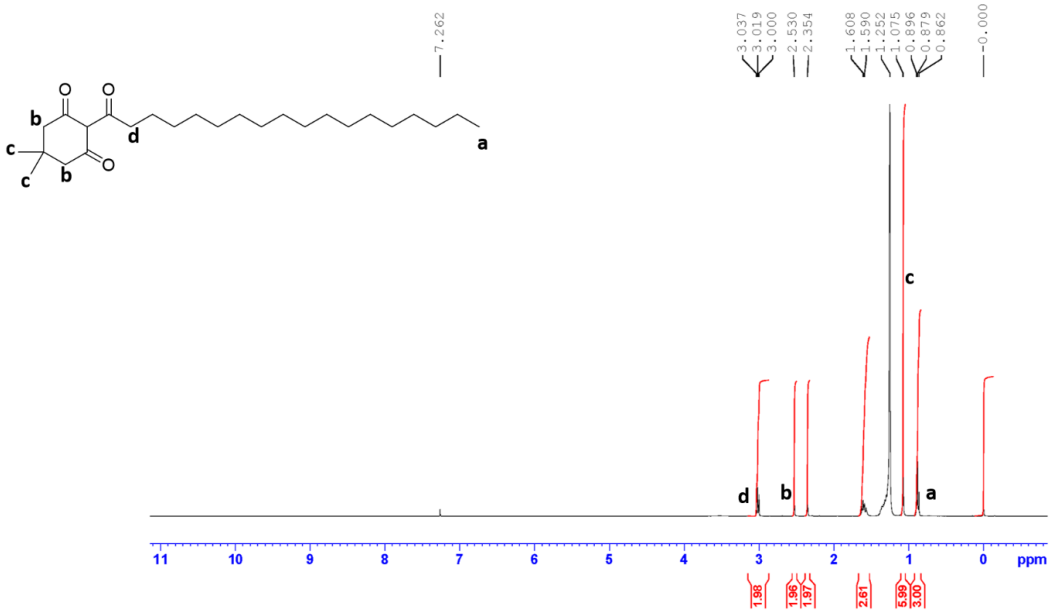

Figure 3-2. ^{1}H-NMR (in $CDCl_3$-*d*) of 2-stearoylcyclohexane-1,3-dione.

Each peak with label represents the feature structure.

recrystallized from EtOAc/Hex to yield colorless crystals. The structure was characterized by NMR (**Fig. 3-2**).

Synthesis of PEG-chitosan-lipid (Schiff link): PEG-chitosan (370 mg) was dissolved in 5 mL DMF followed by addition of 162 mg of 2-stearoylcyclohexane-1,3-dione (Schiff lipid). The mixture was shaken at room temperature overnight. Cold ether was then added to the reaction

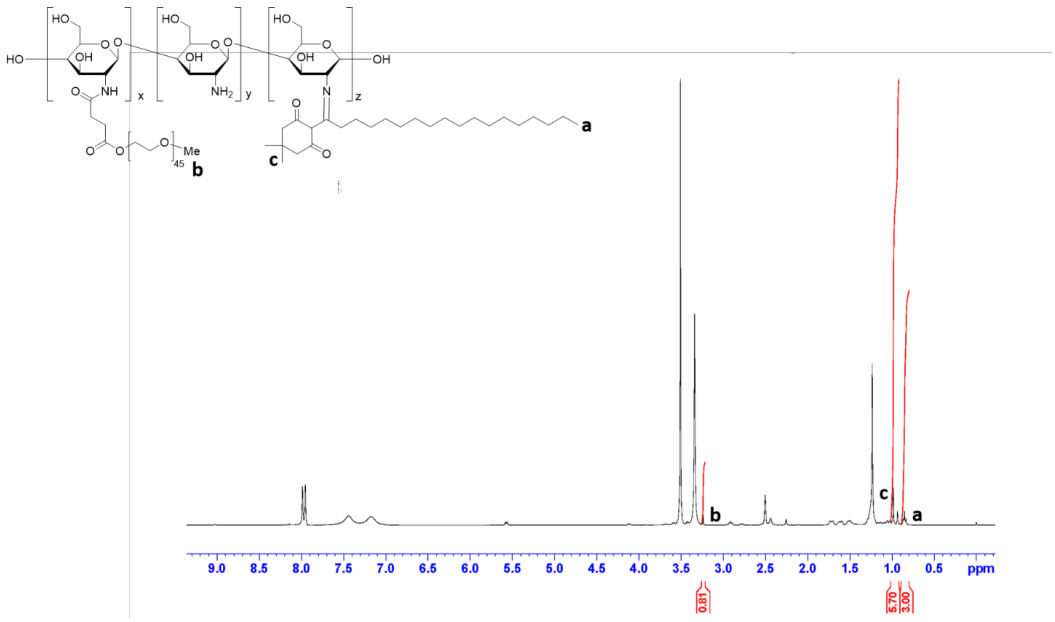

Figure 3-3. ^{1}H-NMR (in DMSO-*d*6) of PEG-Chitosan-lipid (PCL) with Schiff base linker.

Each peak with label represents the feature structure of the PCL polymer. PEG: lipid=1:4, calculated based on the integration ratio between peak a and peak b.

mixture. The precipitates were washed with cold ether 3 times. The solid was collected and dried under vacuum. The structure was characterized by NMR. The final polymer has ~9.5 PEG units, ~35 lipid units per 100 units of chitosan **(Fig. 3-3**).

Synthesis of PEG-chitosan-lipid (amide link): PEG-chitosan (370 mg) was dissolved in 5 mL DMF, followed by addition of 120 mg stearoyl chloride (Sigma-Aldrich) and 0.5 mL TEA. The mixture was shaken at room temperature overnight. Cold ether was then added to the reaction mixture. The precipitates were washed with cold ether 3 times. The solid was collected and dried

under vacuum. The structure was characterized by NMR. The final polymer has ~9.5 PEG units, ~38 lipid units per 100 units of chitosan **(Fig. 3-4)**.

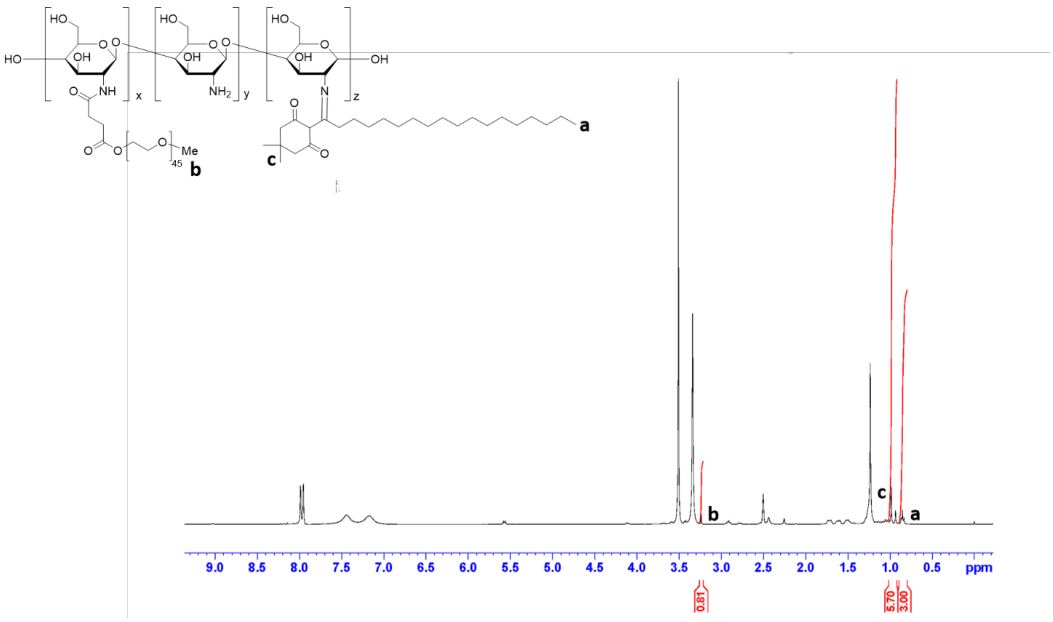

Figure 3-4. ^{1}H-NMR (in DMSO-*d*6) of PEG-Chitosan-lipid (PCL) with amide linker.

Each peak with label represents the feature structure of the PCL polymer. PEG: lipid=1:4, calculated based on the integration ratio between peak a and peak b.

3.2.12 Preparation and characterization of drug-loaded micelles

Blank micelles, drug (DOX or CPT-SAHA)-loaded micelles or drug/pre-siiRhom co-loaded micelles were prepared via a dialysis method. Briefly, drug solution (10 mg/mL in DMSO) was mixed with PCL polymer (5 mg/mL in DMSO) at various carrier/drug weight ratios. The mixture was transferred to a dialysis bag (MWCO:3000) and dialyzed against nano water overnight to generate the drug-loaded micelles. The micelles were concentrated by centrifugation using Vivaspin® tube (MWCO:3000) (Sartorious, Germany). Pre-siiRhom diluted with nano water was then mixed with drug-loaded micelles to form PCL/drug/pre-siiRhom complexes. Pre-siiRhom

complexation was examined by gel retardation. Subsequent incubation with CS/CS-PEG of various ratios led to the formation of CS/CS-PEG-decorated, drug/pre-siiRhom co-loaded PCL-CP NPs. The amounts of DOX or CPT-SAHA was measured by fluorometer and the amounts of pre-siiRhom was measured by Qubit 4 fluorometer (Thermo Fisher Scientific) according to manufacturer's protocol. Particle sizes and polydispersity were measured by DLS (Nano-ZS 90, Malvern Instruments, Malvern) and the morphology was examined by cryo-electron microscopy (cryo-EM).

3.2.13 CryoEM Methods

Samples were first checked with negative-stain electron microscopy by applying 3μL to a freshly glow-discharged continuous carbon on a copper grid and staining with a 1% uranyl acetate solution. Grids were inserted into a Tecnai TF20 electron microscope (Thermofisher Scientific, Waltham, Massachusetts, USA) equipped with a field emission gun and imaged on an XF416 CMOS camera (TVIPS GmbH, Gilching, Germany) to visualize nanoparticle uniformity and concentration. Cryo-grids were prepared by pipetting 3μL of sample on a Protochips C-flat CF-2/1-3CU-T grid (Protochips, Morrisville, North Carolina, USA) that had been glow discharged at 25 mA for 30 secs using an Emitech KX100 glow discharger. Grids were mounted in a Thermofisher Vitrobot Mk 4 with relative humidity of 95%, blotted for 3 secs with a force setting of 4, and plunged into a 40/60 mixture of liquid ethane/propane[171] that was cooled by a bath of liquid nitrogen. Grids were transferred onto a Gatan 910 3-grid cryoholder (Gatan, Inc, Pleasanton, California, USA) and into the TF20 microscope maintaining a temperature no higher than -175 °C throughout. The microscope was operated at 200 kV and contrast was enhanced with a 100μm objective aperture. Cryo-electron micrographs were collected at a nominal 150,000x magnification

on the TVIPS XF416 CMOS camera with a pixel size of 0.74 Ångstroms at the sample. Low dose methods were used to avoid electron beam damage and images were acquired with TVIPS EMplified software using movie mode for drift correction.

3.2.14 Measurement of critical micelle concentration (CMC)

The CMC of PCL-CP/DOX/pre-siRNA was determined via a DLS-based method [172]. Briefly, the light scattering intensity of the DOX/pre-siiRhom/PCL-CP micelles was measured at various concentrations (1–1,000.0 μg/mL) prepared in deionized water by serial dilution at 25 °C. By plotting the light scattering intensity against the DOX/pre-siiRhom/PCL-CP concentration, the CMC was determined as the intersection of the best fit lines drawn through the data points.

3.2.15 Drug release kinetics

The in vitro drug release from drug/pre-siiRhom-coloaded PCL-CP NPs was conducted by dialysis method. Briefly, 1 mL of PCL-CP NPs containing 0.2 mg of DOX or CPT-SAHA in PBS buffer or serum were placed in a clamped dialysis bag and immersed in 25 mL of 0.1 M PBS solution containing 0.5% (w/v) Tween 80. The experiment was performed in triplicate in an incubation shaker at 37 ℃ with gentle shaking (100 rpm). At selected time intervals, 10 μL of PCL-CP/drug/pre-siiRhom solution in the dialysis bag and 5 mL medium outside the dialysis bag were collected while same amount of fresh medium was added for replenishment. The DOX or CPT-SAHA concentration was determined by fluorometer.

3.2.16 Chitosanase-mediated degradation of PCL micelles

PCL (Schiff or amide link) micelles in 40 mM sodium acetate (pH=6) were prepared via dialysis method. Chitosanase (1 mg/mL, Sigma-Aldrich, Cat. 220477) was then added into the micelle solution to a final concentration of 2 μM. The mixture was incubated at 37 °C with gentle shaking. The size and count number were examined by DLS at different times following the incubation.

3.2.17 *In vitro* cytotoxicity assay

Cytotoxicity was performed by MTT assay on 4T1 (murine triple negative breast cancer cell line), MDA-MB-468 (human triple negative breast cancer cell line), CT-26 (murine colorectal cancer cell line), and HCT116 (human colorectal cancer cell line). Cells received various treatments including pre-siiRhom alone, DOX or CPT-SAHA alone, or drug and pre-siiRhom combination at various drug and siRNA concentrations for 48 h. For combination treatment, cells were transfected with pre-siRNA using Lipofectamine 3000 (Invitrogen) for 24 h followed by drug treatment for another 48 h. MTT assay was then performed following a published protocol[173]. IC_{50} was calculated through the Quest Graph™ IC50 Calculator [174]. Synergy was calculated through the SynergyFinder [175].

3.2.18 Pharmacokinetics and in vivo biodistribution

The plasma PK profiles of both DOX and pre-siiRhom after treatment with PCL-CP/DOX/pre-siiRhom were determined by HPLC-FLR and RT-PCR respectively. Groups of 3

female Balb/c mice bearing 4T1 orthotopic breast tumors (~400 mm^3) received tail vein injections of free DOX.HCl, free pre- siiRhom or PCL-CP/DOX/pre-siiRhom at a DOX dose of 5 mg/kg and a pre-siiRhom dose of 1.5 mg/kg, respectively. Blood samples were collected into tubes containing ETDA at designated time points (5min, 30 min, 1 h, 4 h and 24 h post injection). The samples were centrifuged at 12,500 rpm for 10 min at 4 °C and 200 μL of plasma was collected. For DOX measurement, 100 μL plasma was mixed with 50 μL daunorubicin (1 μg/mL, internal control) methanol solution, 250 μL 12 mM phosphoric acid and additional 600 μL methanol, and the mixture was vortexed for 5 min. The samples were centrifuged at 12,500 rpm for 10 min at 4 °C and 500 μL of the clear supernatant was collected and injected into HPLC for DOX measurement using a fluorescence detector. The elution condition of DOX is 0.1% TFA: methanol: acetonitrile (50:25:25) with the excitation at 480nm and emission at 580nm.

For pre-siiRhom measurement, RNA was purified from 30 μL plasma using miRNeasy Serum/Plasma kit (Qiagen, MD, U.S.A). The pre-siiRhom was measured by qRT-PCR as previously published[176]. A standard curve was generated by spiking known amounts of pre-siiRhom followed by purification and qRT-PCR amplification as described above. The copy number of pre-siiRhom in each sample was determined by applying the Ct value to the standard curve. Noncompartmental pharmacokinetic analysis was executed by PK R package[177].

For biodistribution study, tumor-bearing mice received free DOX.HCl, pre-siiRhom alone or PCL-CP/DOX/pre-siiRhom as described above. Tumors and major organs (heart, liver, spleen, lung and kidney) were collected at designated time points (5min, 30 min, 1 h, 4 h and 24 h post injection). Tumors and organs were weighted and PBS was added at 5mL per gram tissue. Tissues were homogenized in PBS buffer. For DOX measurement, 100 μL of homogenized tissue were mixed with 50 μL daunorubicin methanol solution (1 μg/mL), 250 μL 12 mM phosphoric acid and

additional 600 μL methanol. The mixture was vortexed for 5 min. The samples were centrifuged at 12,500 rpm for 10 min at 4 °C and 500 μL of the clear supernatant was collected and injected into HPLC for DOX analysis as described above. For pre-siiRhom measurement, RNA was first extracted from 200 μL of homogenized tissue using Trizol reagent (Invitrogen, NY, U.S.A) following the protocol of the manufacturer. The RNA was further purified with PureLink™ miRNA Isolation Kit (Invitrogen, NY, U.S.A). Then pre-siiRhom was similarly determined as described above.

3.2.19 Cellular uptake

For cellular uptake study, WT or $CD44^{-/-}$ cells were incubated with Cy5.5 labeled PCL-CP NPs, respectively, for 6 h. Then, the culture medium was discarded, and cells were washed with cold saline 3 times and analyzed by flow cytometry.

3.2.20 *In vitro* transwell assay

For all transwell-based transcytosis assays, 0.4 μm pore size filter transwell inserts (Corning, product no. 3470) were used in 6 well plates. An *in vitro* multilayer cell model was established by seeding the cells onto the apical side of a transwell insert. Growth media volumes were calculated to be 500 μl and 2000 μl for apical and basolateral chambers respectively. Seeded cells were cultured for 3 days to form cell layers[105]. The lower chamber was then added with blank DMEM medium, and the upper chamber was added with DMEM medium containing Cy5.5-labeled PCL, PCL/CS or PCL-CP NPs (500μg/mL), with or without pre-treatment with

transcytosis inhibitor chlorpromazine (6 μg/ml) for 2 h. At 8 h after addition of NPs, the fluorescence intensity of the medium in the lower chamber was determined.

In a separate study, HUVEC cells were seeded onto the 0.4 μm diameter microporous membrane of a cell culture insert, followed by incubation in growth factor-containing ECM medium for 2 days to cover the membrane surface. The lower chamber was added with ECM medium, and the upper chamber was added with ECM medium containing Cy5.5-labeled PCL, PCL/CS or PCL-CP NPs (500μg/mL), with or without pre-treatment with transcytosis inhibitor chlorpromazine (6 μg/ml) for 2 h. At 8 h after addition of NPs, the fluorescence intensity of the medium in the lower chamber was determined.

3.2.21 Cell spheroid penetration

WT or $CD44^{-/-}$ CT26 (4T1) cells were seeded in a Nunclon Sphera 96 well U-bottom plate (Thermo Fisher) at a density of 10000 cells per well with 6 μg/ml of collagen I to form a single spheroid per well [106]. After 96 h incubation, dense spheroids were formed, which were confirmed by microscopic examination. The cell spheroids were then incubated with Cy5.5-labeled PCL, PCL/CS or PCL-CP NPs, with or without pre-treatment with chlorpromazine (6 μg/ml) for 2 h. After 18 h incubation with NPs, the spheroids were gently rinsed by saline 3 times. The penetration ability was observed by a confocal laser scanning microscope with Z stack scanning (CLSM, FluoView 3000, Olympus) at 30 μm intervals from the bottom to the middle of the spheroids.

3.2.22 NPs accumulation and penetration in the tumor tissues

The tumor targeting effect of PCL-CP NPs was evaluated in both WT/CD44$^{-/-}$ CT26 tumors (s.c.) established in Balb/c mice and WT/CD44$^{-/-}$MC38 tumors (s.c.) established in B6.129(Cg)-Cd44tm1Hbg/J (CD44$^{-/-}$) mice. Hydrophobic fluorescence dye DiR was loaded into the Cy5.5-labeled PCL-CP carrier at a wt./wt. ratio of 20:1 and intravenously injected into the mice for real-time imaging at the DiR dosage of 0.5 mg/kg. After 24 h, the mice were imaged by an IVIS 200 system with excitation at 730 nm and ICG filter to detect the DiR signal, and excitation at 640 nm and Cy5.5 filter to detect the Cy5.5 signal. The tumor and various organs were then excised for *ex vivo* imaging following our previous protocol [102]. The tumor was then frozen sectioned, and stained with DAPI to label the cell nucleus and the antibody for CD31 to label the vascular endothelial cell. The fluorescence signals in the tumor sections were examined under Keyence BZ-X800 fluorescence microscope.

3.2.23 *In vivo* gene knockdown

Luciferase pre-siRNA- (pre-siLuc) or pre-siCT-loaded PCL-CP NPs were intravenously injected into CT26-Luc tumor-bearing mice at a dose of 1.5 mg pre-siRNA/kg. The efficiency of gene knockdown was measured three times by whole body bioluminescence imaging on the 2nd day following the 1st, 2nd, and 3rd injection of the NPs once every 3 days, respectively. The exposure time was set at 60s for every experiment. Mice were anesthetized according to protocol prior to imaging.

3.2.24 Therapeutic treatment

Therapeutic efficacy was evaluated in both murine breast and colon cancer models. Treatments were started when the tumor reached about 50 mm^3. For colorectal tumor model, groups of 5 mice were treated with saline, PCL-CP/pre-siCT, PCL-CP/pre-siiRhom, PCL-CP/CPT-SAHA and PCL-CP/CPT-SAHA/pre-siiRhom respectively. The dose of CPT-SAHA was 20 mg/kg, and the dose of pre-siRNA was 1.5 mg/kg. For breast tumor model, groups of 5 mice were treated with saline, PCL-CP/pre-siCT, PCL-CP/pre-siiRhom, PCL-CP/DOX and PCL-CP/DOX/pre-siiRhom respectively. The dose of DOX was 5 mg/kg and the dose of pre-siRNA was 1.5 mg/kg. Treatments were given once every 3 days for 5 times by tail vein injection. Tumor volumes were monitored and calculated according to the formula: $(L*W^2)/2$ (L and W are the long and short diameters). Body weights were also followed throughout the entire treatment period. After completing the in vivo experiment, tumor tissues were collected, fixed in 10% formaldehyde, and then embedded in paraffin. The paraffin-embedded tumor tissues were sectioned into slices at 4 μm using an HM 325 Rotary Microtome for further immunohistochemistry staining.

Survival study with aPD-1 combination was conducted with CT26 tumor model. When the tumor volume reached about 200 mm^3, mice were randomly grouped (n=8) and treated with saline, aPD-1, PCL-CP/CPT-SAHA/pre-siiRhom, aPD-1+PCL-CP/CPT-SAHA/pre-siiRhom. Mice were followed for about 4 months for survival.

3.2.25 Immunohistochemistry

For immunostaining, the tumor tissue sections were deparaffinized in xylene and hydrated in descending grades of ethyl alcohol. Sections were unmasked with a boiling 0.1 M sodium citrate

buffer and incubated with 0.3% (v/v) hydrogen peroxide to inactivate endogenous peroxidase activity. Then, the sections were washed twice in distilled water and incubated with diluted normal blocking serum for 1 h. After that, the sections were incubated with primary antibody diluted in blocking buffer at 4 ˚C overnight and washed with TBST for 3 times prior to incubation with secondary antibody. Then the sections were washed with TBST and treated with Vectastain Elite ABC reagent. The sections were incubated with DAB substrate at room temperature for 15 s. Finally, counterstaining was conducted with hematoxylin for imaging under a BZ-X710 Fluorescence Microscope (Keyence, Itasca, IL, USA).

3.2.26 Toxicity

Blood samples were collected after therapeutic study. Complete blood count (CBC) was performed via HemaVet 950FS Auto Blood Analyzer. In addition, serum samples were prepared and the serum levels of alanine aminotransferase (ALT), aspartate aminotransferase (AST) and creatinine were evaluated following manufacturer's protocols as indicators of hepatic and renal function.

Tissues were also processed for H&E staining to test if there is histology change following various treatments [108].

3.2.27 Analysis of tumor-infiltrating immune cells

The immune cell populations in tumors after various treatments were measured by flow cytometry following previous protocol [110]. Briefly, one day after the last treatment, cell suspensions from the spleens or tumors were prepared, and red blood cells lysed. Single cell

suspensions were incubated with respective antibodies. Zombie dye was used to discriminate viable and dead cells. Infiltration of various immune cells ($CD4^+$, $CD8^+$, Treg) in tumor tissues, the production of lymphocyte effector molecules (such as IFN-γ and granzyme B) in immune cells, and the surface levels of MHC-I on tumor cells were determined by multi-color flow cytometric analysis.

3.2.28 Statistical analysis

All values were presented as mean ± s.e.m. Statistical analysis was performed with two-tailed Student's t-test for comparison between two groups, one-way analysis of variance (ANOVA) with Tukey's post hoc test for comparison between multiple groups, and log-rank (Mantel-Cox) test for survival analysis. Results were considered statistically significant if $P < 0.05$. Prism 9.4.0 (GraphPad Software) was used for data analysis and graph plotting.

3.3 Result

3.3.1 Role of iRhom1 in regulating sensitivity to chemotherapy

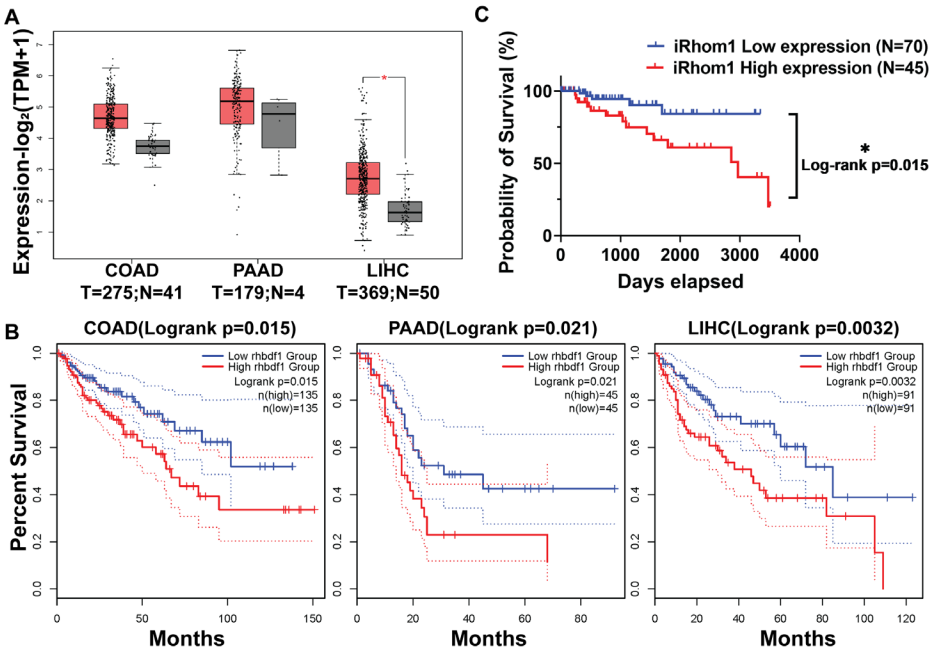

Figure 3-5. Analysis of TCGA data by GEPIA online tool.

(A) iRhom1 is overexpressed in several types of cancers. (B) High expression levels of iRhom1 are associated with poorer clinical prognosis. COAD: colon adenocarcinoma; PAAD: pancreatic adenocarcinoma; LIHC: liver hepatocellular carcinoma. (C) High expression levels of iRhom1 are associated with poorer clinical prognosis in triple negative breast cancer cohort.

IRhom1 has previously been shown to be overexpressed in breast and cervical cancers and its expression is negatively correlated with patient prognosis [153, 178]. Our analysis of the TCGA data shows that iRhom1 is also significantly upregulated in several other types of cancer including CRC, pancreatic cancer, and liver cancer **(Fig. 3-5A)**. The levels of iRhom1 expression are also negatively correlated with the clinical prognosis of those cancer patients (**Fig. 3-5B**). The same negative correlation occurs in triple negative breast cancer (TNBC) patients (**Fig. 3-5C**). More importantly, iRhom1 shows negative correlation with prognosis in those patient cohorts with

chemotherapy treatment in both TNBC and CRC (**Fig. 3-6A**), suggesting a likely role of iRhom1 in chemosensitivity.

As an initial step to understand the role of iRhom1 in regulating drug sensitivity, we analyzed the data in the Cancer Therapeutics Response Portal (CTRP) [161], a database of large-scale cancer cell line drug screening that correlates genetic biomarkers with the response to over 300 anti-cancer agents. Those agents are categorized by their mechanisms of action (protein target or activity) based on the Informer Set of CTRP [161]. This analysis shows that histone deacetylases (HDAC), microtube assembly, and topoisomerase inhibitors are the top ranked drugs whose sensitivity is likely to be regulated by iRhom1 (**Fig. 3-6B**). Therefore doxorubicin (DOX) and Vorinostat (SAHA)/camptothecin (CPT) were chosen as model drugs to test drug sensitivity as they are currently used in the treatment of BC and CRC, respectively. We also prepared a prodrug conjugate (CPT-SAHA) of CPT and SAHA to synergistically improve the anti-tumor activity [179] and to facilitate the incorporation of both drugs into a nanocarrier as detailed later. Indeed, cytotoxicity assays showed that iRhom1 siRNA KD led to sensitization of BC or CRC cells to

DOX or CPT-SAHA (**Fig. 3-6C**). Interestingly, treatment of 4T1 or CT26 cells with DOX or CPT-SAHA also led to increased expression of iRhom1 in a dose-dependent manner (**Fig. 3-6D**). These data suggest a role of iRhom1 in both intrinsic and possibly acquired drug resistance.

To gain more insights into the role of iRhom1 in oncogenesis and drug response, we generated CT26 and 4T1.2 iRhom1 KO sublines, respectively by using CRISPR-Cas9 technology. **Fig. 3-7A** shows the changes in several cancer hallmark signaling pathways from bulk RNAseq

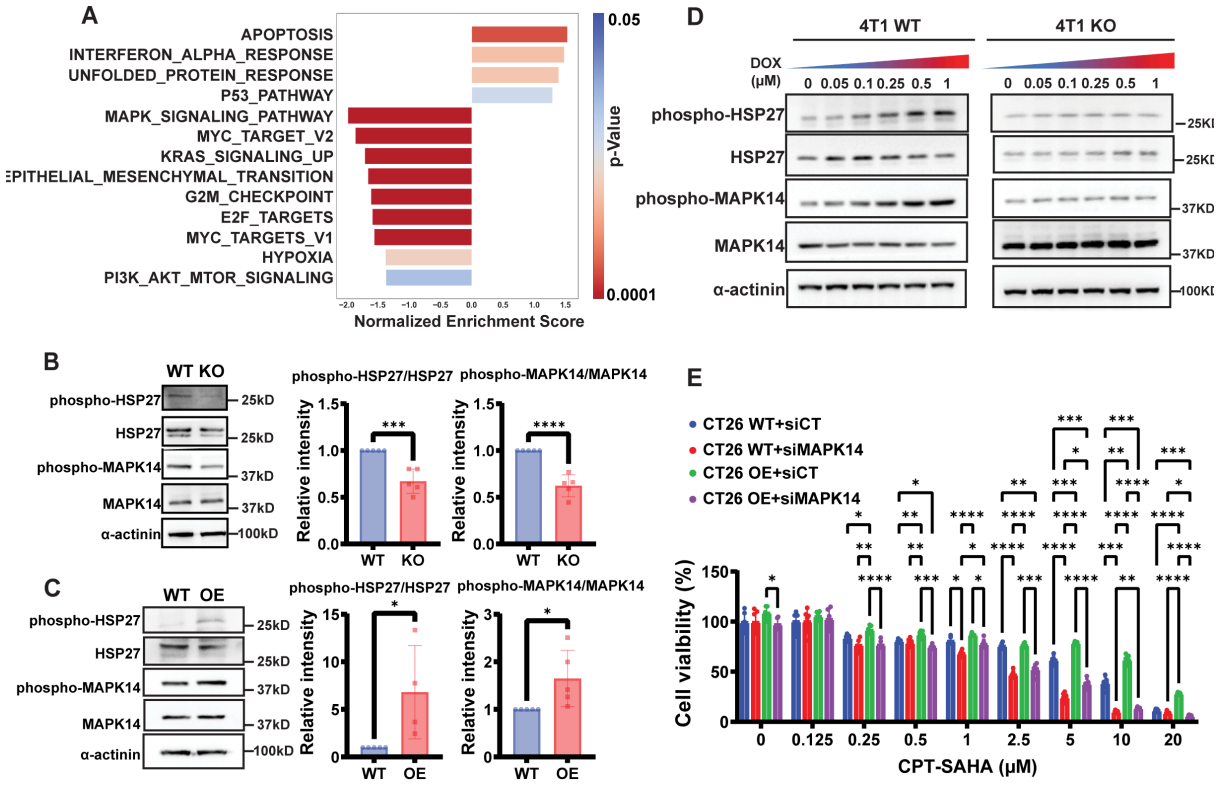

Figure 3-7. iRhom1 cause chemotherapy resistance through MAPK14-HSP27 axis.

(A) RNA-seq analysis of gene enrichment in various signaling pathways in iRhom1 KO CT26 cells compared to WT cells. (B) Changes in the protein levels of MAPK14-HSP27 axis in iRhom1 KO cells compared to WT cells. The experiment was repeated 5 times and data were quantified by densitometry. (C) Changes in the protein levels of MAPK14-HSP27 axis in iRhom1 OE cells compared to WT cells. The experiment was repeated 5 times and data were quantified by densitometry. (D) Changes in the protein levels of MAPK14-HSP27 axis after treatment with various concentrations of DOX in iRhom1 KO cells and WT cells. (E) MTT cytotoxicity assay of treatments with various concentrations of CPT-SAHA in CT26 WT or CT26 iRhom1 OE cells, with or without knockdown of MAPK14 respectively. N=6. The data are presented as the mean ± sem. *p < 0.05, **p < 0.01, ***p < 0.001.

data following KO of iRhom1 in CT26 cells. A number of signaling pathways were downregulated including MAPK, Myc, Kras, and hypoxia while the apoptosis pathway was upregulated. This result is consistent with the notion that iRhom1 supports the survival and proliferation of cancer cells. Furthermore, iRhom1 KO led to decreased expression of phosphorylated MAPK14 (p-MAPK14) and significantly reduced phosphorylation of HSP27 (p-HSP27) (**Fig. 3-7B**), one of the MAPK14 (also called p38-α) substrates and a known player that causes chemoresistance [180, 181]. In contrast, overexpression (OE) of iRhom1 in CT26 cells led to increased levels of p-MAPK14 and p-HSP27 (**Fig. 3-7C**). We have further shown that treatment with DOX led to increased expression of p-HSP27 and p-MAPK14 in WT cells but not in iRhom1 KO cells (**Fig. 3-7D**). **Fig. 3-7E** shows that iRhom1 OE in WT CT26 cells led to further increase in

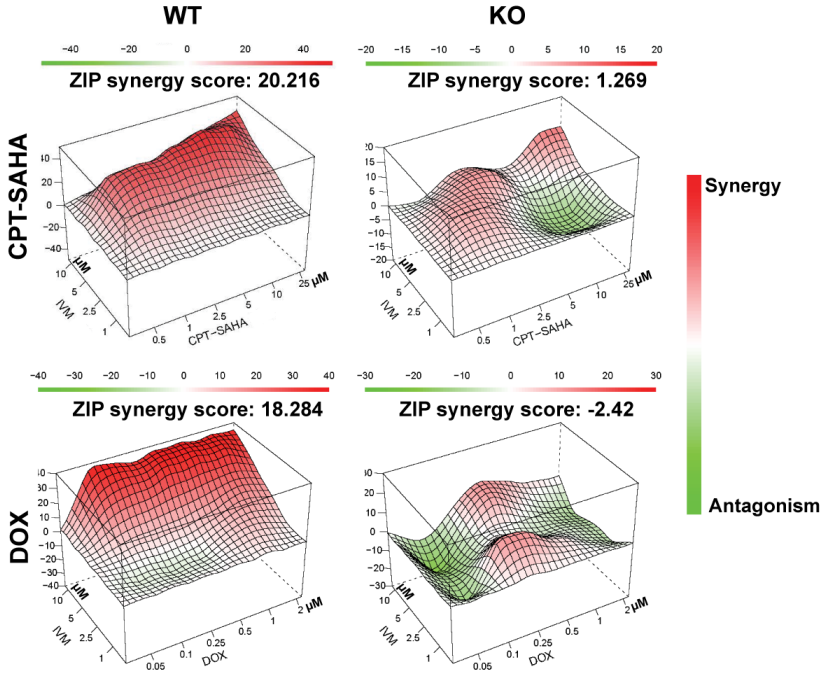

Figure 3-8. iRhom1 mediates the synergy between chemotherapy and HSP27 inhibition.

Synergy between Ivermectin (IVM) and chemotherapy drug (CPT-SAHA or DOX). Calculation of synergy is based on MTT cytotoxicity assay with various concentrations of Ivermectin along with various concentrations of CPT-SAHA or DOX in WT cells and iRhom1 KO cells. N=5.

chemoresistance but this effect was significantly abolished by MAPK14 KD. **Fig. 3-8** shows that

inhibition of phosphorylation of HSP27 by Ivermectin (IVM) treatment led to an overall significant synergistic effect with a chemotherapeutic agent in iRhom1 WT 4T1 and CT26 cells. However, this synergistic effect was significantly attenuated in iRhom1 KO cell lines, suggesting that MAPK14-HSP27 axis likely plays a role in iRhom1-mediated drug resistance.

Searching of iRhom1-interactive partners in proteomic database [182, 183] identified MAPK14 as one potential candidate that is regulated by iRhom1 through protein-protein interaction (PPI). The interaction of iRhom1 with MAPK14 or p-MAPK14 was further confirmed in a pull-down assay (**Fig. 3-9A**). MKK3/6 is an upstream kinase to phosphorylate MAPK14.

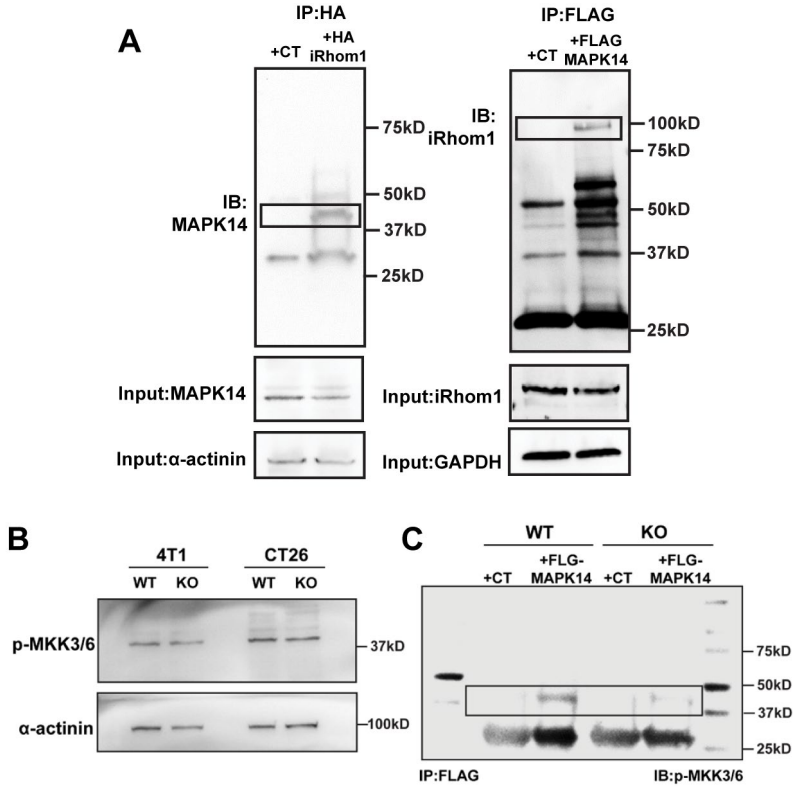

Figure 3-9. iRhom1 regulate MAPK14-HSP27 through protein-protein interaction.

(A) Immunoprecipitation of HA-iRhom1 with anti-HA beads led to pulldown of p-38α in 293T cells transfected with a HA-iRhom1 expression plasmid and reciprocal immunoprecipitation of FLAG-MAPK14 with anti-FLAG beads led to pulldown of iRhom1 in 293T cells transfected with a FLAG-MAPK14 expression plasmid. (B) IRhom1 KO shows no impact on the protein levels of p-MKK3/6 in 4T1 or CT26 cells. (C) Immunoprecipitation of FLAG-MAPK14 with anti-FLAG antibody failed to pulldown p-MKK3/6 in iRhom1 WT or KO cells transfected with a FLAG-MAPK14 expression plasmid.

IRhom1 KO did not affect the phosphorylation of MKK3/6 (**Fig. 3-9B**). However, the interaction between pMKK3/6 and MAPK14 was disrupted in iRhom1 KO cells, suggesting that iRhom1 serves as a scaffold for MAPK14 phosphorylation (**Fig. 3-9C**). MAPK14/HSP27 axis is implicated in both oncogenesis and chemoresistance [184, 185]. Our data suggest that iRhom1 inhibits the drug response likely through regulating the iRhom1/MAPK14/HSP27 pathway.

3.3.2 Role of iRhom1 in regulating immune response

As an initial step to gain insights into the role of iRhom1 in modulating immune responses, we examined the *in vivo* tumor growth rate of iRhom1 WT vs KO tumor cells. Consistent with slower proliferation in culture, iRhom 1 KO CT26 cells formed smaller tumors compared to WT cells in immunodeficient mice (**Fig. 3-10A**). Interestingly, tumor formation was completely

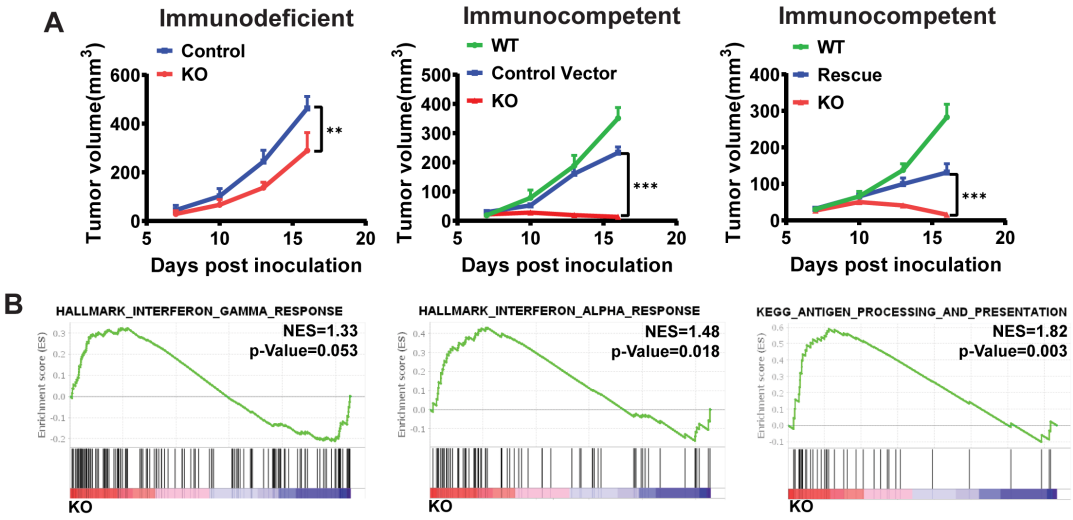

Figure 3-10. iRhom1 is involved in cancer immunity.

(A) Tumor growth curves of WT, iRhom1 KO, iRhom1 rescue and vector control CT26 cells in immunodeficient or immunocompetent mice. N = 3. Data are presented as mean ± s.e.m. *p < 0.05, **p < 0.01, ***p < 0.001. (B) Activation of immune-related signaling pathways in iRhom1-/- CT26 cells (RNAseq analysis).

abolished in immunocompetent mice inoculated with iRhom1 KO CT26 cells (**Fig. 3-10A**). Re-expression of iRhom1 in iRhom1 KO cells led to regained tumor growth *in vivo* (**Fig. 3-10A**). The incomplete rescue of tumor growth in iRhom1-reexpressed cells is likely attributed to the increased immunogenicity of CRISPR-engineered cells that involved the use of a lentiviral vector [186-188]. The above data suggest that the immunomodulating effect of iRhom1 likely plays a more important role in controlling tumor growth *in vivo*. This is supported by RNAseq data showing upregulation of several immune pathways including enhanced interferon response and enhanced antigen presentation in the KO cells (**Fig. 3-10B**).

To gain the mechanistic insights, we examined the impact of iRhom1 KO on antigen (Ag) presentation. B16-OVA cells express chicken OVA as surrogate tumor Ag (e.g., OVA-derived peptide SIINFEKL bound to MHC class I H-2Kb) and have been widely used to study Ag

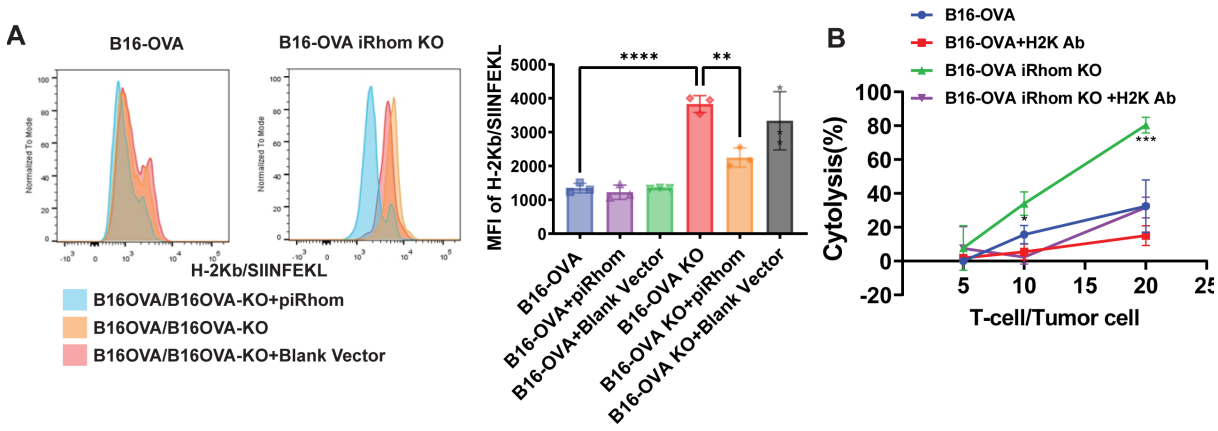

Figure 3-11. iRhom1 negatively regulates antigen presentation.

(A) Flow analysis of H2Kb/SIINFEKL presentation on B16-OVA and iRhom1 KO B16-OVA (B16-OVA KO) cells, with or without re-expression of iRhom1 (+piRhom). N = 3. Data are presented as mean ± s.e.m. *p < 0.05, **p < 0.01, ***p < 0.001. (B) Cytolysis of WT or iRhom1 KO B16-OVA cells co-cultured with CD8+ T cells isolated from spleens of OT-I mice, with or without blockade by H2K antibody (H2K Ab). N = 3. Data are presented as mean ± s.e.m. *p < 0.05, **p < 0.01, ***p < 0.001, ****p<0.0001.

presentation [189]. We generated iRhom1$^{-/-}$ B16-OVA as described above. As shown in **Fig. 3-11A**, the presentation of SIINFEKL/MHC-I complex was significantly enhanced in iRhom1$^{-/-}$

cells. Importantly, the enhanced Ag presentation was significantly attenuated when iRhom1 expression was reconstituted in KO cells via transfection with an iRhom1 plasmid. To examine the biological consequence of improved Ag presentation in iRhom1 KO cells, a cytotoxicity assay was conducted in which OVA-specific $CD8^+$ T cells (OT-1 T cells) were co-cultured with WT B16-OVA or iRhom1 KO B16-OVA cells. Increasing the OT-1 CD8+ T (effector cells) to B16-OVA (target cells) (E/T) ratio was associated with increased cytotoxicity towards both WT B16-OVA and $iRhom1^{-/-}$ B16-OVA cells (**Fig. 3-11B**). It was also apparent that OT-1 T cells exerted significantly more cytotoxicity on iRhom1 KO B16-OVA cells than on B16-OVA cells (**Fig. 3-11B**). In addition, the cytotoxicity on both cells was significantly attenuated by cotreatment with H2K-specific Ab. These data suggest that KO of iRhom 1 in B16-OVA led to a significant increase in H2K-mediated presentation of OVA antigen to OT-1 T cells, resulting in enhanced cytotoxicity.

To look for potential candidate(s) in Ag processing and presentation (APP) machinery that is regulated by iRhom1, we analyzed the proteomics data of TNBC patients in Clinical Proteomic Tumor Analysis Consortium (CPTAC), focusing on the major components involved in APP pathway. Interestingly, among 7 molecules examined, ERAP1 stands out as the only one whose protein expression levels were significantly and inversely correlated with the expression levels of iRhom1 (**Fig. 3-12A**). ERAP1 plays an important role in producing the peptide Ag presented by MHC-I molecules[190]. It is involved in trimming the SIINFEKL precursors to become the final SIINFEKL peptide that subsequently forms complex with MHCI molecules [190, 191]. ERAP1 is also reported to be a sheddase like ADAM17 [192, 193]. We hypothesized that ERAP1 may be similarly subjected to iRhom1-mediated regulation via PPI, which may play an important role in iRhom1-mediated immune response.

KO of iRhom1 led to increased levels of ERAP1 (**Fig. 3-12B**). In contrast, iRhom1 OE

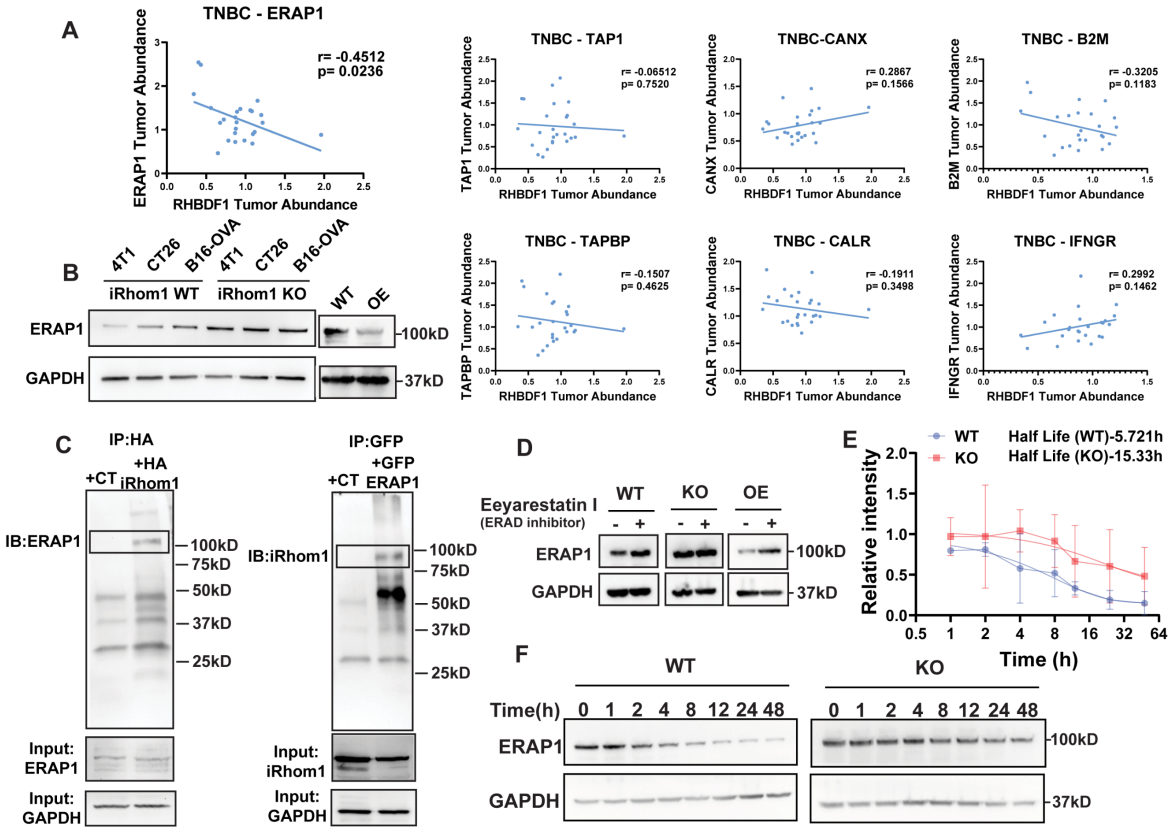

Figure 3-12. iRhom1 regulates ERAP1 stability through ERAD-mediated process.

(A) Proteomic data from CPTAC show that the protein expression levels of iRhom1 are negatively correlated with those of ERAP1 in the tumor samples of TNBC patients. There was no significant correlation with other APP-related proteins. N=25. (B) Changes in ERAP1 protein levels in various cancer cell lines following iRhom1 KO and OE. (C) Immunoprecipitation of HA-iRhom1 with anti-HA antibody led to pulldown of ERAP1 in 293T cells transfected with HA-iRhom1 expression plasmid and reciprocal immunoprecipitation of GFP-ERAP1 with anti-GFP beads led to pulldown of iRhom1 in 293T cells transfected with a GFP-ERAP1 expression plasmid. (D) Changes in ERAP1 protein levels in iRhom1 WT, KO and OE cells after treatment with Eeyarestatin I (4.5 μM), an ERAD inhibitor. (E) The stability (t1/2) of ERAP1 in iRhom1 WT and KO cells determined by cycloheximide chase experiment. The experiment was repeated 3 times and data were quantified by densitometry. (F) Representative WB of ERAP1 protein levels in cycloheximide chase experiments.

resulted in downregulation of ERAP1, further validating the negative regulation of ERAP1 by iRhom1 (**Fig. 3-12B**). **Fig. 3-12C** shows that an HA tag-specific antibody (Ab) effectively pulled down ERAP1 in 293T cells transfected with HA-iRhom 1 plasmid. Reciprocally, iRhom1 was

pulled down by GFP-ERAP1, suggesting a likely PPI between iRhom 1 and ERAP1. Endoplasmic-reticulum-associated protein degradation (ERAD) represents a critical pathway in regulating homeostasis and protein degradation in ER. IRhom1 has been reported to be involved in ERAD as a chaperone in regulating protein turnover [194, 195]. Indeed, treatment with Eeyarestatin 1, an ERAD inhibitor, led to increased level of ERAP1 protein in iRhom1 WT cells and OE cells but not in iRhom1 KO cells (**Fig. 3-12D**). Furthermore, KO of iRhom1 resulted in increased protein stability of ERAP1 as shown in a cycloheximide chase assay (**Fig. 3-12E&F**). Taken together, the above data provides the first evidence that iRhom1 inhibits antigen presentation at least partly through regulating the ERAD-mediated degradation of ERAP1 in ER.

3.3.3 Development of a PCL-CP-based nanocarrier for co-delivery of pre-siiRhom and a chemotherapy agent

Our data thus far as well as those from others suggest that iRhom1 may represent a novel and attractive therapeutic target for cancer, especially in combination with other treatment such as chemotherapy. However, no small molecule inhibitors are currently available for iRhom1. Therefore, we developed a new therapy based on a combination of siiRhom1 and chemotherapy drugs using a new polymeric nanocarrier PEG-Chitosan-Lipid (PCL). A bioengineered iRhom1 pre-siRNA (pre-siiRhom) was used to achieve iRhom1 knockdown. Pre-siRNA is generated by fermentation and is biotransformed into mature siRNA upon intracellular delivery. Folded within cells and without chemical modification, the pre-siRNA better captures the safety profile of natural RNAs and has potential to scale up [196, 197]. The PCL nanocarrier was designed to be equipped with several unique features (**Fig. 3-13A**): *1*) A lipid motif was introduced to facilitate interactions

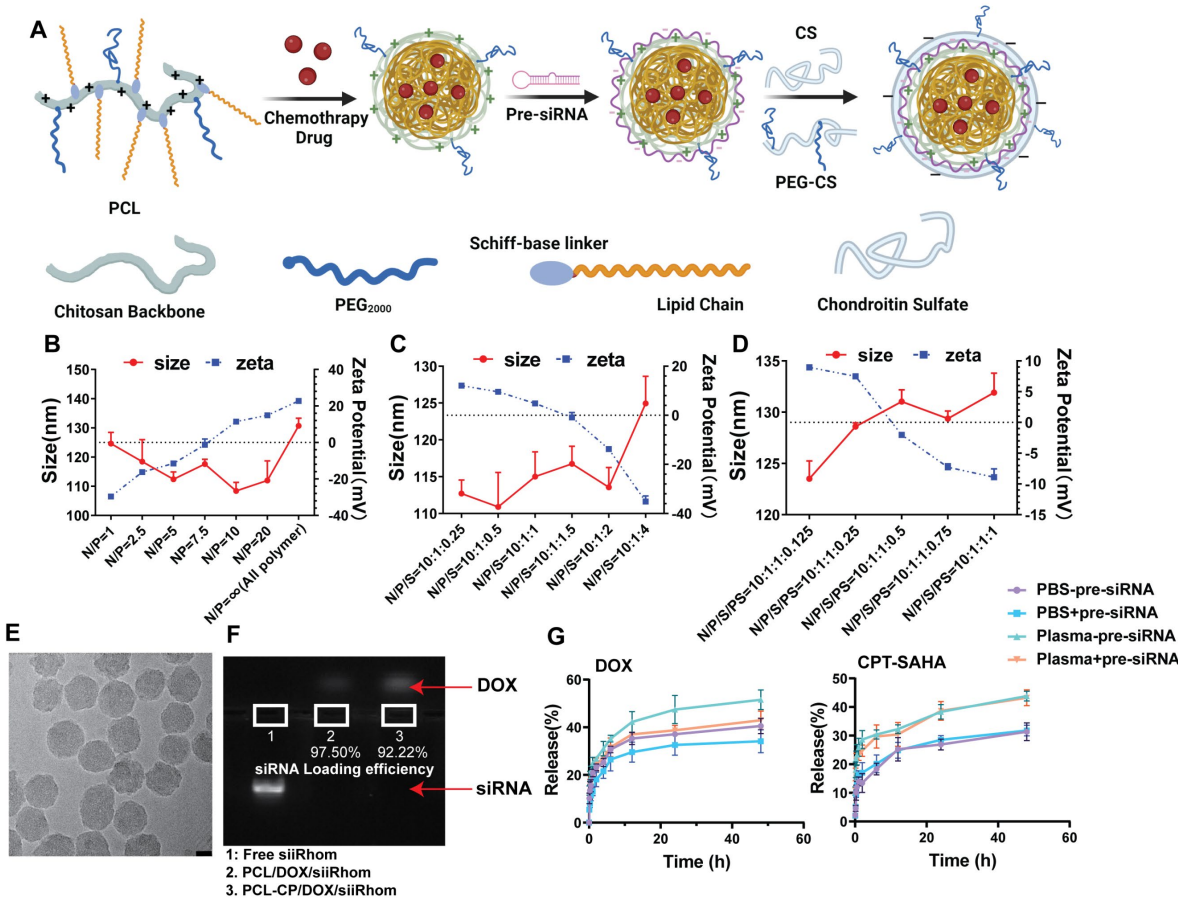

Figure 3-13. iRhom1 regulates ERAP1 stability through ERAD-mediated process.

Biophysical characterizations of DOX (CPT-SAHA)/pre-siRNA-coloaded PCL-CP NPs. (A) A schematic diagram of the protocol for the preparation of DOX (CPT-SAHA)/pre-siRNA-coloaded PCL-CP NPs. (B) Sizes and zeta potentials of PCL/DOX (CPT-SAHA)/pre-siRNA complexes at various N/P ratios. (C) Sizes and zeta potentials of DOX/pre-siRNA-coloaded PCL-C NPs (coated with CS alone) at various N/P/S ratios. (D) Sizes and zeta potentials of DOX/pre-siRNA-coloaded PCL-CP NPs (coated with a mixture of CS and PEG-CS) at various N/P/S(CS)/S(PEG-CS) ratios. (E) Cryo-EM characterization of DOX/pre-siRNA-coloaded PCL-CP NPs prepared at a carrier/drug ratio of 10:1 and a N/P/S/S ratio of 10:1:1:0.5. Bar: 20nm. (F) Gel retardation assay of DOX/pre-siRNA-coloaded PCL-CP NPs. Carrier/drug ratio=10:1, N/P/S/S=10:1:1:0.5. (G) In vitro release of DOX or CPT-SAHA from PCL-CP NPs in PBS or plasma.

with cell membrane and improve transfection [198] while also helps to improve the loading of hydrophobic/lipidic drugs such as DOX or CPT-SAHA into the lipophilic core; *2*) Chitosan was chosen as the backbone to improve biodegradability; *3*) **C**S (chondroitin sulfate, 10~30K)/**P**EG2K-CS were used to coat the PCL micelles coloaded with DOX (or CPT-

SAHA)/pre-siRNA to generate PCL-**CP** NPs with neutral or slightly anionic surface. CS, as a natural ligand of CD44, was also included to mediate active targeting of tumor cells and tumor endothelial cells (ECs) as CD44 is overexpressed in both types of cells. PEG2K-CS was included to minimize the "nonspecific" uptake by RES. DOX or CPT-SAHA could be effectively loaded into PCL micelles through hydrophobic interaction with lipid motif in PCL (**Table. 3-1**). PCL/DOX (CPT-SAHA) readily formed complexes with pre-siRNA at various N/P ratios through charge-charge interaction between cationic amine group of PCL and anionic pre-siRNA (**Fig. 3-13B**). At a N/P ratio of 10/1, DOX/pre-siRNA-coloaded micelles were ~110 nm in size, smaller than that of PCL micelles loaded with DOX alone (170~190nm) (**Fig. 3-13B**), suggesting that pre-siRNA could physically wrap around and stabilize the micelles. Subsequent coating with anionic CS/PEG-CS on the cationic surface of PCL/DOX(CPT-SAHA)/pre-siRNA micelles led to formation of PCL-CP NPs that gradually became anionic with increasing amounts of CS/PEG-CS (**Fig 3-13C-D**). **Fig. 3-13E** shows a cryo-EM image of PCL-CP NPs at a N (nitrogen of PCL polymer)/P (phosphate of pre-siRNA)/S (sulphate of CS)/S (sulphate of PEG-CS) ratio of 10/1/1/0.5. Pre-siRNA was effectively loaded into NPs. Lack of fluorescence signal of pre-siRNA in the sample of pre-siRNA-loaded PCL or PCL-CP suggests the formation of tight PCL polymer/pre-siRNA complex, resulting in the exclusion of ethidium bromide from pre-siRNA (**Fig. 3-13F**). PCL-CP NPs showed slow kinetics of release of DOX or CPT-SAHA in PBS and

the drug release was slightly accelerated in serum. Consistent with its effect in reducing the size of the NPs, pre-siRNA also slowed down the release of DOX in either PBS or serum (**Fig. 3-13G**). Interestingly, chitosan modified with PEG and lipid through a Schiff base remained sensitive to digestion by chitosanase and DOX (CPT-SAHA)/pre-siRNA-coloaded PCL-CP NPs rapidly became disassembled in the presence of chitosanase (**Fig. 3-14**). In contrast, modification of

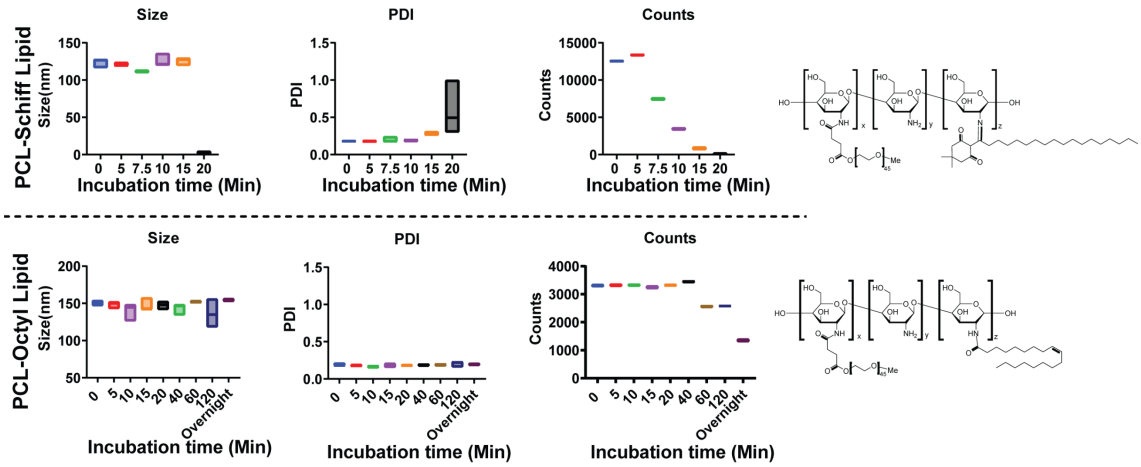

Figure 3-14. Chitosanase-mediated degradation of PCL derivatized with lipid with a Schiff-base or amide linker.

chitosan via the commonly used amide bond [199] led to a drastic decrease in sensitivity to chitosanase. Therefore, our PCL-CP NPs retain the biodegradability of chitosan, which is critical for *in vivo* therapeutic application.

Table 3-1 Biophysical characterization of DOX (CPT-SAHA)-loaded PCL micelles at various carrier/drug ratios (w/w).

Drug	Polymer:drug ratio	Size	PDI	Zeta potential	Loading efficiency	Loading capacity
DOX	5:1	184.93±0.63	0.132±0.021	-5.40±1.13	81.53%	16.31%
	10:1	173.15±0.71	0.143±0.048	2.86±0.55	84.26%	8.42%
CPT-SAHA	5:1	125.1±0.7	0.195±0.020	-4.27±0.61	74.37%	14.87%
	10:1	112.53±0.97	0.200±0.015	-3.27±0.21	82.91%	8.29%

3.3.4 Role of CD44 in tumor endothelial cells (ECs) and tumor cells in the tumor accumulation and penetration of PCL-CP NPs

The effectiveness of tumor-targeting by our PCL-CP NPs is likely attributed to both EPR and CS/CD44-mediated active targeting. Our recent study suggested an important role of targeting of tumor ECs through CD44 in the overall tumor targeting [72]. To further elucidate the respective roles of CD44-mediated transcytosis in tumor ECs and tumor cells, we also generated $CD44^{-/-}$ HUVEC and CT26 cells, respectively. HUVECs cultured in the presence of growth factors express a relatively high level of CD44 and have been used to model tumor ECs. We first established WT or $CD44^{-/-}$ tumors in either WT or $CD44^{-/-}$ mice and then investigated the tissue distribution of the NPs via both imaging and HPLC analysis. **Fig. 3-15A&B** show that KO of CD44 in mice led to a drastic reduction of Cy5.5 signals in both tumors and liver regardless of the CD44 status in the tumor cells. KO of CD44 in the tumor cells also caused deceases of the Cy5.5 signals in tumors in both WT and $CD44^{-/-}$ mice but to a much lesser extent. Fluorescence microscopic examination of tumor sections shows widespread distribution of Cy5.5 signals in the WT tumors grown in WT mice. The Cy5.5 signals in $CD44^{-/-}$ tumors grown in WT mice were largely confined to areas

adjacent to blood vessels ($CD31^{+}$). KO of CD44 in mice led to drastic decreases in the Cy5.5 signals in the tumors, particularly the $CD44^{-/-}$ tumors (**Fig. 3-15C**). Similar results were shown in quantitative analysis of DOX distribution (**Fig. 3-15D&E**).

Fig. 3-16B&D show the results of a transwell assay with both WT and $CD44^{-/-}$ HUVECs. Various Cy5.5-labeled NPs were added to the upper chamber and the samples were collected from

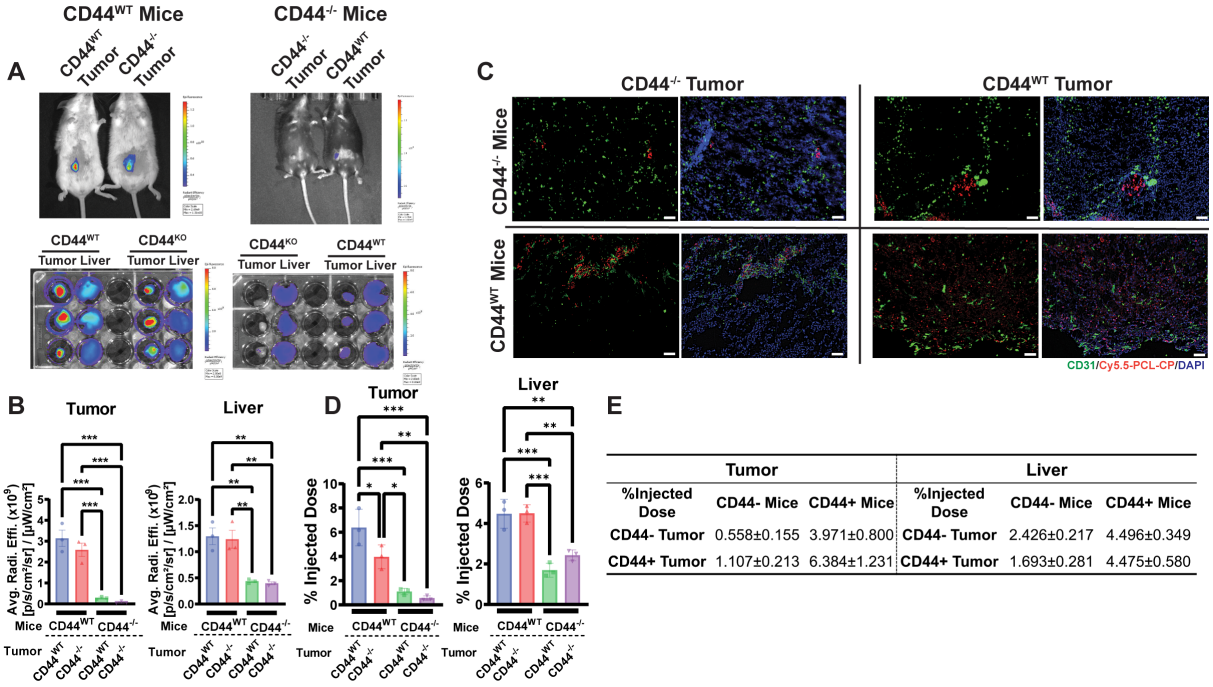

Tumor			Liver		
%Injected Dose	CD44- Mice	CD44+ Mice	%Injected Dose	CD44- Mice	CD44+ Mice
CD44- Tumor	0.558±0.155	3.971±0.800	CD44- Tumor	2.426±0.217	4.496±0.349
CD44+ Tumor	1.107±0.213	6.384±1.231	CD44+ Tumor	1.693±0.281	4.475±0.580

Figure 3-15. Role of CD44 in tumor endothelial cells and tumor cells.

(A) NIRF whole body imaging, ex vivo imaging of CD44 WT or KO tumor-bearing CD44 WT or KO mice at 24 h following i.v. administration of DiR-loaded, Cy5.5-labled PCL-CP NPs. (B) Quantification of ex vivo imaging data from (A). N=3. Data are presented as mean ± s.d. *$p < 0.05$. (C) Fluorescence images of frozen tumor core sections from CD44 WT or KO tumor grown on CD44 WT or KO mice at 24 h after treatment with Cy5.5-labled PCL-CP NPs. CD31 was stained with FITC-labeled antibody to show the endothelial cells. Bar=50 μm. (D) Biodistribution of DOX loaded in DOX/pre-siRNA-coloaded PCL-CP NPs in CD44 WT or KO tumor-bearing CD44 WT or KO mice at 24 h following i.v. administration. N=3. Data are presented as mean ± s.d. (E) Quantitative analysis of biodistribution of DOX in CD44 WT or KO tumor-bearing CD44 WT or KO mice at 24 h following i.v. administration. N=3. Data are presented as mean ± s.d.

the lower chamber at various time intervals (**Fig. 3-16A**). Significantly greater amounts of fluorescence signals were found in the lower chamber with the NPs coated with CS. The amounts

of the signals were significantly decreased when the cells were co-treated with chlorpromazine, an endocytosis inhibitor, suggesting that the CS-decorated NPs are capable of crossing the EC through an active process of transcytosis. It should be noted that this process was essentially abolished in a transwell with CD44$^{-/-}$ HUVECs (**Fig. 3-16D**), suggesting a critical role of CS/CD44 interaction in the cellular uptake and transcytosis of CS-coated NPs. Similar results were observed

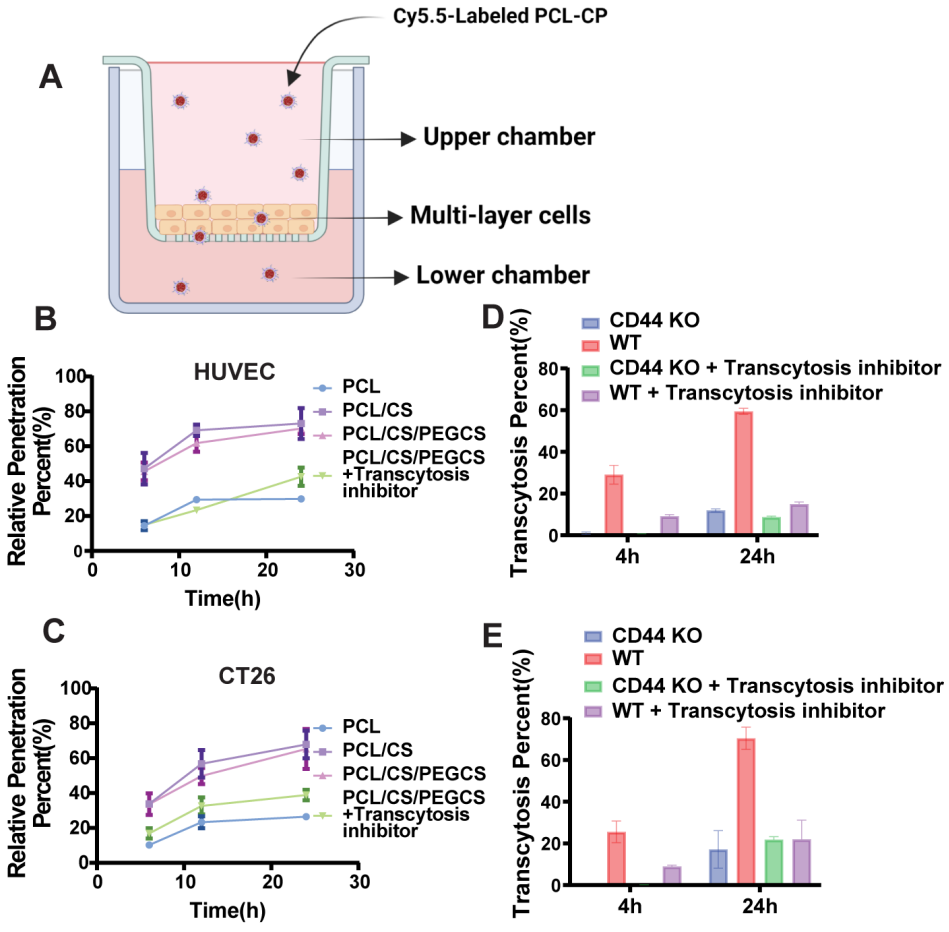

Figure 3-16. CD44 mediates the transcytosis of PCL-CP NPs in tumor endothelial cells and tumor cells.

(A) Illustration of transwell study. (B-E) Transwell assay of transmigration of Cy5.5 labeled PCL NPs, PCL-C NPs or PCL-CP NPs (with or without pretreatment with a transcytosis inhibitor) across HUVEC cells (B), CT26 cells (C), CD44 KO HUVEC cells (D), or CD44 KO CT26 cells (E). Fluorescence intensity of the medium in the lower chamber was measured to calculate the percentage of transmigration at indicated time points. N = 3. Data are presented as mean ± s.d. *p < 0.05, **p < 0.01, ***p < 0.001, ****p<0.0001.

in a transwell study with WT and CD44$^{-/-}$ CT26 cells (**Fig. 3-16C&E**). **Fig. 3-17A** shows the results of NPs penetration in an CT26 tumorsphere. It is apparent that CS-coated but not non-coated NPs effectively penetrated and reached the core of the tumorsphere. Again, this process was significantly attenuated by an endocytosis inhibitor. Furthermore, the CS-mediated NP penetration was only seen in WT but not CD44$^{-/-}$ CT26 tumorsphere (**Fig. 3-17B**), suggesting a role of CS/CD44-mediated transcytosis in tumor penetration.

CD44-mediated tumor targeting has been studied for decades but the underlying mechanism remains elusive, especially the respective role of CD44 in tumor ECs and tumor cells.

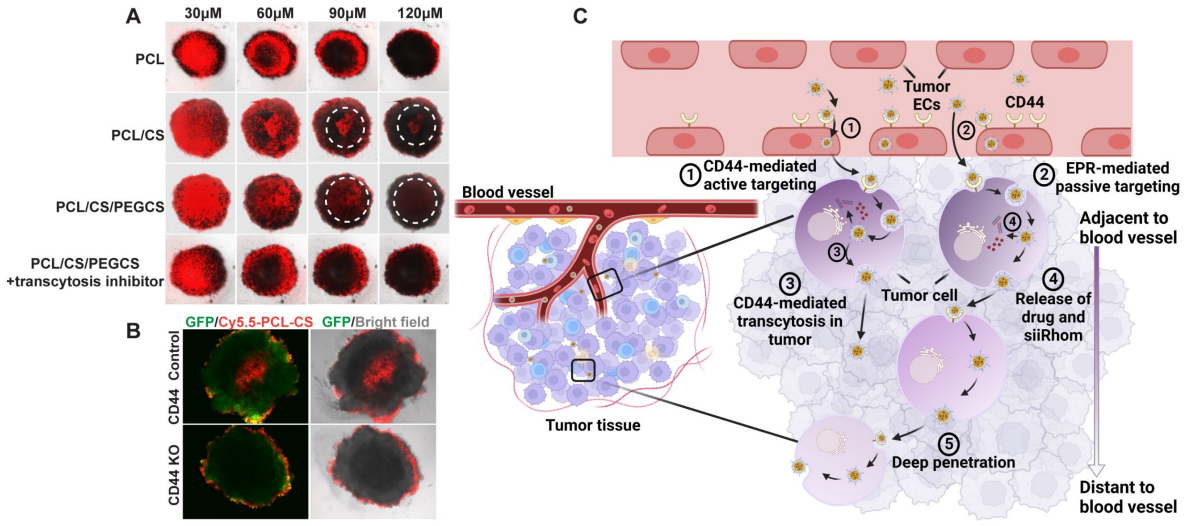

Figure 3-17. CD44 mediates the tumor penetration of PCL-CP NPs in tumor cells.

(A) Confocal z-stack images of CT26 tumor cell spheroids after 18 h incubation with Cy5.5-labeled PCL NPs, PCL-C NPs or PCL-CP NPs (with or without pretreatment with a transcytosis inhibitor). White circles highlight the efficient penetration of CS-coated NPs. (B) Confocal z-stack images of the middle sections of CD44 WT or KO CT26-GFP spheroids after 18 h incubation with Cy5.5-labeled PCL-CP NPs. (C) Proposed role of the CD44 in tumor ECs and tumor cells in mediating tumor targeting and penetration of CS-coated NPs.

Most studies seem to suggest a mechanism that involves EPR followed by targeting to CD44 on tumor cells [200]. Our data suggests that the tumor endothelial CD44-mediated internalization and transcytosis play a more important role than either EPR or tumor cell CD44-mediated targeting in

the total amounts of NPs accumulated in the tumor tissues (**Fig. 3-17C**). Following extravasation, the internalization and transcytosis that are mediated by the tumor cell CD44 contribute to the penetration of the CS-coated NPs in tumor tissues (**Fig. 3-17C**). This information may be highly significant for the future design of more effective tumor-targeting NPs.

3.3.5 Inhibition of iRhom1 further improves CD44-dependent tumor targeting by decreasing CD44 cleavage on the cell membrane

The extracellular domain that is responsible for CD44 ligand binding is constitutively cleaved at membrane-proximal region by metalloprotease in cancer cells [201]. However, its implication in CD44-mediated tumor targeting via nanomedicine has never been studied. IRhom1 is reported to regulate the trafficking of ADAM17, one of the major metalloproteases that are involved in CD44 cleavage [202, 203]. To investigate whether iRhom1 KO affects CD44-mediated tumor targeting, cellular uptake of PCL NPs with or without CS coating was examined in WT and iRhom1 KO or KD tumor cells. **Fig. 3-18A** shows that iRhom1 KO or KD further improved CS/CD44-mediated cellular uptake. Similarly, iRhom1 KO further improved the CS/CD44-mediated transcytosis (**Fig. 3-18B**). NIRF imaging shows more signals of the NPs in iRhom1 KO tumors compared to WT tumors (**Fig. 3-18C**). Similar results were shown with quantitative analysis of DOX distribution in tumors (**Fig. 3-18D**). **Fig. 3-19A&B** show that the CD44 extracellular region was upregulated in iRhom1$^{-/-}$ CT26 cells compared to WT CT26 cells. Western

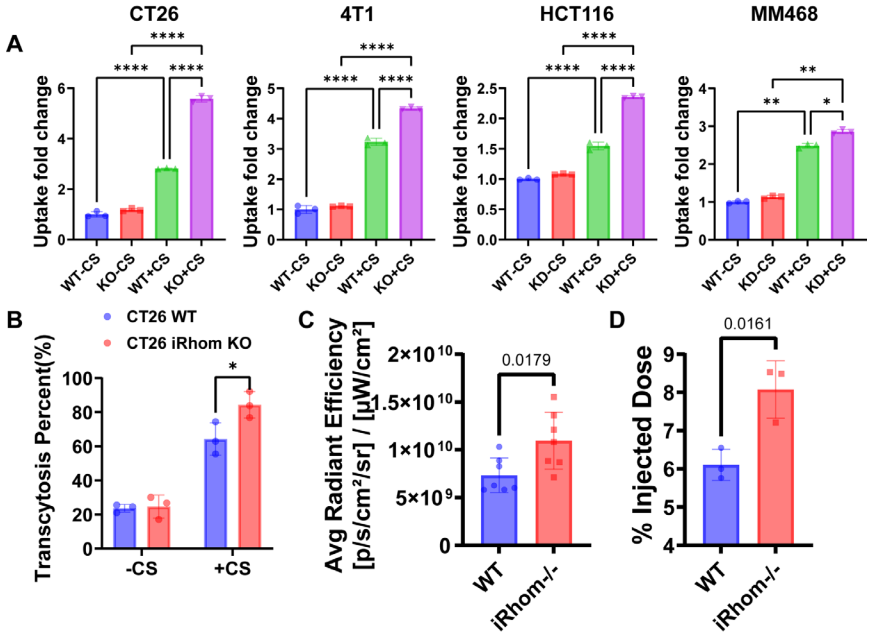

Figure 3-18. IRhom1 KO enhanced the CD44-mediated cell uptake of PCL-CP NPs.

(A) Cellular uptake of Cy5.5 labeled PCL NPs with or without CS coating in various WT or iRhom1 KO cell lines. N=3. Data are presented as the mean ± s.e.m. *p < 0.05, **p < 0.01, ***p < 0.001, ****p<0.0001. (B) Transwell assay of transmigration of Cy5.5 labeled PCL NPs with or without CS coating across WT or iRhom1 KO CT26 cells. Fluorescence intensity of the medium in the lower chamber was measured to calculate the percentage of transmigration at 24h. N=3. Data are presented as the mean ± s.e.m. *p < 0.05, **p < 0.01, ***p < 0.001, ****p<0.0001. (C) Quantification of NIRF whole body imaging at 24 h following i.v. administration of DOX-loaded, Cy5.5-labled PCL-CP NPs. N=7. Data are presented as mean ± s.e.m. (D) Quantitative analysis of biodistribution of DOX in WT or iRhom1 KO tumor-bearing mice (WT) at 24 h following i.v. administration. N=3. Data are presented as mean ± s.e.m.

blotting further showed the upregulation of the full length CD44 (CD44-full), along with downregulation of the cleaved membrane-associated CD44 (CD44-EXT) in iRhom KO or KD cells, suggesting the inhibition of CD44 cleavage in iRhom KO or KD cells (**Fig. 3-19C**). As

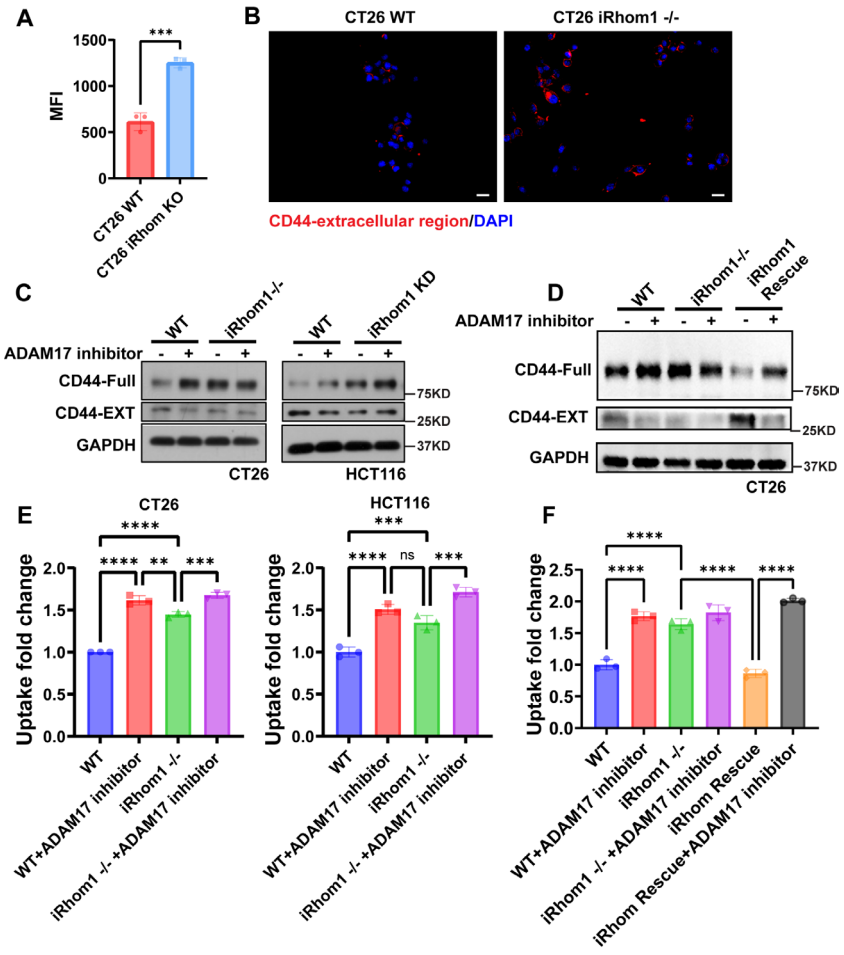

Figure 3-19. IRhom1 KO enhance CD44-mediated cell uptake by downregulating the CD44 cleavage.

(A) CD44 expression levels measured by flow cytometry by staining with an antibody recognizing the CD44 external region. (B) Fluorescence images of CD44 expression in WT or iRhom1 KO CT26 cells. CD44 was stained with an antibody recognizing the CD44 external region (Bar=20 μm). (C) Changes in protein levels of full-length CD44 (CD44-Full) and the cleaved, CD44 membrane-bound fragment (CD44-EXT) in WT or iRhom1 knockout/knockdown cells, with or without ADAM17 inhibitor pretratment (blotted by an antibody recognizing the CD44 intracellular domain). (D) Changes in protein levels of CD44-Full and CD44-EXT in WT, iRhom1 KO and iRhom1 rescue cells, with or without ADAM17 inhibitor treatment. (E-F) Cellular uptake of Cy5.5 labeled PCL-CS NPs in (E) WT or iRhom1 knockout/knockdown cells and (F) WT, iRhom1 knockout/knockdown or iRhom1 rescue cells with or without ADAM17 inhibitor pretreatment. N=3. Data are presented as mean ± s.e.m. *p < 0.05, **p < 0.01, ***p < 0.001, ****p<0.0001.

iRhom1 regulates ADAM17 activity in CD44 cleavage, we pretreated WT and iRhom KO or KD cells with TMI, an ADAM17 inhibitor. WT cells treated with ADAM17 inhibitor showed similar amounts of CD44-full compared to iRhom1 KO or KD cells, while ADAM17 inhibitor barely

improved the CD44-full amount in iRhom1 KO or KD cells (**Fig. 3-19C**). Rescue of iRhom1 led to significant CD44 cleavage and this effect can be blocked by ADAM17 inhibitor (**Fig. 3-19D**). **Fig. 3-19E** shows that cells treated with ADAM17 inhibitor mimicked the phenotype of iRhom KO or KD cells in cellular uptake. In addition, rescue of iRhom1 abolished the enhanced uptake (**Fig. 3-19F**). The above data suggests that iRhom1 can regulate CD44-mediated tumor targeting and transcytosis by affecting CD44 cleavage through iRhom1-ADAM17-CD44 axis.

3.3.6 Co-delivery of pre-siiRhom and chemotherapy agent led to improved anti-tumor efficacy and enhanced antitumor immunity

Fig. 3-20A shows the antitumor activity of different treatments in 4T1 orthotopic TNBC breast tumor model. NPs loaded with pre-siiRhom or DOX alone showed modest antitumor activity. Codelivery of pre-siiRhom and DOX via PCL-CP NPs led to significant improvement in therapeutic efficacy. Similar results were also demonstrated with the NPs co-loaded with pre-siiRhom and CPT-SAHA in CT26 CRC model (**Fig. 3-20C**). All treatments were well tolerated as evident from similar changes in body weights over time compared to the control group (**Fig. 3-20B&D**).

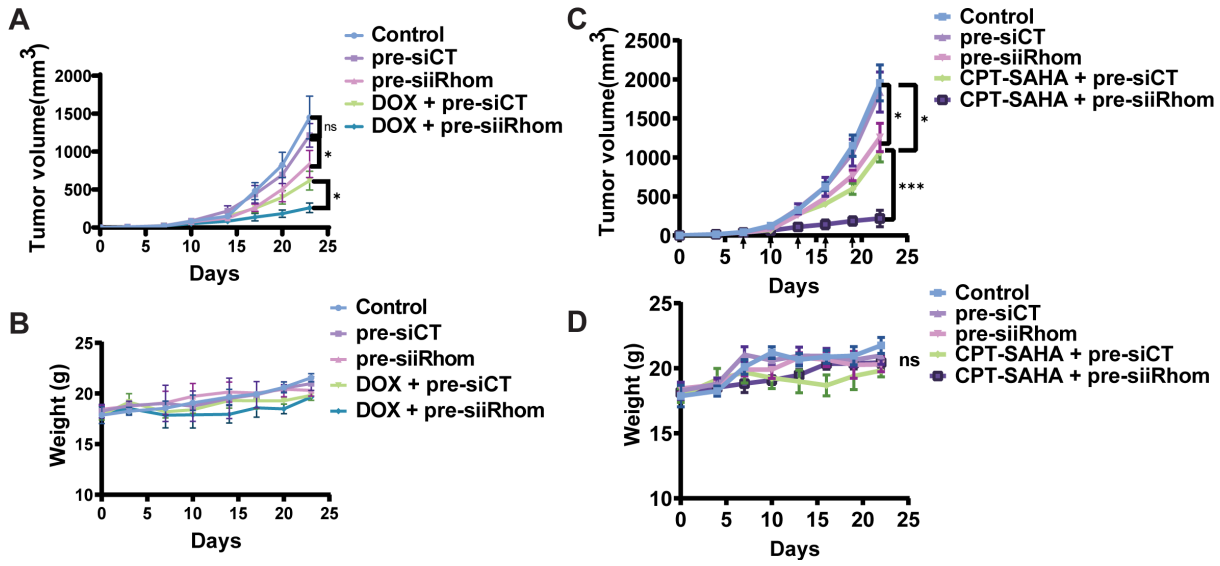

Figure 3-20. Treatment with DOX (CPT-SAHA)/pre-siiRhom PCL-CP NPs led to enhanced therapeutic efficacy.

(A-B) Changes in tumor volumes (A) and body weights (B) in mice bearing 4T1 orthotopic tumors receiving various treatments. N = 5. Data are presented as mean ± s.e.m. *p < 0.05, **p < 0.01, ***p < 0.001. (C-D) Changes in tumor volumes (C) and body weights (D) in mice bearing CT26 tumors receiving various treatments. N=5. Data are presented as mean ± s.e.m. *p < 0.05, **p < 0.01, ***p < 0.001).

KD of iRhom1 via the NPs led to a significant improvement in tumor immune microenvironment as evident from increases in both the total numbers of $CD8^+$ T cells and the numbers of functional ($IFN\gamma^+$ or $GzmB^+$) $CD8^+$ T cells. Inclusion of DOX had no significant impact on these profiles (**Fig. 3-21A**). Interestingly, CPT-SAHA alone showed modest effect in upregulating the total numbers of $CD4^+$ T cells, $CD8^+$ T cells and the numbers of functional ($IFN\gamma^+$ or $GzmB^+$) $CD8^+$ T cells (**Fig. 3-21B**). Combination of iRhom1 KD and CPT-SAHA led to further improvement in tumor microenvironment. Flow analysis of isolated tumor cells showed significant upregulation of MHC1 following treatment with pre-siiRhom or CPT-SAHA, especially the combination of both via NPs (**Fig. 3-21C**).

Fig. 3-21B shows that there was significant upregulation of PD-1 expression in $CD8^+$ T-cells treated with CPT-SAHA, alone or together with pre-siiRhom, suggesting a potential of combining with anti-PD-1 to further improve the cancer treatment. Indeed, combination of CPT-

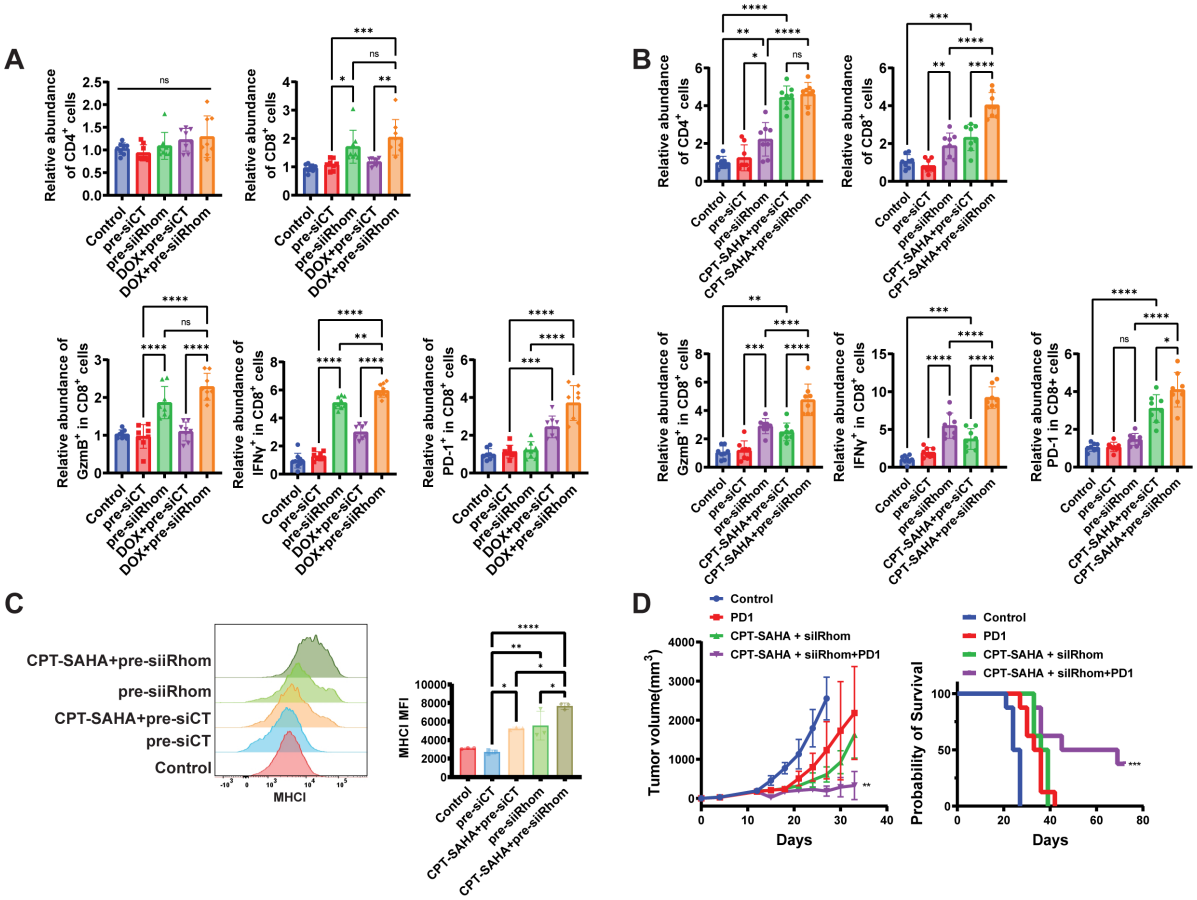

Figure 3-21. Treatment with DOX (CPT-SAHA)/pre-siiRhom PCL-CP NPs led to improved TIME.

(A-B) Representative flow cytometric analysis and the quantification of the relative abundance of $CD8^+$ T-cells, $CD4^+$ T-cells, $CD8^+$ $IFN\gamma^+$ T-cells, $CD8^+$ Granzyme B^+ T-cells and $CD8^+$ $PD1^+$ T-cells in (A) 4T1 and (B) CT26 tumor tissues after various treatments. N=8. Data are presented as mean ± s.e.m. *$p < 0.05$, **$p < 0.01$, ***$p < 0.001$, ****$p<0.0001$. (C) Histogram and the quantitative analysis of MHCI expression in CT26 tumor tissues after various treatments. N=3. Data are presented as mean ± s.e.m. *$p < 0.05$, **$p < 0.01$, ***$p < 0.001$, ****$p<0.0001$). (D) Tumor growth inhibition and survivals of CT26 tumor-bearing mice receiving various treatments. N=8. Data are presented as the mean ± s.e.m. *$p < 0.05$, **$p < 0.01$, ***$p < 0.001$.

SAHA/pre-siiRhom/PCL-CP and anti-PD1 antibody (aPD-1) led to significant improvement in the antitumor activity as demonstrated by significant prolongation of survival time. In addition, 2 out

of the 8 mice in the combination group showed complete tumor eradication 7 days following the 5th treatment (**Fig. 3-21D**).

3.4 Discussion

Using several cancer models, we have extended previous works on the potential role of iRhom1 in oncogenesis and drug response. In addition, we have shown for the first time that iRhom1 inhibits antitumor immune response by negatively regulating the stability of ERAP1 and the ERAP1-mediated Ag processing and presentation. In addition, chemotherapy-induced iRhom1 expression may contribute to immune escape through the iRhom1-ERAP1 axis, suggesting a new mechanistic link between chemoresistance and immunoresistance.

MAPK14/HSP27 axis has been reported to be involved in drug resistance to cisplatin, 5-fluorouracil, taxanes and DOX in BC, CRC and lung cancer [184, 204-208]. However, the underlying mechanisms of how MAPK14/HSP27 is regulated remain to be further elucidated. IRhom1 KO or KD resulted in significantly decreased phosphorylation of both MAPK14 and HSP27, which was correlated with increased sensitivity to DOX and CPT-SAHA in 4T1 and CT26 cells, respectively. Importantly such changes were significantly attenuated when iRhom1 expression was reconstituted via transient transfection. In addition, OE of iRhom1 led to decreased drug sensitivity in both 4T1 and CT26 cells. Interestingly, treatment with DOX or CPT-SAHA led to a further increase in iRhom1 expression, suggesting a likely role of iRhom1 in regulating both intrinsic and acquired resistance. The detailed mechanism of how iRhom1 regulates the level of p-MAPK14 is not clear at present. Our preliminary data show that iRhom1 KO does not affect the phosphorylation of the upstream kinase MKK3/6 but disrupts the interaction of pMKK3/6 and

MAPK14. It is possible that iRhom1 serves as a scaffold to facilitate the phosphorylation of MAPK14 or improve the stability of p-MAPK14. It should be noted that iRhom1 KO also led to upregulation of other signaling pathways such as AKT that may also play an important role in cancer cell survival and drug resistance [209].

IRhom1 KO also led to activation of several immune pathways including antigen processing and presentation (APP) pathway. Interestingly, despite upregulation of several APP-related genes at transcriptional level in RNAseq and qRT-PCR, only ERAP1 showed significant upregulation at protein level following iRhom1 KO. Regulation of ERAP1 protein level by iRhom1 was further confirmed by the data that OE of iRhom1 led to decreased protein level of ERAP1. The PPI between iRhom1 and ERAP1 was also confirmed by pull-down assay. IRhom1 appears to decrease ERAP1 stability through facilitating its degradation via the endoplasmic reticulum-associated *degradation (ERAD) pathway. ERAP1 has been well studied and shown to play an important role in Ag processing, such as in trimming* the OVA SIINFEKL precursors to become the final SIINFEKL peptide. The significance of iRhom1/ERAP1 interaction was demonstrated by the data that iRhom1 KO or KD led to significant improvement in the presentation of SIINFEKL antigen, resulting in significantly enhanced lysis of OVA-B16 cells in a coculture assay with OT-1 T cells. Although iRhom1 likely affects antitumor immunity directly or indirectly through multiple mechanisms, our data strongly support the notion that iRhom1 inhibits the cytotoxic T-cell response at least partly by reducing the stability of ERAP1 protein and the ERAP1-mediated antigen processing and presentation. Our preliminary data show that KD of iRhom2 had no significant impact on the protein expression level of ERAP1. Whether and how iRhom2 regulates antitumor immunity requires more study in the future.

Numerous reports have been published on CD44-mediated tumor targeting using *hyaluronic acid* (HA) or CS-decorated NPs. One major limitation with this targeting strategy is the expression of CD44 on liver sinusoidal endothelial cells (LSECs) that remove most of the NPs in blood due to their abundance. However, the level of CD44 on LSECs is significantly lower than that on tumor cells or tumor ECs. Therefore, decoration of the NPs with "optimal" amounts of PEG shall lead to drastic reduction in the interaction of the NPs with LSECs without significantly compromising their productive interaction with tumor ECs and/or tumor cells. We have demonstrated the success of this strategy initially with PMBOP-CP NPs [72] and now with the new biodegradable PCL-CP NPs: the injected NPs were largely concentrated at tumor site along with decreased uptake by liver. We have further systematically studied the mechanism of tumor targeting and penetration using 2D, 3D, and mouse tumor models generated with WT and $CD44^{-/-}$ tumor cells, and WT and $CD44^{-/-}$ mice. Our data suggest that accumulation of the NPs at tumor site is largely achieved through targeting of CD44 on tumor ECs. Following intracellular delivery into tumor ECs, parts of the NPs are released into the cytosol from endosome/lysosomes while significant amounts of NPs reach the tumor cells through transcytosis. At the same time, small amounts of NPs reach the tumor cells through EPR. Once extravasation, the above process will continue through layers of tumor cells, leading to both intracellular delivery of cargos and deep penetration of the NPs in the tumor tissues. The release of cargos (drug/siRNA) or the entire PCL-CP NPs from endosome may result from protonation of the primary amines of the glucosamine residues as the endosome matures and becomes more acidic, leading to a high charge density and membrane destabilization [210, 211]. The presence of lipid chain in PCL polymer shall further facilitate the interaction of the NPs with the endosome membrane. In addition, enzymatic degradation of chitosan further induces the escape from endosomes/lysosomes, which is driven by

intravesicular osmotic swelling [212]. Interestingly, KO of either iRhom1 or iRhom2 decreases CD44 cleavage and further improves the CD44-mediated tumor targeting of NPs likely through decreasing the activity of ADAM17. This is consistent with literature that ADAM17 mediates the cleavage of CD44 extracellular domain (ectodomain) in various types of cells including tumor cells [213, 214]. It should be noted that ADAM17 inhibitors are currently being evaluated as new therapeutics for treatment of various types of cancers [215-217]. Therefore, ADAM17 inhibitors and CD44-targeting NPs may be combined to achieve synergistic antitumor activity.

Targeted delivery of iRhom1 pre-siRNA alone led to a modest antitumor activity along with increased numbers of $CD8^+$ T cells. Codelivery of iRhom1 pre-siRNA with DOX or CPT-SAHA led to further improvement in both the overall therapeutic efficacy and tumor immune microenvironment. The superior antitumor activity of the combination therapy is likely attributed to several mechanisms including the direct growth inhibiting activity of iRhom1 KD, the increased sensitivity of tumor cells to chemotherapy agents, and activated antitumor immune response. Importantly, this new approach can be combined with anti-PD1 antibody to further improve the therapeutic outcome. Targeting iRhom1 in combination with chemotherapy may represent a new and effective immunochemotherapy for the treatment of various types of cancers including breast and colon cancers.

4.0 Conclusion and perspective

This PhD thesis addresses the limitations of current tumor delivery strategies and proposes two novel approaches to enhance both tumor targeting and penetration. These approaches include: 1) the development of ultrasmall PAZA NPs for enhanced tumor accumulation and penetration, and 2) the development of chitosan-coated PCL-CP NPs for CD44-mediated tumor targeting. We conducted a systematic investigation into the targeting mechanism and identified potential factors that may influence tumor targeting and penetration.

The initial approach involves the development of small-sized nanocarriers, which are anticipated to enhance tumor targeting and penetration by taking advantage of the permeability of blood vessels and cellular gaps [131-133]. Moreover, it has been reported that nanoparticles with a particle size smaller than 20 nm offer greater advantages in addressing interstitial fluid pressure (IFP) and extracellular matrix (ECM), thereby facilitating enhanced deep tissue penetration [134]. Our study has shown that small-sized PAZA NPs are more effective than large-sized PVD NPs in reaching the tumor. However, the mechanistic study demonstrated that tumor penetration is not exclusively reliant on the small size effect but is also linked to the PC composition on the NPs. In particular, there was an increase in the concentration of FN in the corona of PAZA NPs. The FN interacts with the ITGA5 receptor on tumor cells, thereby facilitating increased tumor cellular uptake and transcytosis of PAZA NPs, ultimately resulting in improved tumor penetration. This study provides a novel perspective for the development of a targeted strategy for tumor activity. Instead of utilizing artificial ligands for conjugation, ligand-free NPs can also acquire tumor-targeting properties following the administration involves recruiting the tumor-homing protein FN.

However, the potential factors that determine the component of PC remain elusive and warrant further study.

The second approach involves the development of a CD44-targeting nanocarrier designed to enhance tumor targeting and penetration via CD44-mediated mechanisms. Several studies have been conducted on the CD44-mediated targeting using hyaluronic acid (HA) or CS-decorated NPs. One major limitation with this targeting strategy is the expression of CD44 on liver sinusoidal endothelial cells (LSECs), which results in the clearance of the majority of NPs in blood due to their high abundance. Nevertheless, the expression level of CD44 on LSECs is significantly lower compared to that on tumor cells or tumor ECs. Therefore, decoration of the NPs with "optimal" amounts of PEG shall lead to drastic reduction in the interaction between the NPs and LSECs, while maintaining their effective interaction with tumor ECs and/or tumor cells. The success of this strategy has been demonstrated in the present study. Furthermore, we have conducted a comprehensive investigation into the mechanism of tumor targeting and penetration by utilizing 2D, 3D, and mouse tumor models created with WT and CD44-/- tumor cells, as well as WT and CD44-/- mice. Our data indicates that the accumulation of the NPs at tumor site is largely achieved through targeting of CD44 on tumor ECs, while CD44 on tumor cells plays a more significant role in tumor penetration through CD44-mediated transcytosis. A preliminary study was conducted to investigate the regulation of CD44 under conditions involving chemotherapy treatment in tumor cells, as well as its influence on the uptake of CD44-targeting NPs. The study demonstrated that the extracellular domain of the CD44 receptor is susceptible to cleavage upon exposure to chemotherapy drugs, potentially compromising the tumor-targeting efficacy of NPs. The effect of

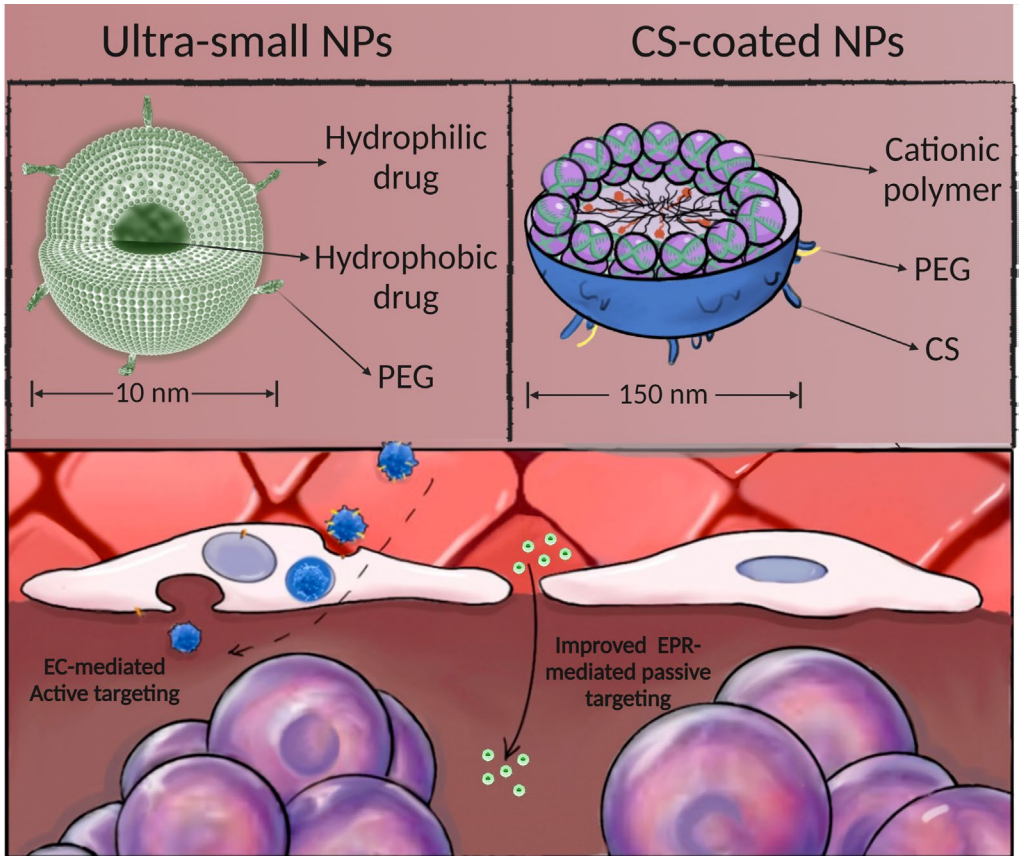

Figure 4-1. Illustration of two strategies in the thesis to improve tumor targeting.

chemotherapy on CD44 cleavage in tumor endothelial cells and its impact on CD44-mediated transcytosis in tumor endothelial cells has not been determined. Further investigation is necessary to clarify the comprehensive impact of chemotherapy drugs on CD44 in both tumor cells and tumor endothelial cells.

With decades of development in targeted delivery to tumors, the interaction between NPs-based drug delivery systems and the physiological environment is now understood to be dynamic rather than static. The efficiency of targeted delivery is dynamic and can be susceptible to influence by physiological or pathological conditions, cancer development, and the status of chemotherapy or immunotherapy. Recent research has indicated that the distribution profiles of NPs may be

influenced by the individual's obesity status, potentially through the modulation of lipoprotein levels on the protein corona [218]. Furthermore, our study and other research demonstrate that the efficiency of nanoparticle targeting can be affected by drug treatment, inflammation, or tumor mutation.

The rapid advancement of technology, such as spatiotemporal single-cell RNA sequencing and cytometry by Time-Of-Flight (CyTOF), necessitates further investigation into the dynamic process of NPs targeting. Moreover, a more precise animal model, such as PDX mouse model or humanized mouse model that can replicate physiologic condition of human tumor, shall boost our understanding of NPs tumor targeting during disease progression in the future.

Bibliography

[1] Y. Matsumura, H. Maeda, A new concept for macromolecular therapeutics in cancer chemotherapy: mechanism of tumoritropic accumulation of proteins and the antitumor agent smancs, Cancer Res 46(12 Pt 1) (1986) 6387-92.
[2] W.L. Monsky, D. Fukumura, T. Gohongi, M. Ancukiewcz, H.A. Weich, V.P. Torchilin, F. Yuan, R.K. Jain, Augmentation of transvascular transport of macromolecules and nanoparticles in tumors using vascular endothelial growth factor, Cancer Res 59(16) (1999) 4129-35.
[3] H. He, L. Liu, E.E. Morin, M. Liu, A. Schwendeman, Survey of Clinical Translation of Cancer Nanomedicines-Lessons Learned from Successes and Failures, Acc Chem Res 52(9) (2019) 2445-2461.
[4] L. Salvioni, M.A. Rizzuto, J.A. Bertolini, L. Pandolfi, M. Colombo, D. Prosperi, Thirty Years of Cancer Nanomedicine: Success, Frustration, and Hope, Cancers 11(12) (2019) 1855.
[5] S. Wilhelm, A.J. Tavares, Q. Dai, S. Ohta, J. Audet, H.F. Dvorak, W.C.W. Chan, Analysis of nanoparticle delivery to tumours, Nature Reviews Materials 1(5) (2016) 16014.
[6] G.H. Petersen, S.K. Alzghari, W. Chee, S.S. Sankari, N.M. La-Beck, Meta-analysis of clinical and preclinical studies comparing the anticancer efficacy of liposomal versus conventional non-liposomal doxorubicin, J Control Release 232 (2016) 255-64.
[7] H. Yang, Z. Tong, S. Sun, Z. Mao, Enhancement of tumour penetration by nanomedicines through strategies based on transport processes and barriers, J Control Release 328 (2020) 28-44.
[8] P.V. Hauser, H.-M. Chang, N. Yanagawa, M. Hamon, Nanotechnology, Nanomedicine, and the Kidney, Applied Sciences 11(16) (2021) 7187.
[9] Y. Shi, R. van der Meel, X. Chen, T. Lammers, The EPR effect and beyond: Strategies to improve tumor targeting and cancer nanomedicine treatment efficacy, Theranostics 10(17) (2020) 7921-7924.
[10] D. Huang, L. Sun, L. Huang, Y. Chen, Nanodrug Delivery Systems Modulate Tumor Vessels to Increase the Enhanced Permeability and Retention Effect, J Pers Med 11(2) (2021).
[11] K. Hori, M. Suzuki, S. Tanda, S. Saito, M. Shinozaki, Q.H. Zhang, Fluctuations in tumor blood flow under normotension and the effect of angiotensin II-induced hypertension, Jpn J Cancer Res 82(11) (1991) 1309-16.
[12] G. Bergers, S. Song, The role of pericytes in blood-vessel formation and maintenance, Neuro Oncol 7(4) (2005) 452-64.
[13] D.W. Siemann, The unique characteristics of tumor vasculature and preclinical evidence for its selective disruption by Tumor-Vascular Disrupting Agents, Cancer Treat Rev 37(1) (2011) 63-74.
[14] R.K. Jain, R.T. Tong, L.L. Munn, Effect of vascular normalization by antiangiogenic therapy on interstitial hypertension, peritumor edema, and lymphatic metastasis: insights from a mathematical model, Cancer Res 67(6) (2007) 2729-35.
[15] R.K. Jain, T. Stylianopoulos, Delivering nanomedicine to solid tumors, Nat Rev Clin Oncol 7(11) (2010) 653-64.
[16] B. Ferrara, C. Pignatelli, M. Cossutta, A. Citro, J. Courty, L. Piemonti, The Extracellular Matrix in Pancreatic Cancer: Description of a Complex Network and Promising Therapeutic Options, Cancers (Basel) 13(17) (2021).

[17] X. He, Y. Yang, Y. Han, C. Cao, Z. Zhang, L. Li, C. Xiao, H. Guo, L. Wang, L. Han, Z. Qu, N. Liu, S. Han, F. Xu, Extracellular matrix physical properties govern the diffusion of nanoparticles in tumor microenvironment, Proceedings of the National Academy of Sciences 120(1) (2023) e2209260120.
[18] M. Zhang, J.J. Ye, Y. Xia, Z.Y. Wang, C.X. Li, X.S. Wang, W. Yu, W. Song, J. Feng, X.Z. Zhang, Platelet-Mimicking Biotaxis Targeting Vasculature-Disrupted Tumors for Cascade Amplification of Hypoxia-Sensitive Therapy, ACS Nano 13(12) (2019) 14230-14240.
[19] S. Sengupta, D. Eavarone, I. Capila, G. Zhao, N. Watson, T. Kiziltepe, R. Sasisekharan, Temporal targeting of tumour cells and neovasculature with a nanoscale delivery system, Nature 436(7050) (2005) 568-72.
[20] M.I. Koukourakis, S. Koukouraki, A. Giatromanolaki, S. Kakolyris, V. Georgoulias, A. Velidaki, S. Archimandritis, N.N. Karkavitsas, High intratumoral accumulation of stealth liposomal doxorubicin in sarcomas--rationale for combination with radiotherapy, Acta Oncol 39(2) (2000) 207-11.
[21] H. Cabral, Y. Matsumoto, K. Mizuno, Q. Chen, M. Murakami, M. Kimura, Y. Terada, M.R. Kano, K. Miyazono, M. Uesaka, N. Nishiyama, K. Kataoka, Accumulation of sub-100 nm polymeric micelles in poorly permeable tumours depends on size, Nat Nanotechnol 6(12) (2011) 815-23.
[22] M. Suzuki, K. Hori, I. Abe, S. Saito, H. Sato, A new approach to cancer chemotherapy: selective enhancement of tumor blood flow with angiotensin II, J Natl Cancer Inst 67(3) (1981) 663-9.
[23] A. Nagamitsu, K. Greish, H. Maeda, Elevating blood pressure as a strategy to increase tumor-targeted delivery of macromolecular drug SMANCS: cases of advanced solid tumors, Jpn J Clin Oncol 39(11) (2009) 756-66.
[24] R.P. Dings, M. Loren, H. Heun, E. McNiel, A.W. Griffioen, K.H. Mayo, R.J. Griffin, Scheduling of radiation with angiogenesis inhibitors anginex and Avastin improves therapeutic outcome via vessel normalization, Clinical cancer research : an official journal of the American Association for Cancer Research 13(11) (2007) 3395-402.
[25] V.P. Chauhan, T. Stylianopoulos, J.D. Martin, Z. Popović, O. Chen, W.S. Kamoun, M.G. Bawendi, D. Fukumura, R.K. Jain, Normalization of tumour blood vessels improves the delivery of nanomedicines in a size-dependent manner, Nat Nanotechnol 7(6) (2012) 383-8.
[26] T. Stylianopoulos, J.D. Martin, V.P. Chauhan, S.R. Jain, B. Diop-Frimpong, N. Bardeesy, B.L. Smith, C.R. Ferrone, F.J. Hornicek, Y. Boucher, L.L. Munn, R.K. Jain, Causes, consequences, and remedies for growth-induced solid stress in murine and human tumors, Proc Natl Acad Sci U S A 109(38) (2012) 15101-8.
[27] P. Baluk, S. Morikawa, A. Haskell, M. Mancuso, D.M. McDonald, Abnormalities of basement membrane on blood vessels and endothelial sprouts in tumors, Am J Pathol 163(5) (2003) 1801-15.
[28] Q. Wang, Q. Liang, J. Dou, H. Zhou, C. Zeng, H. Pan, Y. Shen, Q. Li, Y. Liu, D.T. Leong, W. Jiang, Y. Wang, Breaking through the basement membrane barrier to improve nanotherapeutic delivery to tumours, Nat Nanotechnol (2023).
[29] B. Zhang, K. Jin, T. Jiang, L. Wang, S. Shen, Z. Luo, Y. Tuo, X. Liu, Y. Hu, Z. Pang, Celecoxib normalizes the tumor microenvironment and enhances small nanotherapeutics delivery to A549 tumors in nude mice, Sci Rep 7(1) (2017) 10071.
[30] M.C. Lampi, C.A. Reinhart-King, Targeting extracellular matrix stiffness to attenuate disease: From molecular mechanisms to clinical trials, Sci Transl Med 10(422) (2018).

[31] V.P. Chauhan, R.K. Jain, Strategies for advancing cancer nanomedicine, Nat Mater 12(11) (2013) 958-62.
[32] X. Cun, S. Ruan, J. Chen, L. Zhang, J. Li, Q. He, H. Gao, A dual strategy to improve the penetration and treatment of breast cancer by combining shrinking nanoparticles with collagen depletion by losartan, Acta Biomater 31 (2016) 186-196.
[33] X. Wang, J. Luo, L. He, X. Cheng, G. Yan, J. Wang, R. Tang, Hybrid pH-sensitive nanogels surface-functionalized with collagenase for enhanced tumor penetration, J Colloid Interface Sci 525 (2018) 269-281.
[34] D. Zhang, G. Wang, X. Yu, T. Wei, L. Farbiak, L.T. Johnson, A.M. Taylor, J. Xu, Y. Hong, H. Zhu, D.J. Siegwart, Enhancing CRISPR/Cas gene editing through modulating cellular mechanical properties for cancer therapy, Nat Nanotechnol 17(7) (2022) 777-787.
[35] S. Sindhwani, A.M. Syed, J. Ngai, B.R. Kingston, L. Maiorino, J. Rothschild, P. MacMillan, Y. Zhang, N.U. Rajesh, T. Hoang, J.L.Y. Wu, S. Wilhelm, A. Zilman, S. Gadde, A. Sulaiman, B. Ouyang, Z. Lin, L. Wang, M. Egeblad, W.C.W. Chan, The entry of nanoparticles into solid tumours, Nat Mater 19(5) (2020) 566-575.
[36] M. Hama, Y. Ishima, V.T.G. Chuang, H. Ando, T. Shimizu, T. Ishida, Evidence for Delivery of Abraxane via a Denatured-Albumin Transport System, ACS Appl Mater Interfaces 13(17) (2021) 19736-19744.
[37] D. Feng, J.A. Nagy, H.F. Dvorak, A.M. Dvorak, Ultrastructural studies define soluble macromolecular, particulate, and cellular transendothelial cell pathways in venules, lymphatic vessels, and tumor-associated microvessels in man and animals, Microsc Res Tech 57(5) (2002) 289-326.
[38] M. Barczyk, S. Carracedo, D. Gullberg, Integrins, Cell Tissue Res 339(1) (2010) 269-80.
[39] B.P. Eliceiri, D.A. Cheresh, Role of alpha v integrins during angiogenesis, Cancer J 6 Suppl 3 (2000) S245-9.
[40] M. Amin, M. Mansourian, G.A. Koning, A. Badiee, M.R. Jaafari, T.L.M. Ten Hagen, Development of a novel cyclic RGD peptide for multiple targeting approaches of liposomes to tumor region, J Control Release 220(Pt A) (2015) 308-315.
[41] N. Li, S. Qiu, Y. Fang, J. Wu, Q. Li, Comparison of Linear vs. Cyclic RGD Pentapeptide Interactions with Integrin α(v)β(3) by Molecular Dynamics Simulations, Biology (Basel) 10(7) (2021).
[42] J. Li, X. Zhang, M. Wang, X. Li, H. Mu, A. Wang, W. Liu, Y. Li, Z. Wu, K. Sun, Synthesis of a bi-functional dendrimer-based nanovehicle co-modified with RGDyC and TAT peptides for neovascular targeting and penetration, Int J Pharm 501(1-2) (2016) 112-23.
[43] Y. Lu, S. Han, H. Zheng, R. Ma, Y. Ping, J. Zou, H. Tang, Y. Zhang, X. Xu, F. Li, A novel RGDyC/PEG co-modified PAMAM dendrimer-loaded arsenic trioxide of glioma targeting delivery system, Int J Nanomedicine 13 (2018) 5937-5952.
[44] Y. Wang, L. Tong, J. Wang, J. Luo, J. Tang, L. Zhong, Q. Xiao, W. Niu, J. Li, J. Zhu, H. Chen, X. Li, Y. Wang, cRGD-functionalized nanoparticles for combination therapy of anti-endothelium dependent vessels and anti-vasculogenic mimicry to inhibit the proliferation of ovarian cancer, Acta Biomater 94 (2019) 495-504.
[45] K.N. Sugahara, T. Teesalu, P.P. Karmali, V.R. Kotamraju, L. Agemy, O.M. Girard, D. Hanahan, R.F. Mattrey, E. Ruoslahti, Tissue-penetrating delivery of compounds and nanoparticles into tumors, Cancer Cell 16(6) (2009) 510-20.

[46] X. Liu, P. Lin, I. Perrett, J. Lin, Y.P. Liao, C.H. Chang, J. Jiang, N. Wu, T. Donahue, Z. Wainberg, A.E. Nel, H. Meng, Tumor-penetrating peptide enhances transcytosis of silicasome-based chemotherapy for pancreatic cancer, J Clin Invest 127(5) (2017) 2007-2018.
[47] X. Liu, J. Jiang, Y. Ji, J. Lu, R. Chan, H. Meng, Targeted drug delivery using iRGD peptide for solid cancer treatment, Mol Syst Des Eng 2(4) (2017) 370-379.
[48] J.O. Martinez, M. Evangelopoulos, V. Karun, E. Shegog, J.A. Wang, C. Boada, X. Liu, M. Ferrari, E. Tasciotti, The effect of multistage nanovector targeting of VEGFR2 positive tumor endothelia on cell adhesion and local payload accumulation, Biomaterials 35(37) (2014) 9824-9832.
[49] A. Orleth, C. Mamot, C. Rochlitz, R. Ritschard, K. Alitalo, G. Christofori, A. Wicki, Simultaneous targeting of VEGF-receptors 2 and 3 with immunoliposomes enhances therapeutic efficacy, Journal of drug targeting 24(1) (2016) 80-9.
[50] P. Guo, J. Huang, L. Wang, D. Jia, J. Yang, D.A. Dillon, D. Zurakowski, H. Mao, M.A. Moses, D.T. Auguste, ICAM-1 as a molecular target for triple negative breast cancer, Proc Natl Acad Sci U S A 111(41) (2014) 14710-5.
[51] P. Guo, J. Yang, D. Jia, M.A. Moses, D.T. Auguste, ICAM-1-Targeted, Lcn2 siRNA-Encapsulating Liposomes are Potent Anti-angiogenic Agents for Triple Negative Breast Cancer, Theranostics 6(1) (2016) 1-13.
[52] L.T. Senbanjo, M.A. Chellaiah, CD44: A Multifunctional Cell Surface Adhesion Receptor Is a Regulator of Progression and Metastasis of Cancer Cells, Front Cell Dev Biol 5 (2017) 18.
[53] G. Cao, R.C. Savani, M. Fehrenbach, C. Lyons, L. Zhang, G. Coukos, H.M. Delisser, Involvement of endothelial CD44 during in vivo angiogenesis, Am J Pathol 169(1) (2006) 325-36.
[54] E.J. Oh, K. Park, K.S. Kim, J. Kim, J.A. Yang, J.H. Kong, M.Y. Lee, A.S. Hoffman, S.K. Hahn, Target specific and long-acting delivery of protein, peptide, and nucleotide therapeutics using hyaluronic acid derivatives, J Control Release 141(1) (2010) 2-12.
[55] A.K. Yadav, P. Mishra, A.K. Mishra, P. Mishra, S. Jain, G.P. Agrawal, Development and characterization of hyaluronic acid-anchored PLGA nanoparticulate carriers of doxorubicin, Nanomedicine 3(4) (2007) 246-57.
[56] J. Li, M. Huo, J. Wang, J. Zhou, J.M. Mohammad, Y. Zhang, Q. Zhu, A.Y. Waddad, Q. Zhang, Redox-sensitive micelles self-assembled from amphiphilic hyaluronic acid-deoxycholic acid conjugates for targeted intracellular delivery of paclitaxel, Biomaterials 33(7) (2012) 2310-20.
[57] K.Y. Choi, H. Chung, K.H. Min, H.Y. Yoon, K. Kim, J.H. Park, I.C. Kwon, S.Y. Jeong, Self-assembled hyaluronic acid nanoparticles for active tumor targeting, Biomaterials 31(1) (2010) 106-14.
[58] W. Chen, Y. Liu, X. Liang, Y. Huang, Q. Li, Chondroitin sulfate-functionalized polyamidoamine as a tumor-targeted carrier for miR-34a delivery, Acta Biomater 57 (2017) 238-250.
[59] Y. Pan, Y. Zhang, H. Ouyang, T. Gong, Z. Zhang, X. Cao, Y. Fu, Targeted Delivery of Celastrol via Chondroitin Sulfate Derived Hybrid Micelles for Alleviating Symptoms in Nonalcoholic Fatty Liver Disease, ACS Appl Bio Mater (2023).
[60] Y. Xie, W. Xu, Z. Jin, K. Zhao, Chondroitin sulfate functionalized palmitic acid and cysteine cografted-quaternized chitosan for CD44 and gut microbiota dual-targeted delivery of curcumin, Mater Today Bio 20 (2023) 100617.
[61] G.S. Kansas, Selectins and their ligands: current concepts and controversies, Blood 88(9) (1996) 3259-87.

[62] H. Läubli, L. Borsig, Selectins promote tumor metastasis, Semin Cancer Biol 20(3) (2010) 169-77.
[63] L. Gong, H.J. Mi, H. Zhu, X. Zhou, H. Yang, P-selectin-mediated platelet activation promotes adhesion of non-small cell lung carcinoma cells on vascular endothelial cells under flow, Mol Med Rep 5(4) (2012) 935-42.
[64] S.P. Gunningham, M.J. Currie, H.R. Morrin, E.Y. Tan, H. Turley, G.U. Dachs, A.I. Watson, C. Frampton, B.A. Robinson, S.B. Fox, The angiogenic factor thymidine phosphorylase up-regulates the cell adhesion molecule P-selectin in human vascular endothelial cells and is associated with P-selectin expression in breast cancers, J Pathol 212(3) (2007) 335-44.
[65] B. Hemmerlein, J. Scherbening, A. Kugler, H.J. Radzun, Expression of VCAM-1, ICAM-1, E- and P-selectin and tumour-associated macrophages in renal cell carcinoma, Histopathology 37(1) (2000) 78-83.
[66] Y. Shamay, M. Elkabets, H. Li, J. Shah, S. Brook, F. Wang, K. Adler, E. Baut, M. Scaltriti, P.V. Jena, E.E. Gardner, J.T. Poirier, C.M. Rudin, J. Baselga, A. Haimovitz-Friedman, D.A. Heller, P-selectin is a nanotherapeutic delivery target in the tumor microenvironment, Sci Transl Med 8(345) (2016) 345ra87.
[67] D.E. Tylawsky, H. Kiguchi, J. Vaynshteyn, J. Gerwin, J. Shah, T. Islam, J.A. Boyer, D.R. Boué, M. Snuderl, M.B. Greenblatt, Y. Shamay, G.P. Raju, D.A. Heller, P-selectin-targeted nanocarriers induce active crossing of the blood-brain barrier via caveolin-1-dependent transcytosis, Nat Mater 22(3) (2023) 391-399.
[68] G. Thurston, J.W. McLean, M. Rizen, P. Baluk, A. Haskell, T.J. Murphy, D. Hanahan, D.M. McDonald, Cationic liposomes target angiogenic endothelial cells in tumors and chronic inflammation in mice, J Clin Invest 101(7) (1998) 1401-13.
[69] A. Santel, M. Aleku, O. Keil, J. Endruschat, V. Esche, G. Fisch, S. Dames, K. Löffler, M. Fechtner, W. Arnold, K. Giese, A. Klippel, J. Kaufmann, A novel siRNA-lipoplex technology for RNA interference in the mouse vascular endothelium, Gene Ther 13(16) (2006) 1222-34.
[70] V. Fehring, U. Schaeper, K. Ahrens, A. Santel, O. Keil, M. Eisermann, K. Giese, J. Kaufmann, Delivery of therapeutic siRNA to the lung endothelium via novel Lipoplex formulation DACC, Mol Ther 22(4) (2014) 811-20.
[71] Q. Zhou, S. Shao, J. Wang, C. Xu, J. Xiang, Y. Piao, Z. Zhou, Q. Yu, J. Tang, X. Liu, Z. Gan, R. Mo, Z. Gu, Y. Shen, Enzyme-activatable polymer-drug conjugate augments tumour penetration and treatment efficacy, Nat Nanotechnol 14(8) (2019) 799-809.
[72] Y. Chen, Y. Huang, Q. Li, Z. Luo, Z. Zhang, H. Huang, J. Sun, L. Zhang, R. Sun, D.J. Bain, J.F. Conway, B. Lu, S. Li, Targeting Xkr8 via nanoparticle-mediated in situ co-delivery of siRNA and chemotherapy drugs for cancer immunochemotherapy, Nat Nanotechnol (2022).
[73] M. Kreuter, M. Steins, K. Woelke, T. Buechner, W.E. Berdel, R.M. Mesters, Downregulation of neuropilin-1 in patients with acute myeloid leukemia treated with thalidomide, Eur J Haematol 79(5) (2007) 392-7.
[74] J. Li, Y. Ai, L. Wang, P. Bu, C.C. Sharkey, Q. Wu, B. Wun, S. Roy, X. Shen, M.R. King, Targeted drug delivery to circulating tumor cells via platelet membrane-functionalized particles, Biomaterials 76 (2016) 52-65.
[75] Q. Hu, W. Sun, C. Qian, C. Wang, H.N. Bomba, Z. Gu, Anticancer Platelet-Mimicking Nanovehicles, Adv Mater 27(44) (2015) 7043-50.
[76] A. Parodi, N. Quattrocchi, A.L. van de Ven, C. Chiappini, M. Evangelopoulos, J.O. Martinez, B.S. Brown, S.Z. Khaled, I.K. Yazdi, M.V. Enzo, L. Isenhart, M. Ferrari, E. Tasciotti, Synthetic

nanoparticles functionalized with biomimetic leukocyte membranes possess cell-like functions, Nat Nanotechnol 8(1) (2013) 61-8.
[77] S. Krishnamurthy, M.K. Gnanasammandhan, C. Xie, K. Huang, M.Y. Cui, J.M. Chan, Monocyte cell membrane-derived nanoghosts for targeted cancer therapy, Nanoscale 8(13) (2016) 6981-5.
[78] T. Kang, Q. Zhu, D. Wei, J. Feng, J. Yao, T. Jiang, Q. Song, X. Wei, H. Chen, X. Gao, J. Chen, Nanoparticles Coated with Neutrophil Membranes Can Effectively Treat Cancer Metastasis, ACS Nano 11(2) (2017) 1397-1411.
[79] L. Zhang, R. Li, H. Chen, J. Wei, H. Qian, S. Su, J. Shao, L. Wang, X. Qian, B. Liu, Human cytotoxic T-lymphocyte membrane-camouflaged nanoparticles combined with low-dose irradiation: a new approach to enhance drug targeting in gastric cancer, Int J Nanomedicine 12 (2017) 2129-2142.
[80] T. Gwisai, N. Mirkhani, M.G. Christiansen, T.T. Nguyen, V. Ling, S. Schuerle, Magnetic torque-driven living microrobots for increased tumor infiltration, Sci Robot 7(71) (2022) eabo0665.
[81] T. Harimoto, J. Hahn, Y.Y. Chen, J. Im, J. Zhang, N. Hou, F. Li, C. Coker, K. Gray, N. Harr, S. Chowdhury, K. Pu, C. Nimura, N. Arpaia, K.W. Leong, T. Danino, A programmable encapsulation system improves delivery of therapeutic bacteria in mice, Nat Biotechnol 40(8) (2022) 1259-1269.
[82] A.R. Chaudhuri, A. Nussenzweig, The multifaceted roles of PARP1 in DNA repair and chromatin remodelling, Nature reviews Molecular cell biology 18(10) (2017) 610-621.
[83] P. Caiafa, Parp and epigenetic regulation, Poly (ADP-Ribosyl) ation, Springer2006, pp. 91-102.
[84] Y. Shen, F.L. Rehman, Y. Feng, J. Boshuizen, I. Bajrami, R. Elliott, B. Wang, C.J. Lord, L.E. Post, A. Ashworth, BMN 673, a novel and highly potent PARP1/2 inhibitor for the treatment of human cancers with DNA repair deficiency, Clinical Cancer Research 19(18) (2013) 5003-5015.
[85] W. Zhang, J. Xu, DNA methyltransferases and their roles in tumorigenesis, Biomarker research 5(1) (2017) 1-8.
[86] K.J. Dedes, P.M. Wilkerson, D. Wetterskog, B. Weigelt, A. Ashworth, J.S. Reis-Filho, Synthetic lethality of PARP inhibition in cancers lacking BRCA1 and BRCA2 mutations, Cell cycle 10(8) (2011) 1192-1199.
[87] A.P. Wiegmans, P.-Y. Yap, A. Ward, Y.C. Lim, K.K. Khanna, Differences in expression of key DNA damage repair genes after epigenetic-induced BRCAness dictate synthetic lethality with PARP1 inhibition, Molecular cancer therapeutics 14(10) (2015) 2321-2331.
[88] S. Karakashev, T. Fukumoto, B. Zhao, J. Lin, S. Wu, N. Fatkhutdinov, P.-H. Park, G. Semenova, S. Jean, M.G. Cadungog, EZH2 inhibition sensitizes CARM1-high, homologous recombination proficient ovarian cancers to PARP inhibition, Cancer Cell 37(2) (2020) 157-167. e6.
[89] N.E. Muvarak, K. Chowdhury, L. Xia, C. Robert, E.Y. Choi, Y. Cai, M. Bellani, Y. Zou, Z.N. Singh, V.H. Duong, Enhancing the cytotoxic effects of PARP inhibitors with DNA demethylating agents–a potential therapy for cancer, Cancer cell 30(4) (2016) 637-650.
[90] M.A.T.M. van Vugt, E.E. Parkes, When breaks get hot: inflammatory signaling in BRCA1/2-mutant cancers, Trends in Cancer.
[91] Y.L. Liu, P. Selenica, Q. Zhou, A. Iasonos, M. Callahan, N.Z. Feit, J. Boland, I. Vazquez-Garcia, D. Mandelker, A. Zehir, R.A. Burger, D.J. Powell, C. Friedman, K. Cadoo, R. Grisham, J.A. Konner, R.E. O'Cearbhaill, C. Aghajanian, J.S. Reis-Filho, B. Weigelt, D. Zamarin, BRCA

Mutations, Homologous DNA Repair Deficiency, Tumor Mutational Burden, and Response to Immune Checkpoint Inhibition in Recurrent Ovarian Cancer, JCO Precision Oncology (4) (2020) 665-679.
[92] S. Kakoti, H. Sato, S. Laskar, T. Yasuhara, A. Shibata, DNA Repair and Signaling in Immune-Related Cancer Therapy, Front Mol Biosci 7 (2020) 205-205.
[93] N. Luo, M.J. Nixon, P.I. Gonzalez-Ericsson, V. Sanchez, S.R. Opalenik, H. Li, C.A. Zahnow, M.L. Nickels, F. Liu, M.N. Tantawy, DNA methyltransferase inhibition upregulates MHC-I to potentiate cytotoxic T lymphocyte responses in breast cancer, Nature communications 9(1) (2018) 1-11.
[94] C.B. Yoo, S. Jeong, G. Egger, G. Liang, P. Phiasivongsa, C. Tang, S. Redkar, P.A. Jones, Delivery of 5-aza-2′-deoxycytidine to cells using oligodeoxynucleotides, Cancer Research 67(13) (2007) 6400-6408.
[95] G.G. Eskiler, G. Cecener, U. Egeli, B. Tunca, Synthetically lethal BMN 673 (Talazoparib) loaded solid lipid nanoparticles for BRCA1 mutant triple negative breast cancer, Pharmaceutical research 35(11) (2018) 1-20.
[96] J.E. Belz, R. Kumar, P. Baldwin, N.C. Ojo, A.S. Leal, D.B. Royce, D. Zhang, A.L. van de Ven, K.T. Liby, S. Sridhar, Sustained release talazoparib implants for localized treatment of BRCA1-deficient breast cancer, Theranostics 7(17) (2017) 4340.
[97] B. Brueckner, M. Rius, M.R. Markelova, I. Fichtner, P.-A. Hals, M.L. Sandvold, F. Lyko, Delivery of 5-azacytidine to human cancer cells by elaidic acid esterification increases therapeutic drug efficacy, Molecular cancer therapeutics 9(5) (2010) 1256-1264.
[98] Y. Matsumoto, J.W. Nichols, K. Toh, T. Nomoto, H. Cabral, Y. Miura, R.J. Christie, N. Yamada, T. Ogura, M.R. Kano, Y. Matsumura, N. Nishiyama, T. Yamasoba, Y.H. Bae, K. Kataoka, Vascular bursts enhance permeability of tumour blood vessels and improve nanoparticle delivery, Nature Nanotechnology 11(6) (2016) 533-538.
[99] M. Cooley, A. Sarode, M. Hoore, D.A. Fedosov, S. Mitragotri, A.S. Gupta, Influence of particle size and shape on their margination and wall-adhesion: implications in drug delivery vehicle design across nano-to-micro scale, Nanoscale 10(32) (2018) 15350-15364.
[100] S. Wilhelm, A.J. Tavares, Q. Dai, S. Ohta, J. Audet, H.F. Dvorak, W.C. Chan, Analysis of nanoparticle delivery to tumours, Nature reviews materials 1(5) (2016) 1-12.
[101] S. Sindhwani, A.M. Syed, J. Ngai, B.R. Kingston, L. Maiorino, J. Rothschild, P. MacMillan, Y. Zhang, N.U. Rajesh, T. Hoang, The entry of nanoparticles into solid tumours, Nature materials 19(5) (2020) 566-575.
[102] J. Sun, Y. Chen, K. Li, Y. Huang, X. Fu, X. Zhang, W. Zhao, Y. Wei, L. Xu, P. Zhang, R. Venkataramanan, S. Li, A prodrug micellar carrier assembled from polymers with pendant farnesyl thiosalicylic acid moieties for improved delivery of paclitaxel, Acta Biomaterialia 43 (2016) 282-291.
[103] P. Baldwin, A.W. Ohman, J.E. Medina, E.T. McCarthy, D.M. Dinulescu, S. Sridhar, Nanoformulation of Talazoparib Delays Tumor Progression and Ascites Formation in a Late Stage Cancer Model, Frontiers in Oncology 9 (2019).
[104] D. Dutta, J.G. Donaldson, Search for inhibitors of endocytosis: Intended specificity and unintended consequences, Cell Logist 2(4) (2012) 203-208.
[105] W. Lu, C. Xiong, R. Zhang, L. Shi, M. Huang, G. Zhang, S. Song, Q. Huang, G.-y. Liu, C. Li, Receptor-mediated transcytosis: a mechanism for active extravascular transport of nanoparticles in solid tumors, Journal of controlled release 161(3) (2012) 959-966.

[106] Z. Cong, L. Zhang, S.-Q. Ma, K.S. Lam, F.-F. Yang, Y.-H. Liao, Size-transformable hyaluronan stacked self-assembling peptide nanoparticles for improved transcellular tumor penetration and photo–chemo combination therapy, ACS nano 14(2) (2020) 1958-1970.
[107] V. Justilien, A.P. Fields, Utility and applications of orthotopic models of human non-small cell lung cancer (NSCLC) for the evaluation of novel and emerging cancer therapeutics, Curr Protoc Pharmacol 62 (2013) 14.27.1-14.27.17.
[108] J. Sun, L. Sun, J. Li, J. Xu, Z. Wan, Z. Ouyang, L. Liang, S. Li, D. Zeng, A Multi-Functional Polymeric Carrier for Simultaneous Positron Emission Tomography Imaging and Combination Therapy, Acta Biomaterialia (2018).
[109] A.D. Herbert, A.M. Carr, E. Hoffmann, FindFoci: A Focus Detection Algorithm with Automated Parameter Training That Closely Matches Human Assignments, Reduces Human Inconsistencies and Increases Speed of Analysis, PLOS ONE 9(12) (2014) e114749.
[110] Y. Chen, R. Xia, Y. Huang, W. Zhao, J. Li, X. Zhang, P. Wang, R. Venkataramanan, J. Fan, W. Xie, X. Ma, B. Lu, S. Li, An immunostimulatory dual-functional nanocarrier that improves cancer immunochemotherapy, Nature Communications 7 (2016) 13443-13455.
[111] M. Pertea, D. Kim, G.M. Pertea, J.T. Leek, S.L. Salzberg, Transcript-level expression analysis of RNA-seq experiments with HISAT, StringTie and Ballgown, Nature Protocols 11(9) (2016) 1650-1667.
[112] Y. Wang, Z. Wang, J. Xu, J. Li, S. Li, M. Zhang, D. Yang, Systematic identification of non-coding pharmacogenomic landscape in cancer, Nature communications 9(1) (2018) 1-15.
[113] F. Yuan, M. Leunig, S.K. Huang, D.A. Berk, D. Papahadjopoulos, R.K. Jain, Mirovascular permeability and interstitial penetration of sterically stabilized (stealth) liposomes in a human tumor xenograft, Cancer Research 54(13) (1994) 3352-3356.
[114] A. Shevchenko, H. Tomas, J. Havli, J.V. Olsen, M. Mann, In-gel digestion for mass spectrometric characterization of proteins and proteomes, Nature Protocols 1(6) (2006) 2856-2860.
[115] Y.H. Bae, H. Yin, Stability issues of polymeric micelles, Journal of Controlled Release 131(1) (2008) 2-4.
[116] H. Chen, S. Kim, W. He, H. Wang, P.S. Low, K. Park, J.-X. Cheng, Fast release of lipophilic agents from circulating PEG-PDLLA micelles revealed by in vivo forster resonance energy transfer imaging, Langmuir 24(10) (2008) 5213-5217.
[117] A. Schulz, S. Jaksch, R. Schubel, E. Wegener, Z. Di, Y. Han, A. Meister, J.r. Kressler, A.V. Kabanov, R. Luxenhofer, Drug-induced morphology switch in drug delivery systems based on poly (2-oxazoline) s, ACS Nano 8(3) (2014) 2686-2696.
[118] A. Reisch, A. Runser, Y. Arntz, Y. Mély, A.S. Klymchenko, Charge-controlled nanoprecipitation as a modular approach to ultrasmall polymer nanocarriers: making bright and stable nanoparticles, ACS Nano 9(5) (2015) 5104-5116.
[119] Y. Wang, B. Li, Y. Zhou, Z. Lu, D. Yan, Dissipative particle dynamics simulation study on the mechanisms of self-assembly of large multimolecular micelles from amphiphilic dendritic multiarm copolymers, Soft Matter 9(12) (2013) 3293-3304.
[120] K.K. Chan, D.D. Giannini, J.A. Staroscik, W. Sadee, 5-Azacytidine hydrolysis kinetics measured by high-pressure liquid chromatography and 13C-NMR spectroscopy, J Pharm Sci 68(7) (1979) 807-12.
[121] W. Ngo, J.L.Y. Wu, Z.P. Lin, Y. Zhang, B. Bussin, A. Granda Farias, A.M. Syed, K. Chan, A. Habsid, J. Moffat, W.C.W. Chan, Identifying cell receptors for the nanoparticle protein corona using genome screens, Nature Chemical Biology 18(9) (2022) 1023-1031.

[122] M. Qiu, Y. Tang, J. Chen, R. Muriph, Z. Ye, C. Huang, J. Evans, E.P. Henske, Q. Xu, Lung-selective mRNA delivery of synthetic lipid nanoparticles for the treatment of pulmonary lymphangioleiomyomatosis, Proceedings of the National Academy of Sciences 119(8) (2022) e2116271119.
[123] Y. Xu, Y. Guo, C. Zhang, M. Zhan, L. Jia, S. Song, C. Jiang, M. Shen, X. Shi, Fibronectin-Coated Metal–Phenolic Networks for Cooperative Tumor Chemo-/Chemodynamic/Immune Therapy via Enhanced Ferroptosis-Mediated Immunogenic Cell Death, ACS Nano 16(1) (2022) 984-996.
[124] M.D. Pierschbacher, E. Ruoslahti, Cell attachment activity of fibronectin can be duplicated by small synthetic fragments of the molecule, Nature 309(5963) (1984) 30-3.
[125] J.L. Sechler, S.A. Corbett, J.E. Schwarzbauer, Modulatory roles for integrin activation and the synergy site of fibronectin during matrix assembly, Molecular biology of the cell 8(12) (1997) 2563-73.
[126] J.P. Issa, H.M. Kantarjian, Targeting DNA methylation, Clinical cancer research : an official journal of the American Association for Cancer Research 15(12) (2009) 3938-46.
[127] A.M. Newman, C.L. Liu, M.R. Green, A.J. Gentles, W. Feng, Y. Xu, C.D. Hoang, M. Diehn, A.A. Alizadeh, Robust enumeration of cell subsets from tissue expression profiles, Nature Methods 12(5) (2015) 453-457.
[128] J. Liang, L. Wang, C. Wang, J. Shen, B. Su, A.L. Marisetty, D. Fang, C. Kassab, K.J. Jeong, W. Zhao, Y. Lu, A.K. Jain, Z. Zhou, H. Liang, S.-C. Sun, C. Lu, Z.-X. Xu, Q. Yu, S. Shao, X. Chen, M. Gao, F.X. Claret, Z. Ding, J. Chen, P. Chen, M.C. Barton, G. Peng, G.B. Mills, A.B. Heimberger, Verteporfin Inhibits PD-L1 through Autophagy and the STAT1–IRF1–TRIM28 Signaling Axis, Exerting Antitumor Efficacy, Cancer Immunology Research 8(7) (2020) 952.
[129] A.M. Zeidan, J. Cavenagh, M.T. Voso, D. Taussig, M. Tormo, I. Boss, W.B. Copeland, V.E. Gray, A. Previtali, T. O'Connor, S. Rose, C.L. Beach, L.R. Silverman, Efficacy and Safety of Azacitidine (AZA) in Combination with the Anti-PD-L1 Durvalumab (durva) for the Front-Line Treatment of Older Patients (pts) with Acute Myeloid Leukemia (AML) Who Are Unfit for Intensive Chemotherapy (IC) and Pts with Higher-Risk Myelodysplastic Syndromes (HR-MDS): Results from a Large, International, Randomized Phase 2 Study, Blood 134(Supplement_1) (2019) 829-829.
[130] R.M. Chabanon, G. Muirhead, D.B. Krastev, J. Adam, D. Morel, M. Garrido, A. Lamb, C. Hénon, N. Dorvault, M. Rouanne, R. Marlow, I. Bajrami, M.L. Cardeñosa, A. Konde, B. Besse, A. Ashworth, S.J. Pettitt, S. Haider, A. Marabelle, A.N.J. Tutt, J.-C. Soria, C.J. Lord, S. Postel-Vinay, PARP inhibition enhances tumor cell–intrinsic immunity in ERCC1-deficient non–small cell lung cancer, The Journal of Clinical Investigation 129(3) (2019) 1211-1228.
[131] T. Stylianopoulos, E.-A. Economides, J.W. Baish, D. Fukumura, R.K. Jain, Towards Optimal Design of Cancer Nanomedicines: Multi-stage Nanoparticles for the Treatment of Solid Tumors, Annals of Biomedical Engineering 43(9) (2015) 2291-2300.
[132] K. Huang, H. Ma, J. Liu, S. Huo, A. Kumar, T. Wei, X. Zhang, S. Jin, Y. Gan, P.C. Wang, S. He, X. Zhang, X.-J. Liang, Size-Dependent Localization and Penetration of Ultrasmall Gold Nanoparticles in Cancer Cells, Multicellular Spheroids, and Tumors in Vivo, ACS Nano 6(5) (2012) 4483-4493.
[133] Z. Wan, H. Huang, R.E. West Iii, M. Zhang, B. Zhang, X. Cai, Z. Zhang, Z. Luo, Y. Chen, Y. Zhang, W. Xie, D. Yang, T.D. Nolin, J. Wang, S. Li, J. Sun, Overcoming pancreatic cancer immune resistance by codelivery of CCR2 antagonist using a STING-activating gemcitabine-based nanocarrier, Materials Today 62 (2023) 33-50.

[134] J. Xu, M. Song, Z. Fang, L. Zheng, X. Huang, K. Liu, Applications and challenges of ultra-small particle size nanoparticles in tumor therapy, Journal of Controlled Release 353 (2023) 699-712.
[135] Q. Zhou, S. Shao, J. Wang, C. Xu, J. Xiang, Y. Piao, Z. Zhou, Q. Yu, J. Tang, X. Liu, Z. Gan, R. Mo, Z. Gu, Y. Shen, Enzyme-activatable polymer–drug conjugate augments tumour penetration and treatment efficacy, Nature Nanotechnology 14(8) (2019) 799-809.
[136] Y. Chen, Y. Huang, Q. Li, Z. Luo, Z. Zhang, H. Huang, J. Sun, L. Zhang, R. Sun, D.J. Bain, J.F. Conway, B. Lu, S. Li, Targeting Xkr8 via nanoparticle-mediated in situ co-delivery of siRNA and chemotherapy drugs for cancer immunochemotherapy, Nat Nanotechnol 18(2) (2023) 193-204.
[137] M. Mahmoudi, M.P. Landry, A. Moore, R. Coreas, The protein corona from nanomedicine to environmental science, Nature Reviews Materials 8(7) (2023) 422-438.
[138] X. Wang, M. Wang, R. Lei, S.F. Zhu, Y. Zhao, C. Chen, Chiral Surface of Nanoparticles Determines the Orientation of Adsorbed Transferrin and Its Interaction with Receptors, ACS Nano 11(5) (2017) 4606-4616.
[139] V. Mirshafiee, R. Kim, S. Park, M. Mahmoudi, M.L. Kraft, Impact of protein pre-coating on the protein corona composition and nanoparticle cellular uptake, Biomaterials 75 (2016) 295-304.
[140] M. Qiu, Y. Tang, J. Chen, R. Muriph, Z. Ye, C. Huang, J. Evans, E.P. Henske, Q. Xu, Lung-selective mRNA delivery of synthetic lipid nanoparticles for the treatment of pulmonary lymphangioleiomyomatosis, Proc Natl Acad Sci U S A 119(8) (2022).
[141] D. Plana, A.C. Palmer, P.K. Sorger, Independent Drug Action in Combination Therapy: Implications for Precision Oncology, Cancer Discovery 12(3) (2022) 606-624.
[142] W. Fan, B. Yung, P. Huang, X. Chen, Nanotechnology for Multimodal Synergistic Cancer Therapy, Chem Rev 117(22) (2017) 13566-13638.
[143] A. Cercek, M. Lumish, J. Sinopoli, J. Weiss, J. Shia, M. Lamendola-Essel, I.H. El Dika, N. Segal, M. Shcherba, R. Sugarman, Z. Stadler, R. Yaeger, J.J. Smith, B. Rousseau, G. Argiles, M. Patel, A. Desai, L.B. Saltz, M. Widmar, K. Iyer, J. Zhang, N. Gianino, C. Crane, P.B. Romesser, E.P. Pappou, P. Paty, J. Garcia-Aguilar, M. Gonen, M. Gollub, M.R. Weiser, K.A. Schalper, L.A. Diaz, PD-1 Blockade in Mismatch Repair–Deficient, Locally Advanced Rectal Cancer, New England Journal of Medicine 386(25) (2022) 2363-2376.
[144] M. Freeman, The Rhomboid-Like Superfamily: Molecular Mechanisms and Biological Roles, Annual Review of Cell and Developmental Biology 30(1) (2014) 235-254.
[145] M. Freeman, Rhomboid Proteases and their Biological Functions, Annual Review of Genetics 42(1) (2008) 191-210.
[146] M. Zettl, C. Adrain, K. Strisovsky, V. Lastun, M. Freeman, Rhomboid family pseudoproteases use the ER quality control machinery to regulate intercellular signaling, Cell 145(1) (2011) 79-91.
[147] W.-W. Luo, S. Li, C. Li, H. Lian, Q. Yang, B. Zhong, H.-B. Shu, iRhom2 is essential for innate immunity to DNA viruses by mediating trafficking and stability of the adaptor STING, Nature Immunology 17 (2016) 1057.
[148] M. Cavadas, I. Oikonomidi, C.J. Gaspar, E. Burbridge, M. Badenes, I. Félix, A. Bolado, T. Hu, A. Bileck, C. Gerner, P.M. Domingos, A. von Kriegsheim, C. Adrain, Phosphorylation of iRhom2 Controls Stimulated Proteolytic Shedding by the Metalloprotease ADAM17/TACE, Cell Rep 21(3) (2017) 745-757.

[149] C. Adrain, M. Zettl, Y. Christova, N. Taylor, M. Freeman, Tumor Necrosis Factor Signaling Requires iRhom2 to Promote Trafficking and Activation of TACE, Science 335(6065) (2012) 225-228.
[150] R. Ji, Q. Shi, Y. Cao, J. Zhang, C. Zhao, H. Zhao, Y. Sayyed, L. Fu, L.-Y. Li, Alternative splicing of the human rhomboid family-1 gene RHBDF1 inhibits epidermal growth factor receptor activation, Journal of Biological Chemistry 298(6) (2022) 102033.
[151] X. Li, T. Maretzky, G. Weskamp, S. Monette, X. Qing, P.D.A. Issuree, H.C. Crawford, D.R. McIlwain, T.W. Mak, J.E. Salmon, C.P. Blobel, iRhoms 1 and 2 are essential upstream regulators of ADAM17-dependent EGFR signaling, Proceedings of the National Academy of Sciences 112(19) (2015) 6080.
[152] D.R. McIlwain, P.A. Lang, T. Maretzky, K. Hamada, K. Ohishi, S.K. Maney, T. Berger, A. Murthy, G. Duncan, H.C. Xu, K.S. Lang, D. Häussinger, A. Wakeham, A. Itie-Youten, R. Khokha, P.S. Ohashi, C.P. Blobel, T.W. Mak, iRhom2 regulation of TACE controls TNF-mediated protection against Listeria and responses to LPS, Science 335(6065) (2012) 229-32.
[153] Z. Zhou, F. Liu, Z.S. Zhang, F. Shu, Y. Zheng, L. Fu, L.Y. Li, Human rhomboid family-1 suppresses oxygen-independent degradation of hypoxia-inducible factor-1alpha in breast cancer, Cancer Res 74(10) (2014) 2719-30.
[154] S. Gao, L.-S. Zhang, L. Wang, N.-N. Xiao, H. Long, Y.-L. Yin, Y.-M. Yang, Z. Xi, L.-Y. Li, Z.-S. Zhang, RHBDF1 promotes AP-1-activated endothelial-mesenchymal transition in tumor fibrotic stroma formation, Signal Transduct Target Ther 6(1) (2021) 273-273.
[155] Z. Yan, H. Zou, F. Tian, J.R. Grandis, A.J. Mixson, P.Y. Lu, L.Y. Li, Human rhomboid family-1 gene silencing causes apoptosis or autophagy to epithelial cancer cells and inhibits xenograft tumor growth, Mol Cancer Ther 7(6) (2008) 1355-64.
[156] H. Zou, S.M. Thomas, Z.W. Yan, J.R. Grandis, A. Vogt, L.Y. Li, Human rhomboid family-1 gene RHBDF1 participates in GPCR-mediated transactivation of EGFR growth signals in head and neck squamous cancer cells, FASEB journal : official publication of the Federation of American Societies for Experimental Biology 23(2) (2009) 425-32.
[157] Z. Tang, B. Kang, C. Li, T. Chen, Z. Zhang, GEPIA2: an enhanced web server for large-scale expression profiling and interactive analysis, Nucleic acids research 47(W1) (2019) W556-w560.
[158] K. Krug, E.J. Jaehnig, S. Satpathy, L. Blumenberg, A. Karpova, M. Anurag, G. Miles, P. Mertins, Y. Geffen, L.C. Tang, D.I. Heiman, S. Cao, Y.E. Maruvka, J.T. Lei, C. Huang, R.B. Kothadia, A. Colaprico, C. Birger, J. Wang, Y. Dou, B. Wen, Z. Shi, Y. Liao, M. Wiznerowicz, M.A. Wyczalkowski, X.S. Chen, J.J. Kennedy, A.G. Paulovich, M. Thiagarajan, C.R. Kinsinger, T. Hiltke, E.S. Boja, M. Mesri, A.I. Robles, H. Rodriguez, T.F. Westbrook, L. Ding, G. Getz, K.R. Clauser, D. Fenyö, K.V. Ruggles, B. Zhang, D.R. Mani, S.A. Carr, M.J. Ellis, M.A. Gillette, Proteogenomic Landscape of Breast Cancer Tumorigenesis and Targeted Therapy, Cell 183(5) (2020) 1436-1456.e31.
[159] B. Seashore-Ludlow, M.G. Rees, J.H. Cheah, M. Cokol, E.V. Price, M.E. Coletti, V. Jones, N.E. Bodycombe, C.K. Soule, J. Gould, B. Alexander, A. Li, P. Montgomery, M.J. Wawer, N. Kuru, J.D. Kotz, C.S. Hon, B. Munoz, T. Liefeld, V. Dančík, J.A. Bittker, M. Palmer, J.E. Bradner, A.F. Shamji, P.A. Clemons, S.L. Schreiber, Harnessing Connectivity in a Large-Scale Small-Molecule Sensitivity Dataset, Cancer Discov 5(11) (2015) 1210-23.
[160] A. Basu, N.E. Bodycombe, J.H. Cheah, E.V. Price, K. Liu, G.I. Schaefer, R.Y. Ebright, M.L. Stewart, D. Ito, S. Wang, A.L. Bracha, T. Liefeld, M. Wawer, J.C. Gilbert, A.J. Wilson, N. Stransky, G.V. Kryukov, V. Dancik, J. Barretina, L.A. Garraway, C.S. Hon, B. Munoz, J.A.

Bittker, B.R. Stockwell, D. Khabele, A.M. Stern, P.A. Clemons, A.F. Shamji, S.L. Schreiber, An interactive resource to identify cancer genetic and lineage dependencies targeted by small molecules, Cell 154(5) (2013) 1151-1161.
[161] M.G. Rees, B. Seashore-Ludlow, J.H. Cheah, D.J. Adams, E.V. Price, S. Gill, S. Javaid, M.E. Coletti, V.L. Jones, N.E. Bodycombe, C.K. Soule, B. Alexander, A. Li, P. Montgomery, J.D. Kotz, C.S. Hon, B. Munoz, T. Liefeld, V. Dančík, D.A. Haber, C.B. Clish, J.A. Bittker, M. Palmer, B.K. Wagner, P.A. Clemons, A.F. Shamji, S.L. Schreiber, Correlating chemical sensitivity and basal gene expression reveals mechanism of action, Nat Chem Biol 12(2) (2016) 109-16.
[162] Z. Wan, R. Sun, Y.-W. Liu, S. Li, J. Sun, J. Li, J. Zhu, P. Moharil, B. Zhang, P. Ren, G. Ren, M. Zhang, X. Ma, S. Dai, D. Yang, B. Lu, S. Li, Targeting metabotropic glutamate receptor 4 for cancer immunotherapy, Science Advances 7(50) eabj4226.
[163] A. Subramanian, P. Tamayo, V.K. Mootha, S. Mukherjee, B.L. Ebert, M.A. Gillette, A. Paulovich, S.L. Pomeroy, T.R. Golub, E.S. Lander, J.P. Mesirov, Gene set enrichment analysis: A knowledge-based approach for interpreting genome-wide expression profiles, Proceedings of the National Academy of Sciences 102(43) (2005) 15545-15550.
[164] N.E. Sanjana, O. Shalem, F. Zhang, Improved vectors and genome-wide libraries for CRISPR screening, Nat Methods 11(8) (2014) 783-784.
[165] Z. Wang, B. Yang, M. Zhang, W. Guo, Z. Wu, Y. Wang, L. Jia, S. Li, W. Xie, D. Yang, lncRNA Epigenetic Landscape Analysis Identifies EPIC1 as an Oncogenic lncRNA that Interacts with MYC and Promotes Cell-Cycle Progression in Cancer, Cancer Cell 33(4) (2018) 706-720.e9.
[166] P.Y. Ho, Z. Duan, N. Batra, J.L. Jilek, M.J. Tu, J.X. Qiu, Z. Hu, T. Wun, P.N. Lara, R.W. DeVere White, H.W. Chen, A.M. Yu, Bioengineered Noncoding RNAs Selectively Change Cellular miRNome Profiles for Cancer Therapy, J Pharmacol Exp Ther 365(3) (2018) 494-506.
[167] P.C. Li, M.J. Tu, P.Y. Ho, N. Batra, M.M.L. Tran, J.X. Qiu, T. Wun, P.N. Lara, X. Hu, A.X. Yu, A.M. Yu, In vivo fermentation production of humanized noncoding RNAs carrying payload miRNAs for targeted anticancer therapy, Theranostics 11(10) (2021) 4858-4871.
[168] S. Ning, C. Liu, W. Lou, J.C. Yang, A.P. Lombard, L.S. D'Abronzo, N. Batra, A.M. Yu, A.R. Leslie, M. Sharifi, C.P. Evans, A.C. Gao, Bioengineered BERA-Wnt5a siRNA Targeting Wnt5a/FZD2 Signaling Suppresses Advanced Prostate Cancer Tumor Growth and Enhances Enzalutamide Treatment, Mol Cancer Ther 21(10) (2022) 1594-1607.
[169] W.P. Wang, P.Y. Ho, Q.X. Chen, B. Addepalli, P.A. Limbach, M.M. Li, W.J. Wu, J.L. Jilek, J.X. Qiu, H.J. Zhang, T. Li, T. Wun, R.D. White, K.S. Lam, A.M. Yu, Bioengineering Novel Chimeric microRNA-34a for Prodrug Cancer Therapy: High-Yield Expression and Purification, and Structural and Functional Characterization, J Pharmacol Exp Ther 354(2) (2015) 131-41.
[170] P.R. Christensen, A.M. Scheuermann, K.E. Loeffler, B.A. Helms, Closed-loop recycling of plastics enabled by dynamic covalent diketoenamine bonds, Nature Chemistry 11(5) (2019) 442-448.
[171] W.F. Tivol, A. Briegel, G.J. Jensen, An improved cryogen for plunge freezing, Microsc Microanal 14(5) (2008) 375-9.
[172] N. Yongvongsoontorn, J.E. Chung, S.J. Gao, K.H. Bae, A. Yamashita, M.-H. Tan, J.Y. Ying, M. Kurisawa, Carrier-Enhanced Anticancer Efficacy of Sunitinib-Loaded Green Tea-Based Micellar Nanocomplex beyond Tumor-Targeted Delivery, ACS Nano 13(7) (2019) 7591-7602.
[173] J. Xu, J. Sun, P. Wang, X. Ma, S. Li, Pendant HDAC inhibitor SAHA derivatised polymer as a novel prodrug micellar carrier for anticancer drugs, Journal of drug targeting 26(5-6) (2018) 448-457.
[174] A.B. Inc., IC50 Calculator, 2023. https://www.aatbio.com/tools/ic50-calculator.

[175] A. Ianevski, A.K. Giri, T. Aittokallio, SynergyFinder 3.0: an interactive analysis and consensus interpretation of multi-drug synergies across multiple samples, Nucleic acids research 50(W1) (2022) W739-W743.
[176] M.F. Kramer, Stem-loop RT-qPCR for miRNAs, Current protocols in molecular biology Chapter 15 (2011) Unit 15.10.
[177] T. Jaki, M.J. Wolfsegger, Estimation of pharmacokinetic parameters with the R package PK, Pharmaceutical Statistics 10(3) (2011) 284-288.
[178] Q. Xu, C. Chen, B. Liu, Y. Lin, P. Zheng, D. Zhou, Y. Xie, Y. Lin, C. Guo, J. Liu, L. Li, Association of iRhom1 and iRhom2 expression with prognosis in patients with cervical cancer and possible signaling pathways, Oncol Rep 43(1) (2020) 41-54.
[179] F. Bruzzese, M. Rocco, S. Castelli, E. Di Gennaro, A. Desideri, A. Budillon, Synergistic antitumor effect between vorinostat and topotecan in small cell lung cancer cells is mediated by generation of reactive oxygen species and DNA damage-induced apoptosis, Molecular Cancer Therapeutics 8(11) (2009) 3075-3087.
[180] S. Kudaravalli, P. den Hollander, S.A. Mani, Role of p38 MAP kinase in cancer stem cells and metastasis, Oncogene 41(23) (2022) 3177-3185.
[181] A. Igea, A.R. Nebreda, The Stress Kinase p38α as a Target for Cancer Therapy, Cancer Research 75(19) (2015) 3997-4002.
[182] E.L. Huttlin, L. Ting, R.J. Bruckner, F. Gebreab, M.P. Gygi, J. Szpyt, S. Tam, G. Zarraga, G. Colby, K. Baltier, R. Dong, V. Guarani, L.P. Vaites, A. Ordureau, R. Rad, B.K. Erickson, M. Wühr, J. Chick, B. Zhai, D. Kolippakkam, J. Mintseris, R.A. Obar, T. Harris, S. Artavanis-Tsakonas, M.E. Sowa, P. De Camilli, J.A. Paulo, J.W. Harper, S.P. Gygi, The BioPlex Network: A Systematic Exploration of the Human Interactome, Cell 162(2) (2015) 425-440.
[183] E.L. Huttlin, R.J. Bruckner, J.A. Paulo, J.R. Cannon, L. Ting, K. Baltier, G. Colby, F. Gebreab, M.P. Gygi, H. Parzen, J. Szpyt, S. Tam, G. Zarraga, L. Pontano-Vaites, S. Swarup, A.E. White, D.K. Schweppe, R. Rad, B.K. Erickson, R.A. Obar, K.G. Guruharsha, K. Li, S. Artavanis-Tsakonas, S.P. Gygi, J.W. Harper, Architecture of the human interactome defines protein communities and disease networks, Nature 545(7655) (2017) 505-509.
[184] L. Nappi, A.H. Aguda, N.A. Nakouzi, B. Lelj-Garolla, E. Beraldi, N. Lallous, M. Thi, S. Moore, L. Fazli, D. Battsogt, S. Stief, F. Ban, N.T. Nguyen, N. Saxena, E. Dueva, F. Zhang, T. Yamazaki, A. Zoubeidi, A. Cherkasov, G.D. Brayer, M. Gleave, Ivermectin inhibits HSP27 and potentiates efficacy of oncogene targeting in tumor models, The Journal of Clinical Investigation 130(2) (2020) 699-714.
[185] M. Shiota, J.L. Bishop, K.M. Nip, A. Zardan, A. Takeuchi, T. Cordonnier, E. Beraldi, J. Bazov, L. Fazli, K. Chi, M. Gleave, A. Zoubeidi, Hsp27 Regulates Epithelial Mesenchymal Transition, Metastasis, and Circulating Tumor Cells in Prostate Cancer, Cancer Research 73(10) (2013) 3109-3119.
[186] J.M. Crudele, J.S. Chamberlain, Cas9 immunity creates challenges for CRISPR gene editing therapies, Nature Communications 9(1) (2018) 3497.
[187] C.T. Charlesworth, P.S. Deshpande, D.P. Dever, J. Camarena, V.T. Lemgart, M.K. Cromer, C.A. Vakulskas, M.A. Collingwood, L. Zhang, N.M. Bode, M.A. Behlke, B. Dejene, B. Cieniewicz, R. Romano, B.J. Lesch, N. Gomez-Ospina, S. Mantri, M. Pavel-Dinu, K.I. Weinberg, M.H. Porteus, Identification of preexisting adaptive immunity to Cas9 proteins in humans, Nature Medicine 25(2) (2019) 249-254.
[188] A. Bhuniya, D. Pattarayan, D. Yang, Lentiviral vector transduction provides nonspecific immunogenicity for syngeneic tumor models, Mol Carcinog 61(12) (2022) 1073-1081.

[189] L.D. Falo, M. Kovacsovics-Bankowski, K. Thompson, K.L. Rock, Targeting antigen into the phagocytic pathway in vivo induces protective tumour immunity, Nature Medicine 1(7) (1995) 649-653.
[190] I.A. York, M.A. Brehm, S. Zendzian, C.F. Towne, K.L. Rock, Endoplasmic reticulum aminopeptidase 1 (ERAP1) trims MHC class I-presented peptides in vivo and plays an important role in immunodominance, Proceedings of the National Academy of Sciences 103(24) (2006) 9202-9207.
[191] A. Komlosh, F. Momburg, T. Weinschenk, N. Emmerich, H. Schild, E. Nadav, I. Shaked, Y. Reiss, A Role for a Novel Luminal Endoplasmic Reticulum Aminopeptidase in Final Trimming of 26 S Proteasome-generated Major Histocompatability Complex Class I Antigenic Peptides*, Journal of Biological Chemistry 276(32) (2001) 30050-30056.
[192] X. Cui, F. Hawari, S. Alsaaty, M. Lawrence, C.A. Combs, W. Geng, F.N. Rouhani, D. Miskinis, S.J. Levine, Identification of ARTS-1 as a novel TNFR1-binding protein that promotes TNFR1 ectodomain shedding, The Journal of Clinical Investigation 110(4) (2002) 515-526.
[193] X. Cui, F.N. Rouhani, F. Hawari, S.J. Levine, An Aminopeptidase, ARTS-1, Is Required for Interleukin-6 Receptor Shedding*, Journal of Biological Chemistry 278(31) (2003) 28677-28685.
[194] S.S. Cao, R.J. Kaufman, iRhoms: ERADicating the messenger in growth control signaling, Developmental cell 20(4) (2011) 414-6.
[195] I. Dulloo, S. Muliyil, M. Freeman, The molecular, cellular and pathophysiological roles of iRhom pseudoproteases, Open Biology 9(3) 190003.
[196] Z. Duan, A.-M. Yu, Bioengineered non-coding RNA agent (BERA) in action, Bioengineered 7(6) (2016) 411-417.
[197] P.Y. Ho, A.M. Yu, Bioengineering of noncoding RNAs for research agents and therapeutics, Wiley interdisciplinary reviews. RNA 7(2) (2016) 186-97.
[198] M. Li, S. Schlesiger, S.K. Knauer, C. Schmuck, A tailor-made specific anion-binding motif in the side chain transforms a tetrapeptide into an efficient vector for gene delivery, Angewandte Chemie 127(10) (2015) 2984-2987.
[199] W.M. Argüelles-Monal, J. Lizardi-Mendoza, D. Fernández-Quiroz, M.T. Recillas-Mota, M. Montiel-Herrera, Chitosan Derivatives: Introducing New Functionalities with a Controlled Molecular Architecture for Innovative Materials, Polymers, 2018.
[200] P. Kesharwani, R. Chadar, A. Sheikh, W.Y. Rizg, A.Y. Safhi, CD44-Targeted Nanocarrier for Cancer Therapy, Frontiers in Pharmacology 12 (2022).
[201] I. Okamoto, H. Tsuiki, L.C. Kenyon, A.K. Godwin, D.R. Emlet, M. Holgado-Madruga, I.S. Lanham, C.J. Joynes, K.T. Vo, A. Guha, M. Matsumoto, Y. Ushio, H. Saya, A.J. Wong, Proteolytic Cleavage of the CD44 Adhesion Molecule in Multiple Human Tumors, The American Journal of Pathology 160(2) (2002) 441-447.
[202] P. Kamarajan, J.M. Shin, X. Qian, B. Matte, J.Y. Zhu, Y.L. Kapila, ADAM17-mediated CD44 cleavage promotes orasphere formation or stemness and tumorigenesis in HNSCC, Cancer Med 2(6) (2013) 793-802.
[203] E. Johansson, E.S. Grassi, V. Pantazopoulou, B. Tong, D. Lindgren, T.J. Berg, E.J. Pietras, H. Axelson, A. Pietras, CD44 Interacts with HIF-2α to Modulate the Hypoxic Phenotype of Perinecrotic and Perivascular Glioma Cells, Cell Rep 20(7) (2017) 1641-1653.
[204] H. Yoo, S.K. Choi, J. Lee, S.H. Park, Y.N. Park, S.Y. Hwang, J.H. Shin, Y. Na, Y. Kwon, H.J. Lee, Y.S. Lee, Drug-Like Small Molecule HSP27 Functional Inhibitor Sensitizes Lung Cancer Cells to Gefitinib or Cisplatin by Inducing Altered Cross-Linked Hsp27 Dimers, Pharmaceutics 13(5) (2021).

[205] Z. Liu, Y. Liu, Y. Long, B. Liu, X. Wang, Role of HSP27 in the multidrug sensitivity and resistance of colon cancer cells, Oncology letters 19(3) (2020) 2021-2027.
[206] R.K. Hansen, I. Parra, P. Lemieux, S. Oesterreich, S.G. Hilsenbeck, S.A. Fuqua, Hsp27 overexpression inhibits doxorubicin-induced apoptosis in human breast cancer cells, Breast cancer research and treatment 56(2) (1999) 187-96.
[207] S.F. Chen, S. Nieh, S.W. Jao, C.L. Liu, C.H. Wu, Y.C. Chang, C.Y. Yang, Y.S. Lin, Quercetin suppresses drug-resistant spheres via the p38 MAPK-Hsp27 apoptotic pathway in oral cancer cells, PLoS One 7(11) (2012) e49275.
[208] M. Lampros, N. Vlachos, S. Voulgaris, G.A. Alexiou, The Role of Hsp27 in Chemotherapy Resistance, Biomedicines 10(4) (2022).
[209] R. Liu, Y. Chen, G. Liu, C. Li, Y. Song, Z. Cao, W. Li, J. Hu, C. Lu, Y. Liu, PI3K/AKT pathway as a key link modulates the multidrug resistance of cancers, Cell Death & Disease 11(9) (2020) 797.
[210] M. Malhotra, C. Tomaro-Duchesneau, S. Prakash, Synthesis of TAT peptide-tagged PEGylated chitosan nanoparticles for siRNA delivery targeting neurodegenerative diseases, Biomaterials 34(4) (2013) 1270-1280.
[211] D. Gurusamy, K. Mogilicherla, S.R. Palli, Chitosan nanoparticles help double-stranded RNA escape from endosomes and improve RNA interference in the fall armyworm, Spodoptera frugiperda, Arch Insect Biochem Physiol 104(4) (2020) e21677.
[212] M. Köping-Höggård, K.M. Vårum, M. Issa, S. Danielsen, B.E. Christensen, B.T. Stokke, P. Artursson, Improved chitosan-mediated gene delivery based on easily dissociated chitosan polyplexes of highly defined chitosan oligomers, Gene Ther 11(19) (2004) 1441-52.
[213] O. Nagano, H. Saya, Mechanism and biological significance of CD44 cleavage, Cancer Science 95(12) (2004) 930-935.
[214] E. Johansson, E.S. Grassi, V. Pantazopoulou, B. Tong, D. Lindgren, T.J. Berg, E.J. Pietras, H. Axelson, A. Pietras, CD44 Interacts with HIF-2α to Modulate the Hypoxic Phenotype of Perinecrotic and Perivascular Glioma Cells, Cell Reports 20(7) (2017) 1641-1653.
[215] N. Saha, K. Xu, Z. Zhu, D. Robev, T. Kalidindi, Y. Xu, J. Himanen, E. de Stanchina, N.V.K. Pillarsetty, D.S. Dimitrov, D.B. Nikolov, Inhibitory monoclonal antibody targeting ADAM17 expressed on cancer cells, Translational Oncology 15(1) (2022) 101265.
[216] F. Tschanz, S. Bender, I. Telarovic, V. Waller, R.F. Speck, M. Pruschy, The ADAM17-directed Inhibitory Antibody MEDI3622 Antagonizes Radiotherapy-induced VEGF Release and Sensitizes Non–Small Cell Lung Cancer for Radiotherapy, Cancer Research Communications 1(3) (2021) 164-177.
[217] F. Caiazza, P.M. McGowan, M. Mullooly, A. Murray, N. Synnott, N. O'Donovan, L. Flanagan, C.J. Tape, G. Murphy, J. Crown, M.J. Duffy, Targeting ADAM-17 with an inhibitory monoclonal antibody has antitumour effects in triple-negative breast cancer cells, British Journal of Cancer 112(12) (2015) 1895-1903.
[218] H. Tang, Y. Zhang, T. Yang, C. Wang, Y. Zhu, L. Qiu, J. Liu, Y. Song, L. Zhou, J. Zhang, Y.K. Wong, Y. Liu, C. Xu, H. Wang, J. Wang, Cholesterol modulates the physiological response to nanoparticles by changing the composition of protein corona, Nat Nanotechnol 18(9) (2023) 1067-1077.